JETP Letters, Vol. 76, No. 11, 2002, pp. 647–650. From Pis'ma v Zhurnal Éksperimental'noĭ i Teoreticheskoĭ Fiziki, Vol. 76, No. 11, 2002, pp. 771–773.

Confining String Formed by *P* Vortices in the Indirect *Z*(2) Projection of *SU*(2) Lattice Gauge Theory¶

V. G. Bornyakov[1, 2, 3]*, A. V. Kovalenko[2]*, M. I. Polikarpov[2]*, and D. A. Sigaev[2]*

[1] *Institute for Theoretical Physics, Kanazawa University, 920-1192 Kanazawa, Japan*

[2] *Institute for Theoretical and Experimental Physics, Moscow, 117259 Russia*

[3] *Institute for High Energy Physics, Russian Academy of Sciences, Protvino, 142280 Russia*

**e-mail: vborn@itep.ru; kovalenko@itep.ru; polykarp@itep.ru; sigaev@itep.ru*

Received October 24, 2002

We study the distribution of *P* vortices near the confining string in the indirect *Z*(2) projection of *SU*(2) lattice gauge theory. We find that the density of vortices approaches the vacuum value at large distances and is strongly suppressed near the line connecting the test quark–antiquark pair. This implies that the condensate of *P* vortices is broken inside the confining string. The width of the *P*-vortex density distribution increases with increasing distance between the quark and antiquark. Our best fit indicates the logarithmic dependence of this width on $q\bar{q}$ separation. © *2002 MAIK "Nauka/Interperiodica"*.

PACS numbers: 11.15.Ha; 12.38.Aw

1. INTRODUCTION

It was suggested by 't Hooft and Mandelstam that the string formation between the massive quark and antiquark was an analogue of the dual Meissner effect in a superconducting vacuum [1], and the most popular theory of quark confinement was based on the abelian projection [2].

There are also alternative theories of quark confinement. It was found recently that one of them, the magnetic vortex theory [3], did not have some drawbacks of the abelian projected theory. The most remarkable success of the magnetic vortex theory is the explanation of the existence of the linear potential between higher representation quarks in the Casimir scaling regime [4].

While in the abelian projected theory a part of the *SU*(*N*) symmetry is broken, leaving $U(1)^{N-1}$ gauge symmetry, in the magnetic vortex theory, the Z_N center plays a special role. Thus, further gauge fixing, which leaves a remnant *Z*(*N*) symmetry, is to be performed.

This can be achieved in several ways. First, we can directly fix the gauge in *SU*(*N*) theory leaving *Z*(*N*) gauge symmetry [4]. We can also use the indirect *Z*(2) projection [4]. It is defined in terms of abelian variables; i.e., we have to perform the abelian projection first. After fixing the maximal abelian gauge [5] and projecting *SU*(2) link variables $U_{x\mu}$ onto abelian link variables $u_{x\mu}$, we maximize the functional *R* and define the link variables $Z_{x\mu}$:

$$R = \sum_{x,\mu} \cos^2\theta_{x\mu},$$

$$Z_{x\mu} = \mathrm{sgn}(\cos\theta_{x\mu}),$$

where $\cos\theta_{x\mu} = \frac{1}{2}\mathrm{Tr}\,u_{x\mu}$.

A plaquette is pierced by a *P* vortex lying on the dual lattice if *Z*(2) plaquette $P_{x,\mu\nu} \equiv Z_{x\mu}Z_{x+\mu,\nu}Z^{\dagger}_{x+\nu,\mu}Z^{\dagger}_{x\nu} = -1$.

Below we present the results of studying a confining string in terms of *P* vortices. Applying the indirect *Z*(2) projection to the original *SU*(2) configurations for various lattice sizes and couplings β, we obtain reliable results for the form of *Z*(2) confining string and the dependence of its radius on the distance between the test quark and antiquark.

2. VORTICES NEAR THE CONFINING STRING

We consider the quantity that measures the dependence of the vortex density on the distances $r_\perp$ from the $q\bar{q}$ axis and $r_\parallel$ along this axis

$$Q(r_\perp, r_\parallel) = \frac{\langle WV(r_\perp, r_\parallel)\rangle}{\langle W\rangle}, \quad (1)$$

¶This article was submitted by the authors in English.

Simulation details

β	Lattice size	Number of configurations
2.40	24^4	20
2.50	24^4	50
2.55	28^4	50
2.60	28^4	25

where W is a $Z(2)$ Wilson loop and vortex detector $V(r_\perp, r_\parallel) = (1 - P_{x,\mu\nu})/2$. A similar quantity was investigated for the distribution of monopole currents near the confining string [6]. Our calculations were performed on $Z(2)$ vacuum configurations obtained via the indirect $Z(2)$ projection, the intermediate gauge fixing being performed by the simulated annealing algorithm [7]. The table summarizes the information about the configurations used.

Since a P vortex is a 2-dimensional surface in 4-dimensional space, the P-vortex density is defined on the plaquettes and has 6 independent components for each site. Thus, the complete measurement of the P-vortex density involves measurements of 6 quantities per site, or one quantity per plaquette. We use the notation "01," "02," etc., to denote the orientation of the vortex detector $V(r_\perp, r_\parallel)$, where "0" denotes the temporal direction of the $Z(2)$ Wilson loop, "1" denotes the spatial direction of the $Z(2)$ Wilson loop, and "2" is the direction in which $r_\perp$ is counted, so that the densities for planes "μ 2" and "μ 3" may differ (and actually do so).

Obviously, there is no correlation between W and $V(r_\perp, r_\parallel)$ at large distances $r_\perp$, $Q(\infty, r_\parallel) = \langle V \rangle$, which is the value of the vacuum vortex density [8]. However, the vortex density decreases near the confining string. This effect is illustrated in Fig. 1. The minima in Fig. 1 correspond to the positions of the test quark and antiquark. This figure actually represents only one of the six components of vortex density, "01," but the others look rather similar.

In Fig. 2, we show the dependence of all six components of the vortex density $Q(r_\perp, r_\parallel)/a^2$ on the distance $r_\perp$ for $r_\parallel$ fixed at the middle of the $q\bar{q}$ axis and the vortex detector V lying in various planes. We see stronger suppression of Q for the plane "01," which is parallel to the Wilson loop. The normalization $1/a^2$ is due to dimensional considerations [4]; the density of P vortices, which are 2-dimensional surfaces, should scale as a^2, a being the lattice spacing.

3. THE RADIUS OF THE CONFINING STRING

We employ $Q(r_\perp, r_\parallel)$ to evaluate the radius of the confining string in terms of P vortices.

The Gaussian form of the fitting function is used to fit our data:

$$Q(r_\perp) = A\exp\left[-\left(\frac{r_\perp}{r_0}\right)^2\right] + Q(\infty), \qquad (2)$$

A and r_0 being the fitting parameters. It is reasonable to treat r_0 as the radius of the confining string. Function (2) was used in studies of the nonabelian [9] and abelian [10] flux-tube action densities and was predicted theoretically in [11]. We obtained fits with reasonable χ^2 (Fig. 3).

To determine the dependence of the radius r_0 on the distance R between the quark and antiquark, we involve the data for four different β and various sizes of Wilson loops. Different β yield results that are in good agree-

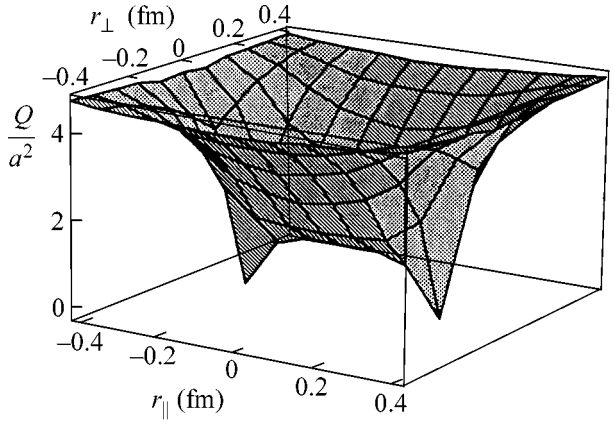

Fig. 1. The dependence of Q/a^2 on $r_\perp$ and $r_\parallel$, β = 2.5.

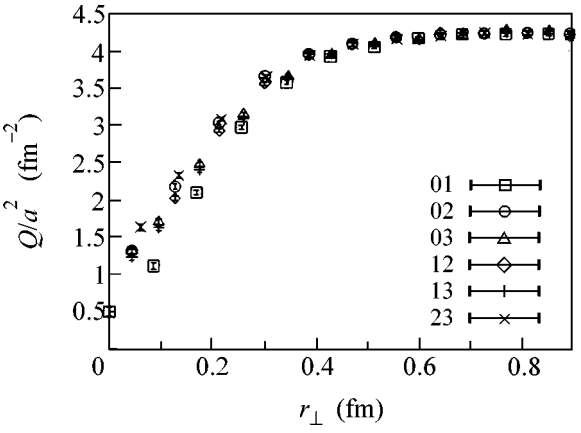

Fig. 2. Q/a^2 as a function of $r_\perp$ for the Wilson loop 11×5, β = 2.5. Notation "01" means that the detecting plaquette lies in the plane "01."

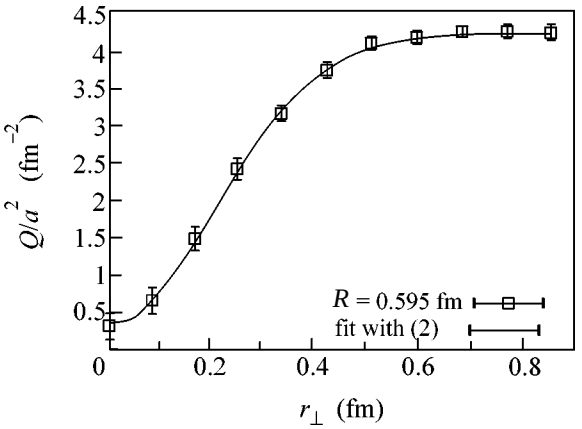

Fig. 3. The fit of the confining string profile by expression (2) for the Wilson loop 11 × 9, β = 2.5. The data are for plaquettes "01."

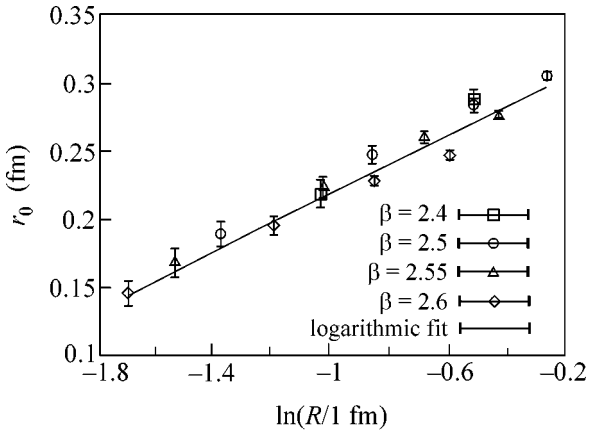

Fig. 4. The confining string radius as a function of ln *R*.

ment (Fig. 4), confirming that our results correspond to the continuum limit.

We used several fitting functions to describe the dependence of r_0 on R; the best χ^2 was obtained for

$$r_0(R) = a\ln(R/1\text{ fm}) + b, \quad (3)$$

which is shown in Fig. 4 by the solid line; $\chi^2/n_{\text{free}} = 4.43$, $a = 0.107(8)$ fm, $b = 0.326(6)$ fm. A slightly worse fit ($\chi^2/n_{\text{free}} = 4.47$) was obtained for the fitting function $r_0(R) = (aR + b)^\alpha$ with one extra free parameter α. The fit using the dependence $r_0(R) = (a\ln(R/1\text{ fm}) + b)^{1/2}$, which is predicted by the simple string model [11], gives a worse $\chi^2/n_{\text{free}} = 5.89$.

It is worth mentioning that the logarithmic dependence of r_0^2 was found in the studies of the nonabelian flux tube [9], while for the abelian flux tube the width was found to be independent of R [10]. On the other hand, accurate recent studies have shown the dependence of the width of the abelian flux tube on the distance between the test quark–antiquark pair (Y. Koma, private communication).

Note that in Fig. 4 even data for very small $R \approx 0.2$ fm seem to lie on the same curve as data for larger R (till $R \approx 0.8$ fm). This means that the confining string is already formed at very small distances. This fact is in agreement with the results of [4], where the correct value of the string tension was obtained from small $Z(2)$ Wilson loops.

4. DISCUSSION

For the monopole-confinement mechanism, there exists the effective classical model, which is the dual abelian Higgs model. The classical equations of motion for this model describe the profile of the confining string in the maximal abelian projection unexpectedly well [6]. For *P* vortices, we have no classical effective model, and our fitting function (2) has a phenomenological origin. On the other hand, the qualitative similarity of the dependence of $Q(r_\perp, r_\parallel)$ on $r_\perp$ to the dependence of the action density of the nonabelian or abelian flux tube is not accidental. $Q(r_\perp, r_\parallel)$ can be interpreted as the $Z(2)$ projection of the nonabelian magnetic/electric energy density. This aspect will be discussed elsewhere.

We can also explain the flux-tube profile shown in Fig. 1 from a different point of view. It is well known that monopoles correlate with *P* vortices [4]. On the other hand, it is also known that the condensate of monopoles is broken inside the confining string. Thus, one can expect that the condensate of *P* vortices should also be broken or, at least, substantially reduced inside the confining string. We actually see this effect in Figs. 1–3.

We are grateful to M.N. Chernodub, F.V. Gubarev, and V.I. Zakharov for useful discussions. M.I.P. was supported in part by the Russian Foundation for Basic Research (project nos. 02-02-17308, 01-02-117456, 00-15-96-786), by INTAS-00-00111, and by the CRDF award RPI-2364-MO-02. A.V.K. was supported in part by the Russian Foundation for Basic Research (project no. 02-02-17308) and CRDF MO-011-0. B.V.G. acknowledges the support of a JSPS Fellowship grant.

REFERENCES

1. G. 't Hooft, *High Energy Physics*, Ed. by A. Zichichi (Editrice Compositori, Bolognia, 1976); S. Mandelstam, Phys. Rep. **23**, 245 (1976).
2. G. 't Hooft, Nucl. Phys. B **190**, 455 (1981).
3. G. 't Hooft, Nucl. Phys. B **138**, 1 (1978); J. M. Cornwall, Nucl. Phys. B **157**, 392 (1979).

4. L. Del Debbio, M. Faber, J. Greensite, and S. Olejnik, Phys. Rev. D **55**, 2298 (1997); hep-lat/9610005; M. Faber, J. Greensite, and S. Olejnik, Phys. Rev. D **57**, 2603 (1998); hep-lat/9710039.

5. A. S. Kronfeld, G. Schierholz, and U. J. Wiese, Nucl. Phys. B **293**, 461 (1987).

6. V. Singh, D. A. Browne, and R. W. Haymaker, Phys. Lett. B **306**, 115 (1993); hep-lat/9301004; C. Schlichter, G. S. Bali, and K. Schilling, Nucl. Phys. Proc. Suppl. **63**, 519 (1998); hep-lat/9709114; F. V. Gubarev, E. M. Ilgenfritz, M. I. Polikarpov, and T. Suzuki, Phys. Lett. B **468**, 134 (1999); hep-lat/9909099.

7. V. G. Bornyakov, D. A. Komarov, and M. I. Polikarpov, Phys. Lett. B **497**, 151 (2001); hep-lat/0009035.

8. M. N. Chernodub, M. I. Polikarpov, A. I. Veselov, and M. A. Zubkov, Nucl. Phys. Proc. Suppl. **73**, 575 (1999); hep-lat/9809158.

9. G. S. Bali, K. Schilling, and C. Schlichter, Phys. Rev. D **51**, 5165 (1995); hep-lat/9409005.

10. G. S. Bali, hep-ph/9809351; V. Bornyakov, H. Ichie, S. Kitahara, *et al.*, Nucl. Phys. Proc. Suppl. **106**, 634 (2002); hep-lat/0111042.

11. M. Luscher, G. Munster, and P. Weisz, Nucl. Phys. B **180**, 1 (1981).

JETP Letters, Vol. 76, No. 11, 2002, pp. 651–655. From Pis'ma v Zhurnal Éksperimental'noĭ i Teoreticheskoĭ Fiziki, Vol. 76, No. 11, 2002, pp. 774–778.

Possible Universal Cause of High-T_c Superconductivity in Different Metals¶

M. Ya. Amusia[1, 2] and V. R. Shaginyan[3, *]

[1] *The Racah Institute of Physics, the Hebrew University, 91904 Jerusalem, Israel*
[2] *Ioffe Physicotechnical Institute, Russian Academy of Sciences, St. Petersburg, 194021 Russia*
[3] *St. Petersburg Nuclear Physics Institute, Russian Academy of Sciences, Gatchina, 188300 Russia*
**e-mail: vrshag@thd.pnpi.spb.ru*

Received June 17, 2002; in final form, October 31, 2002

Using the theory of high-temperature superconductivity based on the idea of the fermion-condensation quantum phase transition (FCQPT), we show that neither the *d*-wave pairing symmetry, the pseudogap phenomenon, nor the presence of the $Cu–O_2$ planes is of decisive importance for the existence of high-T_c superconductivity. We analyze recent experimental data on this type of superconductivity in different materials and show that these facts can be understood within the theory of superconductivity based on the FCQPT. The latter can be considered as a universal cause of high-T_c superconductivity. The main features of a room-temperature superconductor are discussed. © *2002 MAIK "Nauka/Interperiodica".*

PACS numbers: 74.20.Fg; 71.27.+a; 74.72.-h

It has been a long-standing problem to develop a theory describing high-temperature superconductivity (HTS) observed in copper oxide based compounds. These compounds are extremely complex materials having a great number of competing degrees of freedom, which produce a great variety of physical properties. In turn, these properties can compete and coexist with superconductivity, hiding the understanding of the universal cause of superconductivity. As a result, it was suggested that the unique superconducting properties in these compounds are determined by the presence of the $Cu–O_2$ planes, by the *d*-wave pairing symmetry, and by the existence of the pseudogap phenomena in optimally doped and underdoped cuprates (see, e.g., [1–3]).

However, recent studies of quasiparticle tunneling spectra of cuprates have revealed that the pairing symmetry may change from *d*- to *s*-wave symmetry, depending on the hole- or electron-doping level [4]. Then, high-temperature *s*-wave superconductivity was observed in electron-doped infinite layer cuprates with a sharp transition at $T = 43$ K, without a pseudogap [5]. Therefore, we can conclude that the *d*-wave symmetry of pairs and the pseudogap phenomena are not necessary parts of HTS. Recent studies of HTS in chemically doped A_3C_{60} [6] have shown that the presence of the $Cu–O_2$ planes is also not a necessary condition for the existence of HTS. Moreover, it has recently been demonstrated that strongly overdoped cuprates Tl-2201 obey the Wiedemann–Pranz law perfectly [7]. This fact, attesting that excitations, which carry heat, also carry charge *e*, shows that these quasiparticles have the same properties as Landau quasiparticles. This imposes serious constraints upon the possible theories of HTS. For instance, this fact demonstrates that there is no spin–charge separation [7], as was suggested in one group of proposals [8, 9]. On the other hand, it is well known that the superconducting transition temperature $T_c^{\alpha\gamma}(x)$ of the oxides appears to pass through a bell-shaped curve as a function of the hole (or electron) mobile charge-carrier density x (see, e.g., [3]). Here, α denotes the material, say C_{60} or Tl-2201, etc., and γ denotes hole or electron doping. It is essential to note that the shape of the functions $T_c^{\alpha\gamma}(x)$ is similar in different samples, so that there exist empirical formulas that relate the transition temperature $T_c^{\alpha\gamma}(x)$ to the carrier concentration x. For example, in case of Tl-2201 (see, e.g., [7]), $T_c(x) = T_c^M(1 - 82.6(p - 0.16)^2)$. Here, T_c^M is the maximum value of the transition temperature. Thus, we can use the simple approximation

$$T_c^{\alpha\gamma}(x) = T_1^{\alpha}T_2^{\gamma}(x_1 - x)x, \qquad (1)$$

where the coefficients T_1^{α} and T_2^{γ} define the transition temperature T_c for a given hole (or electron) metal, with x obviously going continuously to zero at the insulator–metal transition. It directly follows from Eq. (1) that the transition temperature reaches its maximum value T_c^M at the optimal doping level $x_{\rm opt}$

$$T_c^M = T_c^{\alpha\gamma}(x_{\rm opt}) = T_1^{\alpha}T_2^{\gamma}\left(\frac{x_1}{2}\right)^2. \qquad (2)$$

¶This article was submitted by the authors in English.

The general shape of the function $T_c(x)$ points to the fact that the generic properties of HTS are defined by a 2D charge (electron or hole) in a strongly correlated liquid rather then by the solids that hold this liquid. As to the solids, they arrange the presence of the pseudogap phenomena, *s*- or *d*-wave pairing symmetry, the electron–phonon coupling constant defining T_c, the variation region of x, and so on.

It is well known that consideration of strongly correlated liquids is close to the problem of systems with a large coupling constant, which is the most important in many-body physics. One solution of this problem has been offered by Landau theory of normal Fermi liquids, which introduces the notion of quasiparticles and parameters characterizing the effective interaction between them [10]. As a result, the Landau theory removed high-energy degrees of freedom and kept a sufficiently large number of relevant low-energy degrees of freedom to treat the liquid's low-energy properties. Usually, it is assumed that the breakdown of Landau theory is defined by Pomeranchuk's stability conditions and occurs when the Landau amplitudes, being negative, reach critical value. The new phase, in which the stability conditions are restored, can in principle be again described in the framework of the theory. However, it has recently been demonstrated [11] that the Pomeranchuk conditions do not cover all possible limitations: the overlooked one is related to the situation where, at temperature $T = 0$, the effective mass can become infinitely large. It was demonstrated that such a situation, leading to profound consequences, can take place when the corresponding amplitude, being positive, reaches a critical value, producing a completely new class of strongly correlated Fermi liquids with the fermion condensate (FC) [11, 12]. This liquid is separated from a normal Fermi liquid by the fermion-condensation quantum phase transition (FCQPT) [13]. In such a case, we are dealing with the strong-coupling limit, where an absolutely reliable answer based on purely theoretical first-principle grounds cannot be given. Therefore, the only way to verify whether the FC occurs is to consider the experimental facts that can signal the existence of such a state. It seems to us that there are strong indications of the existence of FC in high-T_c superconductors.

In this letter, we show that the new experimental facts mentioned above are the desirable evidence and that they can be explained within the theory of HTS based on the FCQPT [14]. We also describe the main features of corresponding room-temperature superconductors.

Let us start with a brief consideration of the general properties of a two-dimensional electron liquid in the superconducting state, when the system underwent FCQPT [13, 14]. At $T = 0$, the ground-state energy $E_{gs}[\kappa(\mathbf{p}), n(\mathbf{p})]$ is a functional of the order parameter, of the superconducting state $\kappa(\mathbf{p})$, and of the quasiparticle occupation numbers $n(\mathbf{p})$ and is determined by the well-known equation of the weak-coupling theory of superconductivity (see, e.g., [15])

$$E_{gs} = E[n(\mathbf{p})] + \int \lambda_0 V(\mathbf{p}_1, \mathbf{p}_2)\kappa(\mathbf{p}_1)\kappa^*(\mathbf{p}_2)\frac{d\mathbf{p}_1 d\mathbf{p}_2}{(2\pi)^4}. \quad (3)$$

Here, $E[n(\mathbf{p})]$ is the ground-state energy of a normal Fermi liquid, $n(\mathbf{p}) = v^2(\mathbf{p})$, and $\kappa(\mathbf{p}) = v(\mathbf{p})\sqrt{1 - v^2(\mathbf{p})}$. It is assumed that the pairing interaction $\lambda_0 V(\mathbf{p}_1, \mathbf{p}_2)$ is weak. By minimizing E_{gs} with respect to $\kappa(\mathbf{p})$, we obtain the equation connecting the single-particle energy $\varepsilon(\mathbf{p})$ to $\Delta(\mathbf{p})$:

$$\varepsilon(\mathbf{p}) - \mu = \Delta(\mathbf{p})\frac{1 - 2v^2(\mathbf{p})}{2\kappa(\mathbf{p})}. \quad (4)$$

The single-particle energy $\varepsilon(\mathbf{p})$ is determined by the Landau equation, $\varepsilon(\mathbf{p}) = \delta E[n(\mathbf{p})]/\delta n(\mathbf{p})$ [10], and μ is the chemical potential. The equation for the superconducting gap $\Delta(\mathbf{p})$ takes the form

$$\Delta(\mathbf{p}) = -\int \lambda_0 V(\mathbf{p}, \mathbf{p}_1)\kappa(\mathbf{p}_1)\frac{d\mathbf{p}_1}{4\pi^2}. \quad (5)$$

If the coupling constant $\lambda_0 \longrightarrow 0$, the maximum value Δ_1 of the superconducting gap tends to zero, $\Delta_1 \longrightarrow 0$, and Eq. (4) reduces to that proposed in [11]:

$$\varepsilon(\mathbf{p}) - \mu = 0, \quad \text{if} \quad \kappa(\mathbf{p}) \neq 0, \quad (0 < n(\mathbf{p}) < 1); \quad p_i \le p \le p_f \in L_{FC}. \quad (6)$$

At $T = 0$, Eq. (6) defines a new state of a Fermi liquid with FC, for which the modulus of the order parameter $|\kappa(\mathbf{p})|$ has finite values in L_{FC} range of momenta $p_i \le p \le p_f$ occupied by FC, and $\Delta_1 \longrightarrow 0$ in L_{FC} [11, 13]. Such a state can be considered as superconducting, with an infinitely small value of Δ_1, so that the entropy of this state is equal to zero. This state, created by the quantum phase transition, disappears at $T > 0$ [13].

It follows from Eq. (6) that the system breaks into two quasiparticle subsystems: the first one in the L_{FC} range is occupied by quasiparticles with the effective mass $M^*_{FC} \propto 1/\Delta_1$, while the second by quasiparticles with finite mass M^*_L and momenta $p < p_i$. It is seen from Eq. (6) that, at the point of FCQPT $p_f \longrightarrow p_i \longrightarrow p_F$, the effective mass is as large as $1/\Delta_1$. Equation (6) acquires nontrivial solutions at $r_s = r_{FC}$, and FCQPT takes place if the Landau amplitudes depending on the density are positive and sufficiently large, so that the potential energy prevails over the kinetic energy and the transformation of the Fermi step function $n(p) = \theta(p_F - p)$ into the smooth function defined by Eq. (6) becomes possible [11].

Looking now for a simple situation where we can solve Eqs. (4) and (5) analytically, we assume that $\lambda_0 \neq 0$ and is small, so that we can employ the standard theory

of superconductivity. In that case, Δ_1 becomes finite, leading to a finite value of the effective mass M^*_{FC} in L_{FC}, which can be obtained from Eq. (4) [13]

$$M^*_{FC} \simeq p_F \frac{p_f - p_i}{2\Delta_1}, \tag{7}$$

while the effective mass M^*_L is disturbed weakly. Here, p_F is the Fermi momentum. It follows from Eq. (7) that the quasiparticle dispersion can be represented by two straight lines characterized by the effective masses M^*_{FC} and M^*_L, respectively. These lines intersect near the binding energy E_0 of electrons, which defines an intrinsic energy scale of the system:

$$E_0 = \varepsilon(\mathbf{p}_f) - \varepsilon(\mathbf{p}_i) \simeq \frac{(p_f - p_i)p_F}{M^*_{FC}} \simeq 2\Delta_1. \tag{8}$$

Equations (7) and (8) lead to the following general result for the maximum value Δ_1 coming from the contribution of FC [14]:

$$\Delta_1 \simeq \beta\varepsilon_F \frac{p_f - p_i}{p_F} \ln(1 + \sqrt{2}), \tag{9}$$

where $\varepsilon_F = p_F^2/2M^*_L$ is the Fermi energy and β is the dimensionless coupling constant. If the FC contribution to Δ_1 becomes comparatively small, then Δ_1 is given by the well-known relation proportional to the exponent of $(-1/\beta)$, $\Delta_1 \propto \exp(-1/\beta)$.

In fact, as is seen from Eqs. (4) and (5), a Fermi liquid with FC is absorbed by the superconducting phase transition and never exhibits the dispersionless plateau associated with $M^*_{FC} \longrightarrow \infty$. As a result, a Fermi liquid beyond the point of FCQPT can be described by two types of quasiparticles characterized by two finite effective masses M^*_{FC} and M^*_L, respectively, and by the intrinsic energy scale E_0 [13, 14]. It is reasonably reliable to suggest that we returned to the Landau theory by integrating out high-energy degrees of freedom and introducing the quasiparticles. The sole difference between the Landau Fermi liquid and the Fermi liquid having undergone FCQPT is that we have to increase the number of relevant low-energy degrees of freedom by adding both the new type of quasiparticles with the effective mass M^*_{FC} given by Eq. (7) and the energy scale E_0 given by Eq. (8). We also have to bear in mind that the properties of these new quasiparticles of the Fermi liquid with the FC cannot be separated from the properties of the superconducting state, as follows from Eqs. (7), (8), and (9). We may say that the quasiparticle system in the range L_{FC} becomes very "soft" and has to be considered as a strongly correlated liquid. On the other hand, the system's properties and dynamics are dominated by a strong collective effect having its origin in FCQPT and determined by the macroscopic number of quasiparticles in the range L_{FC}. Such a system cannot be disturbed by the scattering of individual quasiparticles and has the features of a quantum protectorate [13, 16]. On the other hand, as soon as the energy scale $E_0 \longrightarrow 0$, the system is driven back into the normal Landau Fermi liquid [14].

Recent studies of photoemission spectra have discovered an energy scale in the spectrum of low-energy electrons in cuprates that manifests itself as a kink in the single-particle spectra [17, 18]. The spectra in the energy range (200–0) meV can be described by two straight lines intersecting at the binding energy $E_0 \sim$ (50–70) meV [18]. Then, in underdoped copper oxides, there exists the pseudogap phenomenon, and the shape of single-particle excitations strongly deviates from that of a normal Fermi liquid (see, e.g., [1]). In the highly overdoped regime, slight deviations from the normal Landau Fermi liquid are observed [7, 19]. All these specific properties are naturally explained within the model proposed in [13, 14, 20] and allow one to relate the doping level or the charge-carrier density x regarded as the density of holes (or electrons) per unit area to the density of the Fermi liquid with FC. We assume that x_{FC} corresponds to the highly overdoped regime at which FCQPT takes place and introduce the effective coupling constant $g_{\text{eff}} \sim (x_{FC} - x)/x_{FC}$. According to the model, the doping level x at $x \le x_{FC}$ in metals is related to $(p_f - p_i)$ in the following way:

$$g_{\text{eff}} \sim \frac{(x_{FC} - x)}{x_{FC}} \sim \frac{p_f - p_i}{p_F} \sim \frac{p_f^2 - p_i^2}{p_F^2}. \tag{10}$$

Consider now two possible types of the superconducting gap $\Delta(\mathbf{p})$ given by Eq. (5) and defined by interaction $\lambda_0 V(\mathbf{p}, \mathbf{p}_1)$. If this interaction is dominated by a phonon-mediated attraction, the even solution of Eq. (5) with an s wave or $s + d$-mixed waves will have the lowest energy. If the pairing interaction $\lambda_0 V(\mathbf{p}_1, \mathbf{p}_2)$ is a combination of attractive and repulsive interaction, d-wave odd superconductivity can take place (see, e.g., [21]). But both s-wave even and d-wave odd symmetries lead to approximately the same values of the gap Δ_1 in Eq. (9) [14]. Therefore, the nonuniversal pairing symmetries in HTS are likely the results of the pairing interaction, and the d-wave pairing symmetry cannot be considered as absolutely necessary for HTS existence, in accord with experimental findings [5]. If only d-wave pairing existed, the transition from superconducting gap to pseudogap could take place, so that the superconductivity would be destroyed at the temperature T_c, with the superconducting gap being smoothly transformed into the pseudogap, which closes at some temperature $T^* > T_c$ [20, 22]. In the case of s-wave pairing, we can expect that the pseudogap phenomena do not exist, in accordance with experimental observation (see [5] and references therein).

We turn now to consideration of the maximum value of the superconducting gap Δ_1 as a function of the density x of mobile charge carriers. Being rewritten in terms of x and x_{FC} related to the variables p_i and p_f by Eq. (10), Eq. (9) takes the form

$$\Delta_1 \propto \beta(x_{FC} - x)x. \quad (11)$$

Here, we take into account that the Fermi level $\varepsilon_F \propto p_F^2$, the density $x \propto p_F^2$, and thus, $\varepsilon_F \propto x$. We can reliably assume that $T_c \propto \Delta_1$, because the empirically obtained simple bell-shaped curve $T_c(x)$ should reflect only a smooth dependence. Then, instead of Eq. (11) we have

$$T_c^{\alpha\gamma} \propto \beta^\alpha \beta^\gamma (x_{FC} - x)x. \quad (12)$$

In Eq. (12), we made the natural change $\beta = \beta^\alpha\beta^\gamma$, since the coupling constant β is fixed by the properties of the metal in question. Now it is seen that Eq. (12) coincides with Eq. (1), producing the universal optimal doping level $x_{\rm opt} = x_{FC}/2 = x_1/2$, in line with the experimental facts.

Let us make here few remarks. In [23], HTS was reported in such fullerides as C_{60}, $CHBr_3$, and $CHCl_3$. In the case of hole metals, the T_c^M ratios were measured for $C_{60}/CHBr_3$–$C_{60}/CHCl_3$–C_{60}, and the same ratios were also found for the respective electron metals [23]. It follows from Eq. (12) that, among these hole doped fullerides, the T_c^M ratios for $C_{60}/CHBr_3$–$C_{60}/CHCl_3$–C_{60} must be the same as in the case of the respective electron-doped fullerides, because the factor β^γ, related to hole or electron doping, drops out of the ratios. We believe that our calculations present evidence for the correctness of these experimental facts. Then, it was also shown that a Fermi liquid with FC, which exhibits strong deviations from the Landau Fermi liquid behavior, is driven into the Landau Fermi liquid by applying a magnetic field B. This field-induced Landau Fermi liquid behavior provides an $A + BT^2$ dependence for the resistivity ρ. A re-entrance into the strongly correlated regime, where ρ is a linear function of the temperature T, is observed if the magnetic field B decreases to some critical value $B_{\rm cr}$ [24]. We expect that similar behavior can be observed in the case of strongly overdoped high-temperature compounds at the temperatures $T \longrightarrow 0$. If the superconductivity is depressed by the critical field B_c, the T^2 behavior of the resistivity ρ can be restored at fields $B_{\rm cr} > B_c$. We assume that this behavior was observed in overdoped Tl-2201 compounds at millikelvin temperatures [7, 25].

As an example of the implementation of the previous analysis, let us consider the main features of a room-temperature superconductor. As follows from Eq. (9), $\Delta_1 \sim \beta\varepsilon_F \propto \beta/r_s^2$. Noting that FCQPT takes place in three-dimensional systems at $r_s \sim 20$ and in quasi-two-dimensional systems at $r_s \sim 8$ [26], we can expect that Δ_1 of 3D system comprises 10% of the corresponding maximum value of the 2D superconducting gap, reaching values as high as 60 meV for underdoped crystals with $T_c = 70$ [27]. On the other hand, it is seen from Eq. (9) that Δ_1 can be even larger, $\Delta_1 \sim 75$ meV, and one can expect $T_c \sim 300$ K in the case of the s-wave pairing, as follows from the simple relation $2T_c \simeq \Delta_1$. In fact, we can safely take $\varepsilon_F \sim 300$ meV, $\beta \sim 0.5$, and $(p_f - p_i)/p_F \sim 0.5$. Thus, we can conclude that a possible room-temperature superconductor should be a quasi-two-dimensional structure and an s-wave superconductor, in order to get rid of the pseudogap phenomena, which tremendously reduce the transition temperature. The density x of the mobile charge carriers must satisfy the condition $x \le x_{FC}$ and be flexible to reach the optimal doping level. It is worth noting that the coupling constant β must be sufficiently large, because FC giving rise to the order parameter $\kappa(\mathbf{p})$ does not produce by itself the gap Δ. For instance, the coupling constant can be enhanced by intercalation or by some kind of a disorder. It is pertinent to note that FCQPT can take place in three-dimensional metals at the ordinary metallic densities, as in heavy-fermion metals, where the effective mass is sufficiently large [24]. In that case, the potential energy can easily prevail over the kinetic energy, leading to FCQPT at sufficiently high densities. Then, we can expect the appearance of HTS if the coupling constant is large to ensure high values of the superconducting gap.

In summary, we have shown by a simple self-consistent analysis that the general features of the shape of the critical temperature T_c as a function of the density x of mobile carriers in metals and the value of the optimal doping $x_{\rm opt}$ can be understood within the framework of the theory of high-T_c superconductivity based on the FCQPT. We have demonstrated that neither the d-wave-pairing symmetry, the pseudogap phenomenon, nor the presence of the Cu–O_2 planes is of importance for the existence of the high-T_c superconductivity. Our theory explains the experimental observation that a strongly correlated Fermi liquid in heavily overdoped cuprates transforms into a normal Landau liquid. The main features of a room-temperature superconductor have also been outlined.

This work was supported in part by the Russian Foundation for Basic Research, project no. 01-02-17189.

REFERENCES

1. T. Timusk and B. Statt, Rep. Prog. Phys. **62**, 61 (1999).
2. C. C. Tsuei and J. R. Kirtley, Rev. Mod. Phys. **72**, 969 (2000).
3. C. M. Varma, Z. Nussinov, and Wim van Saarloos, Phys. Rep. **361**, 267 (2002).

4. N.-C. Yeh *et al.*, Phys. Rev. Lett. **87**, 087003 (2001); A. Biswas *et al.*, Phys. Rev. Lett. **88**, 207004 (2002); J. A. Skinta *et al.*, Phys. Rev. Lett. **88**, 207005 (2002).
5. J. A. Skinta *et al.*, Phys. Rev. Lett. **88**, 207003 (2002); C.-T. Chen *et al.*, Phys. Rev. Lett. **88**, 227002 (2002).
6. O. Gunnarsson, Rev. Mod. Phys. **69**, 575 (1997).
7. C. Proust *et al.*, Phys. Rev. Lett. **89**, 147003 (2002).
8. P. W. Anderson, Science **235**, 1196 (1987).
9. S. A. Kivelson *et al.*, Phys. Rev. B **35**, 8865 (1987).
10. L. D. Landau, Zh. Éksp. Teor. Fiz. **30**, 1058 (1956) [Sov. Phys. JETP **3**, 920 (1956)].
11. V. A. Khodel and V. R. Shaginyan, Pis'ma Zh. Éksp. Teor. Fiz. **51**, 488 (1990) [JETP Lett. **51**, 553 (1990)]; V. A. Khodel, V. R. Shaginyan, and V. V. Khodel, Phys. Rep. **249**, 1 (1994).
12. G. E. Volovik, Pis'ma Zh. Éksp. Teor. Fiz. **53**, 208 (1991) [JETP Lett. **53**, 222 (1991)].
13. M. Ya. Amusia and V. R. Shaginyan, Pis'ma Zh. Éksp. Teor. Fiz. **73**, 268 (2001) [JETP Lett. **73**, 232 (2001)]; M. Ya. Amusia and V. R. Shaginyan, Phys. Rev. B **63**, 224507 (2001).
14. M. Ya. Amusia, S. A. Artamonov, and V. R. Shaginyan, Pis'ma Zh. Éksp. Teor. Fiz. **74**, 495 (2001) [JETP Lett. **74**, 396 (2001)].
15. D. R. Tilley and J. Tilley, *Superfluidity and Superconductivity* (Hilger, Bristol, 1975).
16. R. B. Laughlin and D. Pines, Proc. Natl. Acad. Sci. U.S.A. **97**, 28 (2000); P. W. Anderson, cond-mat/0007185; cond-mat/0007287.
17. T. Valla *et al.*, Science **285**, 2110 (1999).
18. P. V. Bogdanov *et al.*, Phys. Rev. Lett. **85**, 2581 (2000); A. Kaminski *et al.*, Phys. Rev. Lett. **86**, 1070 (2001).
19. Z. Yusof *et al.*, Phys. Rev. Lett. **88**, 167006 (2002).
20. M. Ya. Amusia and V. R. Shaginyan, Phys. Lett. A **298**, 193 (2002).
21. A. A. Abrikosov, Phys. Rev. B **52**, R15738 (1995); cond-mat/9912394.
22. V. R. Shaginyan, Pis'ma Zh. Éksp. Teor. Fiz. **68**, 491 (1998) [JETP Lett. **68**, 527 (1998)]; S. A. Artamonov and V. R. Shaginyan, Zh. Éksp. Teor. Fiz. **119**, 331 (2001) [JETP **92**, 287 (2001)].
23. J. H. Schön, Ch. Kloc, and B. Batlogg, Science **293**, 2432 (2001).
24. Yu. G. Pogorelov and V. R. Shaginyan, Pis'ma Zh. Éksp. Teor. Fiz. **76**, 614 (2002).
25. A. P. Mackenzie *et al.*, Phys. Rev. B **53**, 5848 (1996).
26. V. A. Khodel, V. R. Shaginyan, and M. V. Zverev, Pis'ma Zh. Éksp. Teor. Fiz. **65**, 242 (1997) [JETP Lett. **65**, 253 (1997)].
27. N. Miyakawa *et al.*, Phys. Rev. Lett. **83**, 1018 (1999).

JETP Letters, Vol. 76, No. 11, 2002, pp. 656–659. Translated from Pis'ma v Zhurnal Éksperimental'noĭ i Teoreticheskoĭ Fiziki, Vol. 76, No. 11, 2002, pp. 779–783.

Spin-Wave Resonance in Three-Layer NiFe/Dy_xCo_{1-x}/NiFe Films as a Method for Detecting Structural Inhomogeneities in Amorphous Dy_xCo_{1-x} Layers

R. S. Iskhakov[1, *], V. A. Seredkin[1, 2], S. V. Stolyar[1], L. A. Chekanova[1], and V. Yu. Yakovchuk[1]

[1] *Kirenskiĭ Institute of Physics, Siberian Division, Russian Academy of Sciences, Akademgorodok, Krasnoyarsk, 660036 Russia*

** e-mail: rauf@iph.krasn.ru*

[2] *Krasnoyarsk State University, Krasnoyarsk, 660041 Russia*

Received October 21, 2002

The standing spin-wave spectrum was studied by spin-wave resonance in three-layer $Ni_{80}Fe_{20}/Dy_xCo_{1-x}/Ni_{80}Fe_{20}$ films with an amorphous interlayer of DyCo alloy in the region of compensation compositions. It is shown that the spin-wave resonance (SWR) spectrum in the geometry $\mathbf{k} \parallel M$ is observed only for a planar system with a DyCo layer of precompensation composition. In the $\mathbf{k} \perp M$ geometry, the SWR spectrum was observed for the DyCo systems with both pre- and postcompensation compositions. The exchange stiffness was analyzed as a function of the DyCo layer thickness to formulate a model of microheterophase structure for amorphous DyCo alloys in the compensation region, where the magnetic microstructure accounts for the dynamic and static magnetic characteristics of these materials. © *2002 MAIK "Nauka/Interperiodica".*

PACS numbers: 76.50.+g; 75.30.Ds; 75.70.-i

Amorphous RE(Dy, Gd, Tb)–TM(Fe, Co) alloys prepared as solid solutions in a broad concentration range are the brightest representatives of a class of amorphous ferrimagnets. The magnetization of these alloys is the sum of antiparallel magnetizations of the RE and TM sublattices. For this reason, the magnetization in these materials becomes zero at a certain compensation temperature (T_{comp}) or composition (x_{comp}). These materials, when prepared as films with near-compensation compositions, are ordinarily used as media for ultrahigh-density thermomagnetic recording [1]. In these films, the coercive force has a sharp maximum at the points T_{comp} (or x_{comp}). A deviation of only several degrees from T_{comp} (or of 2–3 at. % from x_{comp}) is sufficient for the coercive force to decrease by several times. The magnetic and atomic structures of these alloys were extensively studied in [2]. However, some of their properties, e.g., dynamic properties, are still poorly understood. For instance, studies of these films by ferromagnetic resonance (FMR) show that the FMR line width increases as the film composition (temperature) approaches x_{comp} (T_{comp}) and that no electromagnetic microwave absorption is observed (note that such behavior of the FMR parameters is common to all ferrimagnetic materials [3]).

In this work, we report the results of studying the dynamic magnetic properties of three-layer NiFe/Dy_xCo_{1-x}/NiFe films, in which the amorphous RE–TM layer is prepared in the region of compensation compositions.

It was established in our experiments that, first, a uniform alternating magnetic field excites standing spin waves in such a three-layer planar composite system. This gives evidence for the exchange interaction between the ferri- and ferromagnetic layers. Second, analysis of the dependence of effective spin-wave stiffness of such a system on the thickness of the ferrimagnetic layer allowed an indirect (but reliable) conclusion to be drawn about some features of the real magnetic and chemical structures of DyCo alloy films with compensation composition.

SAMPLE PREPARATION AND EXPERIMENTAL TECHNIQUE

Three-layer exchange-coupled $Ni_{80}Fe_{20}/Dy_xCo_{1-x}/Ni_{80}Fe_{20}$ films were prepared by thermal evaporation in a vacuum of 3×10^{-6} torr by sequential deposition of NiFe and DyCo layers on a cover glass substrate from three independent evaporators with ring cathodes. The thicknesses of the Permalloy layers in the planar system were d_{NiFe} = 1100 Å, and the thickness of the Dy_xCo_{1-x} layer was varied in the range from 100 to 800 Å. Single-layer 3000-Å-thick films of $Ni_{80}Fe_{20}$ Permalloy and single-layer 700-Å-thick Dy_xCo_{1-x} films were used as reference samples. The film thicknesses and chemical compositions were monitored by X-ray spectroscopic

analysis. The amorphous state of the DyCo layer was monitored by electron microscopy. The magnetooptical Kerr effect in fields up to 15 kOe was used as a test method for determining the pre-, post-, and compensation compositions of this layer. The same method (by studying the magnetooptical hysteresis loops at both the outer and inner surfaces of the DyCo layer) was used to establish that the DyCo films were compositionally homogeneous across their width (this was subsequently confirmed by Auger spectroscopy) and had perpendicular anisotropy. In our case, the room-temperature compensation composition was $Dy_{22}Co_{78}$. Two groups of planar structures were prepared: $Ni_{80}Fe_{20}/Dy_{20}Co_{80}/Ni_{80}Fe_{20}$ and $Ni_{80}Fe_{20}/Dy_{24}Co_{76}/Ni_{80}Fe_{20}$. Although the chosen compositions of the ferrimagnetic layer are on opposite sides of x_{comp}, they have close total saturation magnetizations $M_s \approx 80$ G, coercive forces $H_c \approx 4$–5 kOe, and perpendicular magnetic anisotropies $K_\perp \approx 3 \times 10^5$ erg/cm^3.

The spin-wave resonance (SWR) spectra of the planar NiFe/Dy_xCo_{1-x}/NiFe structures, single-layer NiFe films, and DyCo films were studied on a standard X-band spectrometer with the cavity fundamental frequency $f = 9.2$ GHz at room temperature. The films were placed at the antinode of an alternating magnetic field in the cavity and magnetized in two geometries (either perpendicular or parallel to the surface). In the first geometry, the resonance fields of SWR peaks (in ferromagnetic films) are known to satisfy the equation

$$H_n = \frac{\omega}{\gamma} + 4\pi M - \eta_{\text{eff}}\mathbf{k}_n^2, \quad \mathbf{k} \parallel M, \tag{1}$$

and, in the second geometry, the equation

$$H_n = \{[(\omega/\gamma)^2 + (2\pi M)^2]^{1/2} - 2\pi M\} - \eta_{\text{eff}}\mathbf{k}_n^2, \quad \mathbf{k} \perp M, \tag{2}$$

where $\omega = 2\pi f$ is the frequency, γ is the gyromagnetic ratio, $\eta_{\text{eff}} = 2A/M$ is the spin-wave stiffness depending on the exchange interaction constant A, M is the magnetization, and $k_n = (\pi/d)n$ ($n = 1, 2, 3, \ldots$ and d is the film thickness) is the wave vector of the nth mode in the SWR spectrum.

An important point is that the effective exchange stiffness η_{eff}, calculated by formula

$$\eta_{\text{eff}} = \frac{H_1 - H_n}{n^2 - 1}\left(\frac{d}{\pi}\right)^2, \tag{3}$$

is independent of the geometry of SWR experiment and must have the same value when recording the SWR peaks in both $\mathbf{k} \parallel M$ and $\mathbf{k} \perp M$ geometries. Indeed, the SWR spectra for the reference single-layer 3000-Å $Ni_{80}Fe_{20}$ films were recorded in both geometries: $\mathbf{k} \parallel M$ (14 peaks, including the surface peak) and $\mathbf{k} \perp M$ (5 peaks) (Fig. 1). Nevertheless, the η_{eff} values calculated by Eq. (3) proved to be nearly the same, with a good accuracy, for both cases and equal to $\eta_{\text{eff}} \approx 2.5 \times 10^{-9}$ Oe cm^2 (this value is consistent with the literature data [4]). No SWR absorption was observed for the reference $Dy_{20}Co_{80}$, $Dy_{22}Co_{78}$, or $Dy_{24}Co_{76}$ films.

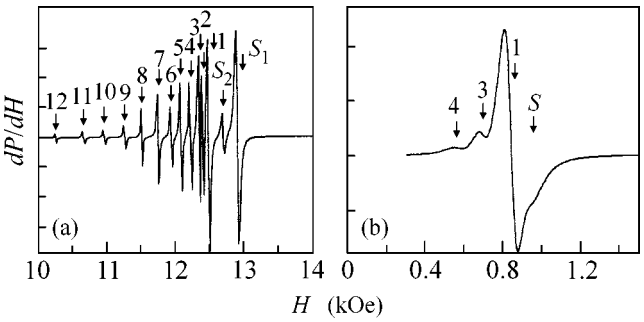

Fig. 1. SWR spectra of the reference $Ni_{80}Fe_{20}$ films in the dP/dH–H coordinates: (a) $\mathbf{k} \parallel M$ and (b) $\mathbf{k} \perp M$ (S indicates the surface modes and 1, 2, 3, … label the bulk modes).

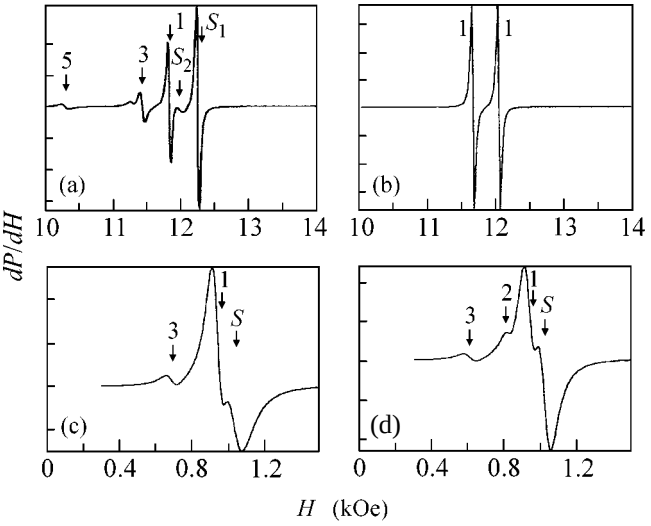

Fig. 2. SWR spectra of the three-layer $Ni_{80}Fe_{20}/Dy_xCo_{1-x}/Ni_{80}Fe_{20}$ films with a DyCo layer of (a, c) precompensation and (b, d) postcompensation composition in two geometries: (a, b) ($\mathbf{k} \parallel M$) and (c, d) ($\mathbf{k} \perp M$).

RESULTS AND DISCUSSION

Figure 2 shows the absorption spectra of the three-layer NiFe/Dy_xCo_{1-x}/NiFe films studied. The SWR spectrum of the planar $Ni_{80}Fe_{20}/Dy_{20}Co_{80}/Ni_{80}Fe_{20}$ system in the $\mathbf{k} \parallel M$ geometry is given in Fig. 2a, and the SWR spectrum of $Ni_{80}Fe_{20}/Dy_{24}Co_{76}/Ni_{80}Fe_{20}$ in the same geometry is given in Fig. 2b. The spectra are essentially different; in a planar system with the DyCo interlayer of precompensation composition, spin waves are excited, whereas, in a planar system with the DyCo

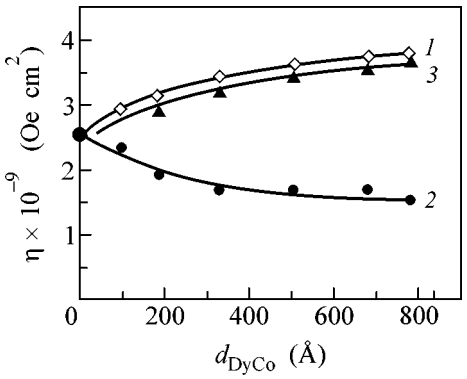

Fig. 3. Dependence of the effective spin-wave stiffness η_{eff} of the three-layer films on the thickness of the DyCo layer: (curve *1*) $\eta^{(\mathbf{k} \parallel M)}$ for $Ni_{80}Fe_{20}/Dy_{20}Co_{80}/Ni_{80}Fe_{20}$, (curve *2*) $\eta^{(\mathbf{k} \perp M)}$ for $Ni_{80}Fe_{20}/Dy_{20}Co_{80}/Ni_{80}Fe_{20}$, and (curve *3*) $\eta^{(\mathbf{k} \perp M)}$ for $Ni_{80}Fe_{20}/Dy_{24}Co_{76}/Ni_{80}Fe_{20}$.

interlayer of postcompensation composition, the spectrum is a superposition of the FMR spectra of the two ferromagnetic NiFe layers. Such a sizable distinction is caused by the exchange interaction between the layers and by the orientation of magnetization of the Co sublattice in the DyCo layer about the external magnetic field. Indeed, for a three-layer system with the interlayer of precompensation composition in the geometry of our experiment, the saturation magnetization vectors of the NiFe layers and the vectors of the overall DyCo magnetization and the magnetization of the Co sublattice are parallel to the external magnetic field *H*. Owing to the exchange interaction between the magnetic moments of transition metals, the Co magnetic moments are involved in the formation of coherent standing spin waves by microwave fields. In this case, standing waves with different *n* are sequentially excited upon varying *H* (Fig. 2a). At the same time, the configuration of the magnetization vectors in a three-layer system with the postcompensation DyCo interlayer is different. The magnetization vector of the Co sublattice in DyCo and the saturation magnetization vectors of the NiFe layers are antiparallel in the saturating fields *H*. As a result, due to the same exchange interaction, the spectrum of this system is an FMR doublet (Fig. 2b).

Unexpectedly, SWR-type absorption was observed in the $\mathbf{k} \perp M$ geometry (the external field is parallel to the film planes) for the planar systems with both pre- and postcompensation DyCo interlayers (Figs. 2c and 2d, respectively). The point is that the external field *H* (~1 kOe) in this geometry is appreciably weaker than the coercive force of the ferrimagnetic DyCo layer ($H_c \approx 4$–5 kOe). Consequently, this field cannot change the orientation of the total magnetization in the DyCo layer (as also the orientations of sublattice magnetizations). This became clear after the parameters of SWR spectra were changed by varying the thickness of the DyCo interlayer from 100 to 800 Å.

Figure 3 presents the effective exchange stiffness η_{eff} as a function of the thickness of the DyCo layer, as calculated by formula (3) from the experimental SWR spectra given by Eq. (1) for the planar $Ni_{80}Fe_{20}/Dy_{20}Co_{80}/Ni_{80}Fe_{20}$ system in the $\mathbf{k} \parallel M$ geometry (curve *1*) and by Eq. (2) for the $Ni_{80}Fe_{20}/Dy_{20}Co_{80}/Ni_{80}Fe_{20}$ and $Ni_{80}Fe_{20}/Dy_{24}Co_{76}/Ni_{80}Fe_{20}$ systems in the $\mathbf{k} \perp M$ geometry (curves *2* and *3*, respectively). In this figure, the exchange stiffness η_{eff} of the reference NiFe film is plotted on the ordinate axis (The formation of an effective exchange stiffness η_{eff} from the partial exchange stiffnesses η_i of the individual layers in a three-layer system is not discussed in this work).

One can see that the value of exchange stiffness η_{eff} of the $Ni_{80}Fe_{20}/Dy_{20}Co_{80}/Ni_{80}Fe_{20}$ system depends on the geometry of the SWR experiment; the calculated ratio η_{eff} ($\mathbf{k} \parallel M$) to η_{eff} ($\mathbf{k} \perp M$) is as high as two or even higher (curves *1, 2*), which far exceeds the experimental error (~10%). At the same time, one can see that the values of η_{eff} measured for the $Ni_{80}Fe_{20}/Dy_{24}Co_{76}/Ni_{80}Fe_{20}$ system in the $\mathbf{k} \perp M$ geometry (curve *3*) are close to their values in the system with the $Dy_{20}Co_{80}$ interlayer in the $\mathbf{k} \parallel M$ geometry. On the assumption that the exchange stiffness of a ferromagnetic film does not depend on the SWR geometry, one arrives at the conclusion that η_{eff} for curves *1* and *3* (Fig. 3) characterize the same magnetic material, while η_{eff} for curve *2* (Fig. 3) corresponds to a different magnetic material.

In our opinion, these results reflect the fundamental property of the amorphous state, namely, the intrinsic structural (fluctuative) inhomogeneity of amorphous alloys. Amorphous alloys are known to contain chemical (phase) nanoscale inhomogeneities. In particular, these inhomogeneities in amorphous ferromagnetic alloys cause fluctuations of exchange interaction and saturation magnetization, which was repeatedly detected experimentally (including the SWR method [5–8]). The magnitude of concentration fluctuations in these alloys can be as high as several atomic percent of mean concentration. This is the key factor that underlies the specific behavior of DyCo alloys in the compensation region. It is natural to introduce the notion of two magnetic phases for this alloy: the Φ_1 phase, for which the inequality $M_{Co} > M_{Dy}$ is satisfied locally and integrally, and the phase Φ_2, for which the inequality $M_{Dy} > M_{Co}$ is satisfied on the micro- and macrolevel. In the range of concentrations $x \ll x_{comp}$ or $x \gg x_{comp}$, the magnetic structure of the DyCo alloy is uniquely related to either Φ_1 or Φ_2. A basically different situation occurs in the region $x \approx x_{comp}$ under the condition that Δ_x falls within the range of fluctuations of local concentrations. In this case, the compensation point x_{comp} is determined from the requirement that the volumes of chaotically mixed Φ_1 and Φ_2 phases be the same. Then the pre- and postcompensation DyCo alloys are defined by

the inequalities $V_{\Phi_1} > V_{\Phi_2}$, $V_{\Phi_1} < V_{\Phi_2}$, respectively. According to simple estimates within the framework of percolation theory, one can state that the percolation near x_{comp} occurs through both Φ_1 and Φ_2 up to the concentrations x^* for which the condition $V_{\Phi_1} \approx 2V_{\Phi_2}$ or $2V_{\Phi_1} \approx V_{\Phi_2}$ is met.

The results of our experiment can naturally be interpreted in terms of the scheme proposed in Fig. 4 (the arrows in this figure indicate the possible magnetization orientations for 3*d* metals and the magnetization profile across the thickness of a three-layer film in the first SWR mode). Figure 4a describes the experimental situation presented in Fig. 2a. In Fig. 4a, Φ_1 and Φ_2 denote, respectively, the matrix and impurity phases in the $Dy_{20}Co_{80}$ layer. The magnetization M_{Co} in phase Φ_1 is aligned with both the external and perpendicular anisotropy fields. Due to the exchange interaction between transition metals, the magnetization of M_{Co} in the impurity phase Φ_2 should have the in-plane component in this case. For this reason, the coherent spin wave in the three-layer $Ni_{80}Fe_{20}/Dy_{20}Co_{80}/Ni_{80}Fe_{20}$ system propagates in the $\mathbf{k} \parallel M$ geometry through the phase Φ_1, and, in the $\mathbf{k} \perp M$ geometry, through the phase Φ_2 (Figs. 2c and 4c). Then the difference in the η_{eff} values for curves *1* and *2* in Fig. 3 is physically understandable, because the effective thickness in this case is contributed by the partial stiffnesses η_i of, in fact, different magnetic materials. The situation is the reverse for the $Ni_{80}Fe_{20}/Dy_{24}Co_{76}/Ni_{80}Fe_{20}$ system, where Φ_2 and Φ_1 are the matrix and impurity phases, respectively. In this case, the magnetization M_{Dy} of the Φ_2 phase is aligned with the external field in the SWR geometry ($\mathbf{k} \parallel M$), while the magnetization M_{Co} of this phase is antialigned with both external field and NiFe magnetizations. In such a situation, the coherent spin wave can be excited only in the NiFe layers (Figs. 2b and 4b). However, the magnetization M_{Co} of the impurity phase can contain the in-plane component. For this reason, the coherent spin wave in the three-layer $Ni_{80}Fe_{20}/Dy_{24}Co_{76}/Ni_{80}Fe_{20}$ system can propagate in the $\mathbf{k} \perp M$ geometry through the impurity phase Φ_1 (Figs. 2d and 4d). This explains the agreement between the η_{eff} values for curves *1* and *3* in Fig. 3.

Thus, the SWR studies of the three-layer planar $Ni_{80}Fe_{20}/Dy_xCo_{1-x}/Ni_{80}Fe_{20}$ systems containing amorphous DyCo interlayer in the region of compensation compositions enable one not only to judge indirectly (though, in our opinion, reliably) the inhomogeneous structure of these amorphous DyCo films but also propose a model of microheterophase organization of this industrially important class of magnetic materials.

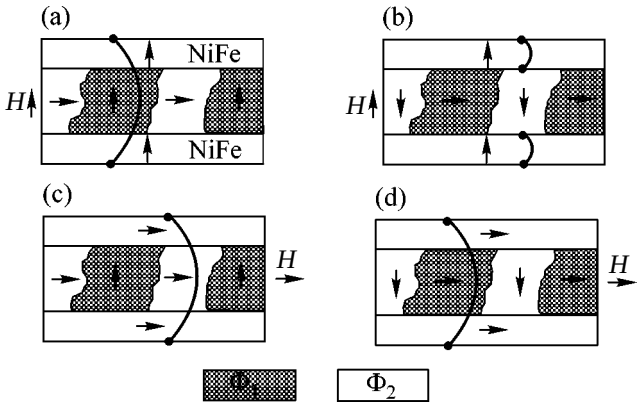

Fig. 4. Configuration of the magnetization vectors for 3*d* metals in the three-layer films and the first standing-wave mode: (a, c) precompensation and (b, d) postcompensation DyCo compositions.

This work was supported by the Russian Foundation for Basic Research, project no. 02-02-97717.

REFERENCES

1. R. W. Chantrell, A. Lyberatos, M. El-Hilo, and K. O. Grady, J. Appl. Phys. **76**, 6407 (1994).
2. K. H. J. Buschow, in *Ferromagnetic Materials*, Ed. by E. P. Wolhfarth and K. H. J. Buschow (Elsevier, New York, 1988), Vol. 4.
3. A. G. Gurevich, *Magnetic Resonance in Ferrites and Antiferromagnets* (Nauka, Moscow, 1973).
4. G. I. Rusov, Fiz. Tverd. Tela (Leningrad) **9**, 196 (1967) [Sov. Phys. Solid State **9**, 146 (1967)].
5. V. A. Ignatchenko, R. S. Iskhakov, L. A. Chekanova, and N. S. Chistyakov, Zh. Éksp. Teor. Fiz. **75**, 876 (1978) [Sov. Phys. JETP **48**, 328 (1978)].
6. R. S. Iskhakov, M. M. Brushtunov, A. S. Chekanov, *et al.*, Fiz. Met. Metalloved. **79**, 122 (1995).
7. R. S. Iskhakov, S. V. Stolyar, L. A. Chekanova, and V. S. Zhigalov, Fiz. Tverd. Tela (St. Petersburg) **43**, 1072 (2001) [Phys. Solid State **43**, 1108 (2001)].
8. R. S. Iskhakov, D. E. Prokof'ev, L. A. Chekanova, and V. S. Zhigalov, Pis'ma Zh. Tekh. Fiz. **27** (8), 81 (2001) [Tech. Phys. Lett. **27**, 344 (2001)].

Translated by V. Sakun

JETP Letters, Vol. 76, No. 11, 2002, pp. 660–663. Translated from Pis'ma v Zhurnal Éksperimental'noĭ i Teoreticheskoĭ Fiziki, Vol. 76, No. 11, 2002, pp. 784–787.

Electron-Filling Kinetics of 2D States on a Helium Film

V. B. Shikin

Institute of Solid-State Physics, Russian Academy of Sciences, Chernogolovka, Moscow region, 142432 Russia

Received October 10, 2002; in final form, October 24, 2002

The details of charging a free liquid-helium surface with electrons are discussed. It is shown that the thickness of the helium film varies during this process and gradually decreases under the action of electron pressure on the helium surface. In turn, the pressure depends on the film thickness. Hence, the self-consistent kinetic problem arises with characteristic relaxation time τ mainly of hydrodynamic origin (viscous adjustment of the film thickness to the variable electron pressure). The value of τ is quite sensitive to the film thickness d ($\tau \propto d^3$). In the most representative interval 10^{-1} cm $> d > 10^{-4}$ cm, τ varies in the range 10^{-3} s $\le \tau \le 10^{+8}$ s. The situation is most intriguing in the vicinity of the critical point (at the critical point, the charged helium film becomes unstable). As it is approached, τ increases to infinity. © *2002 MAIK "Nauka/Interperiodica".*

PACS numbers: 73.50.Bk; 73.25.+i

The saturation regime is one of the most popular regimes of filling 2D electronic states with electrons at the helium surface. In this regime, an external electron source operates continuously and replenishes the helium surface to a level providing the compensation of an external field by the self-field of electrons above the helium. The excessive electrons are "removed" to the upper metallic electrode (Fig. 1). The steady-state density of 2D surface electrons is a known function of the potential difference between the control electrodes in the cell (Fig. 1) and its geometry (see Eq. (3)). Therein lies the merit of the saturation regime. The recent example of manipulations with a charged 2D system in the saturation regime is described in [1].

The filling of a helium surface with electrons is an intriguing kinetic process, whose details have not been discussed to date. The problem deserves particular attention, because the characteristic relaxation times are rather long, especially for thin helium films and under conditions close to critical (at the critical point, the charged helium surface loses stability). It is the purpose of this work to formulate the corresponding kinetic problem in the simplest analytic form and to analyze it qualitatively.

1. Consider the system shown in Fig. 1. Electric fields E_- above and E_+ below the helium surface charged with electron density n_s are

$$E_- = \frac{V}{D} - 4\pi\sigma\frac{d}{D}, \tag{1}$$

$$E_+ = \frac{V}{D} + 4\pi\sigma\frac{(D-d)}{D}, \tag{2}$$

where $\sigma = en_s$ and V is the potential difference between the cell plates (Fig. 1).

If an external field above the helium is completely screened, i.e., if $E_- = 0$ and, hence,

$$4\pi\sigma = V/d, \tag{3}$$

then the electric field E_+ is

$$E_+ = V/d. \tag{4}$$

For given d_o and V, where d_o is the thickness of the helium film in the absence of an external field, the helium surface is deflected under the action of electron pressure $P_{\text{el}} = E_+^2/8\pi$ to a depth

$$\xi_\infty = d - d_o, \tag{5}$$

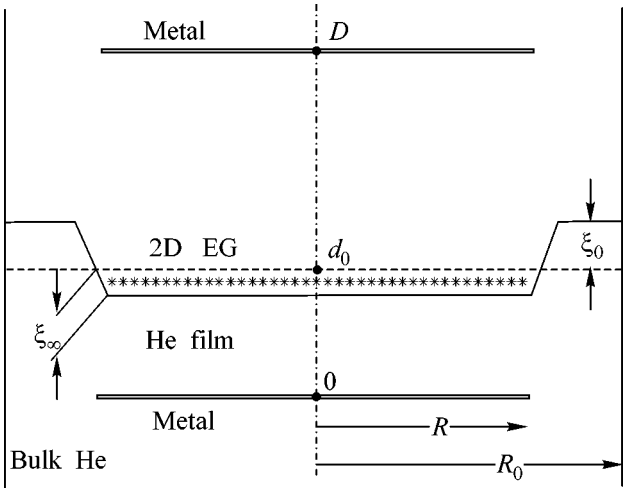

Fig. 1. Scheme of geometrical notation for a cell with 2D electron system. The positions of the neutral film boundary d_o and the deformations ξ_o and ξ_∞ are also shown.

0021-3640/02/7611-0660$22.00

whose value is determined by the conditions for mechanical equilibrium and retention of the total volume of liquid,

$$\rho g\xi_\infty + \frac{V^2}{8\pi d_o^2} = \rho g\xi_o, \tag{6}$$

$$R^2\xi_\infty + (R_o^2 - R^2)\xi_o = 0, \quad R_o > R, \quad |\xi_\infty| \ll d_o. \tag{7}$$

Here, ρ and g are the density of liquid helium and the gravitational acceleration, respectively; R is the radius of the electron disc at the helium surface; and R_o and ξ_o are the radius and deformation of the liquid surface beyond the electron disc (Fig. 1). The simultaneous solution of Eqs. (6) and (7) gives

$$\xi_\infty = -\frac{V^2}{8\pi\rho g^* d_o^2}, \quad g^* = g\left(1 + \frac{R^2}{R_o^2 - R^2}\right). \tag{8}$$

Turning to the kinetics, we note that the potential difference V can be introduced into the problem almost instantly (on the time scale of interest). The saturation of the liquid surface with 2D electrons is also a rather fast process (at every instant of time, Eq. (3) with the time-dependent film thickness $d(t)$ is valid). The hydrodynamic change in $d(t)$ is the longest process. Apart from the "horizontal" kinetics, the rate of liquid transfer to a reservoir can also be influenced by the throughput of the vertical part (if it exists) of the film. The terminology for the neutral situation—horizontal and vertical film components and a reservoir—is clarified in Fig. 2 (for simplicity, the control electrodes and the 2D system itself are not shown in this figure). The dependence of the film thickness d on the distance h between the substrate base and the reservoir level are given by the expression

$$f_{\text{ret}}/d^4 = \rho g(d - h). \tag{9}$$

Here, g is the gravitational acceleration and f_{ret} is the van der Waals constant with allowance made for retardation.

As long as $h > 0$, the thickness of the helium film only slightly exceeds its level in the reservoir:

$$d \simeq h + f_{\text{ret}}/(\rho g h)^4. \tag{9a}$$

The substrate is completely dipped into the liquid.

However, if $h < 0$, definition (9) tends to the known asymptotic expression

$$d^4 \simeq f_{\text{ret}}/(\rho g h_m), \quad h_m = |h|. \tag{9b}$$

In this limit, the vertical walls of the substrate rise above the level of bulk helium but still remain covered with a thin helium film, which connects its horizontal part with the reservoir.

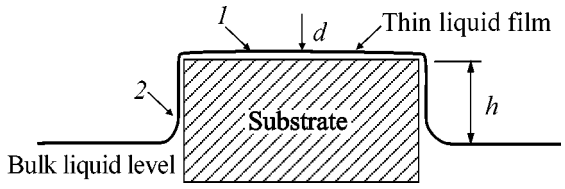

Fig. 2. Scheme of a cell without its electrical part. The presence of horizontal (*1*) and vertical (*2*) film components are illustrated.

For the thicknesses

$$\kappa d_o \le 1, \quad \kappa^2 = \rho g/\alpha, \tag{10}$$

which are only considered in what follows (α is the surface tension coefficient), one can manipulate the film thickness using approximation (9a). There are no vertical film parts in this formula (this fact was already used in Eqs. (6) and (7) and in Fig. 1), so that the hydrodynamic kinetics is controlled by the rate of liquid escape from the electron "piston" with radius R. We deliberately use the term piston. It implies that the 2D electron density at the liquid film between the control electrodes remains uniform during the course of changing $d(t)$. This purely electrostatic statement (the charge density in a flat capacitor is constant, except for the edge effects, which are neglected below because $R \gg d$) is corroborated by direct experiments, which provide evidence that the deformation of a helium surface under the action of electron pressure is uniform both in the static regime [2] and under parametric excitation [3].

Therefore, the problem is reduced to the well-known problem (see, e.g., [4]) of viscous liquid flow from under a flat piston. In this problem, the rate $\dot{\xi}$ of a change in film thickness is related to the force F stimulating liquid viscous flow by the expression (see [4] and Eq. (A5) in the Appendix)

$$F = \frac{3\pi\eta R^4\dot{\xi}}{8d^3}. \tag{11}$$

Here, η is the helium dynamic viscosity. The sum

$$F = -\pi R^2\left[\rho g^*\xi(t) + \frac{V^2}{8\pi(d_o + \xi(t))^2}\right] \tag{12}$$

plays the role of force F. By equating it to zero in the limit $d_o \gg |\xi_\infty|$, one can determine ξ_∞ in Eq. (6).

Writing

$$\xi(t) = \xi_\infty + \delta\xi(t) \tag{13}$$

and linearizing Eqs. (11) and (12) with respect to the addition $\delta\xi(t)$, one gets

$$\delta\dot{\xi} = \frac{8d_o^3}{3\eta R^2}\left(\frac{V^2}{4\pi d_o^3} - \rho g^*\right)\delta\xi, \qquad (14)$$
$$\delta\xi(0) = -\xi_\infty, \quad \delta\xi(+\infty) \longrightarrow 0.$$

The right-hand side of Eq. (14) contains, among other things, the term

$$\left(\rho g^* - \frac{V^2}{4\pi d_o^3}\right).$$

The charged surface loses stability, under the condition $\kappa d_o \ll 1$, when this expression turns to zero upon the variation of parameters V and d_o [5].

The solution to Eq. (14)

$$\delta\xi(t) = -\xi_\infty \exp(-t/\tau),$$
$$\tau^{-1} = \frac{8d_o^3}{3\pi\eta R^2}\left(\rho g^* - \frac{V^2}{4\pi d_o^3}\right) \qquad (15)$$

determines, in particular, the characteristic relaxation time τ. In the case $\rho g^* \gg V^2/4\pi d_o^3$, this time has hydrostatic origin:

$$\tau^{-1} \simeq \frac{8d_o^3}{3\pi\eta R^2}\rho g^*. \qquad (16)$$

For $\rho \simeq 0.146$ g/cm^3, $g^* \simeq g$ (when $R \ll R_o$), $\eta = \rho\nu$, $\nu \simeq 1.5 \times 10^{-3}$ cm^2/s, $R \sim 1$ cm, and $d_o \leq 0.1$ cm, τ scales as $\tau \geq 10^{-3}$ s. Regime (6) corresponds to the film thickness lying in the range 10^{-1} cm $\geq d_o \geq 10^{-4}$ cm. As d approaches its lower limit $d_o \geq 10^{-4}$ cm, the relaxation time shifts to $\tau \geq 10^{+8}$ s. In other words, in the vicinity of $d \geq 10^{-4}$ cm, the equilibrium value ξ_∞ (8) is achieved over a long time.

Of interest is the sensitivity of relaxation time (15) to the difference $(\rho g^* - V^2/4\pi d_o^3)$. In the vicinity of the stability boundary of the helium film, where

$$V_{cr}^2/4\pi = \rho g^* d_o^3, \qquad (17)$$

τ tends to infinity. This fact may be a reason for the quantitative discrepancy between the prediction given by Eq. (17) in [5] and the experiment [6], which confirms that the critical electric field V_{cr}^2/d_o^2 linearly drops with decreasing thickness d_o but systematically overstates the critical value of d_o.

2. In addition to the $\delta\xi(t)$ kinetics given by Eq. (15), whose details can be studied by capacitive methods, the results presented above also refer to the electron population at the helium film. The point is that, for a given V, the electron density changes with time, because $n_s \propto V/(d_o + \xi(t))$. If $\xi(t)$ is a sizable fraction of d_o (it will be seen below that such is indeed the case), then n_s becomes variable.

We first use the above information to determine the scale of n_s variation. The simultaneous use of Eq. (8), which is valid over the whole region of film stability, and Eq. (17) for the stability boundary gives the following estimate for the maximal deformation of the charged film:

$$\xi_\infty^{cr} = -d_o/2. \qquad (18)$$

This deformation cannot be regarded as small, so that Eqs. (8) and (17) near the stability boundary should be refined.

Equation (8) now takes the form

$$\rho g^* \xi_\infty + \frac{V^2}{8\pi(d_o + \xi_\infty)^2} = 0, \qquad (19)$$

while the equivalent to Eq. (17) is

$$V_{cr}^2/4\pi = \rho g^* (d_o + \xi_\infty^{cr})^3. \qquad (20)$$

The simultaneous solution of Eqs. (19) and (20) at the critical point yields for ξ_∞^{cr}

$$\xi_\infty^{cr} = -d_o/3. \qquad (21)$$

Although this deformation is smaller than that given by Eq. (18), it provides a change of approximately 30% from the initial to finite n_s value, which is asymptotically slowly established with time. Expression (21) also implies that the linearization (14) under near-critical conditions is not very reliable (the requirement $|\xi_\infty^{cr}| \ll d_o$ is not fulfilled), at least, at the initial stage of adjustment.

The more general equation for $\dot{\xi}$ reads

$$\dot{\xi} = -\frac{8(d_o + \xi)^3}{3\eta R^2}\left[\rho g \xi + \frac{V^2}{8\pi}\frac{1}{(d_o + \xi)^2}\right], \qquad (22)$$
$$\xi(0) = 0, \quad \xi(+\infty) = \xi_{+\infty},$$

where ξ_∞ is given by Eq. (19). At the initial stage,

$$\dot{\xi} \simeq -\frac{V^2}{3\pi\eta R^2}(d_o + \xi), \quad \rho g \xi \ll \frac{V^2}{8\pi}\frac{1}{(d_o + \xi)^2}, \qquad (23)$$
$$\xi(0) = 0,$$

so that

$$\xi(t) = -d_o[1 - \exp(-t/\tau_o)],$$
$$\tau_o^{-1} = V^2/3\pi\eta R^2. \qquad (24)$$

Regime (24) matches with the asymptotic behavior

$$\zeta(t) = \xi_\infty + \delta\zeta(t),$$

$$\delta\zeta(t) = \delta\zeta_o \exp(-t/\tau), \quad \tau^{-1} = \frac{8d_*^3}{3\pi\eta R^2}\left(\rho g^* - \frac{V^2}{4\pi d_*^3}\right),$$

$$d_* = d_o + \xi_\infty, \tag{25}$$

$$\delta\xi(0) = -\xi_\infty + \xi(t_*), \quad \delta\xi(+\infty) \longrightarrow 0,$$

where ξ_∞ is given by Eq. (16), $\xi(t)$ is from Eq. (24), the time t_* is determined from the requirement

$$\rho g \xi(t_*) + V^2/(8\pi d_o^2) \simeq 0, \tag{26}$$

and time in Eq. (25) is counted from t_*.

Thus, the equilibrium in near-critical kinetics is established in two stages. At the initial stage, on the interval $0 < t \le t_*$, the kinetics is exponential with the characteristic relaxation time τ_o given by Eq. (24) with t_* determined from Eq. (26). Subsequently, the kinetics is again exponential but with the relaxation time (25).

In summary, one can state that filling the helium surface with electrons is an intriguing problem and deserves special attention. Apart from the 2D electronic aspect, this problem is helpful in studying the details of spinodal decay kinetics at its initial stage. Indeed, our problem involves all attributes of spinodal kinetics (see, e.g., [7–10]): the presence of an instability point, the possibility of a fast transition from the stable to the decaying state, the exponential decay at the initial stage, etc.

APPENDIX

The problem of radial motion of a viscous liquid between two pistons approaching each other is well known (see, e.g., [4]). Since the boundary conditions in our variant are nonstandard (compared to the literature conditions), we present below the details of its solution.

The equations of motion of a viscous liquid under a pressure of electron piston have the form at $v_z \ll v_r$ and $\partial v_r/\partial r \ll \partial v_r/\partial z$

$$\eta \frac{\partial^2 v_r}{\partial z^2} = \frac{\partial p}{\partial r}, \quad \frac{\partial p}{\partial z} = 0, \tag{A1}$$

$$\frac{1}{r}\frac{\partial (r v_r)}{\partial r} + \frac{\partial v_z}{\partial z} = 0 \tag{A2}$$

with the boundary conditions

$$v_r = v_z = 0, \text{ at } z = 0, \quad r \le R,$$

$$\partial v_r/\partial z = 0, \quad v_z = -u, \text{ at } z = d, \quad r \le R,$$

$$p = p_o, \quad r \ge R.$$

Here, d is the thickness of the helium film, u is the rate of its variation under the action of external forces, p_o is the external pressure beyond the cylindrically symmetric capacitor, and η is the first viscosity of the liquid (helium). The second of these boundary conditions satisfies the requirement $\sigma_{rz}(z = d) = 0$ (this tensor component of viscous stress is zero at the free surface of the liquid film).

From Eqs. (A1) with the above boundary conditions, it follows that

$$\eta v_r = -z(d - z/2)\partial p/\partial r. \tag{A3}$$

Integrating Eq. (A2), one gets

$$u = \frac{1}{r}\frac{\partial}{\partial r}\int_o^d r v_r dz = -\frac{d^3}{3\eta r}\frac{\partial}{\partial r}\left(r\frac{\partial p}{\partial r}\right). \tag{A4}$$

Hence,

$$p = p_o + \frac{3\eta u}{4d^3}(R^2 - r^2),$$

so that the total drag force F is

$$F = 3\pi\eta u R^4/(8d^3). \tag{A5}$$

This expression was used in Eq. (11) of the main text.

REFERENCES

1. A. Levchenko, E. Teske, G. Kolmakov, *et al.*, Pis'ma Zh. Éksp. Teor. Fiz. **65**, 547 (1997) [JETP Lett. **65**, 572 (1997)].
2. R. Crandall, Surf. Sci. **58**, 266 (1976).
3. P. Leiderer, Physica B (Amsterdam) **186**, 93 (1984).
4. L. D. Landau and E. M. Lifshitz, *Course of Theoretical Physics*, Vol. 6: *Fluid Mechanics*, 3rd ed. (Nauka, Moscow, 1986; Pergamon, New York, 1987).
5. D. Chernikova, Fiz. Nizk. Temp. **2**, 1374 (1976) [Sov. J. Low Temp. Phys. **2**, 669 (1976)].
6. A. Volodin, M. Khaĭkin, and V. Édel'man, Pis'ma Zh. Éksp. Teor. Fiz. **26**, 707 (1977) [JETP Lett. **26**, 543 (1977)].
7. J. W. Chan, Acta Metall. **9**, 795 (1961); Acta Metall. **10**, 179 (1962).
8. H. E. Cook, Acta Metall. **18**, 297 (1970).
9. J. S. Langer, M. Baron, and H. D. Miller, Phys. Rev. A **11**, 1417 (1975).
10. A. Olemskoĭ and I. Koplyk, Usp. Fiz. Nauk **165**, 1105 (1995) [Phys. Usp. **38**, 1061 (1995)].

Translated by V. Sakun

JETP Letters, Vol. 76, No. 11, 2002, pp. 664–669. Translated from Pis'ma v Zhurnal Éksperimental'noĭ i Teoreticheskoĭ Fiziki, Vol. 76, No. 11, 2002, pp. 788–793.

Magnetic Collapse and the Change of Electronic Structure of $FeBO_3$ Antiferromagnet under High Pressure

V. A. Sarkisyan[1], I. A. Troyan[2], I. S. Lyubutin[1, *], A. G. Gavrilyuk[2], and A. F. Kashuba[1]

[1] *Shubnikov Institute of Crystallography, Russian Academy of Sciences, Leninskiĭ pr. 59, Moscow, 117333 Russia*

** e-mail: lyubutin@ns.crys.ras.ru*

[2] *Institute of High-Pressure Physics, Russian Academy of Sciences, Troitsk, Moscow region, 142190 Russia*

Received October 25, 2002

The effect of high pressures up to 60 GPa on single-crystal and polycrystalline samples of iron borate $^{57}FeBO_3$ was studied by Mössbauer absorption spectroscopy (^{57}Fe nuclei) in a diamond anvil cell. Magnetic field H_{hf} at the ^{57}Fe nuclei increases with pressure but abruptly drops to zero at 46 ± 2 GPa, indicating the crystal transition from the antiferromagnetic to nonmagnetic state. This is accompanied by an abrupt change in the isomer shift and quadrupole splitting. Their values in the high-pressure phase are evidence for the transition of Fe^{+3} ions from a high-spin ($S = 5/2$, $^6A_{1g}$) to low-spin ($S = 1/2$, $^6T_{2g}$) state (spin crossover). This correlates with an abrupt decrease in the unit-cell volume (by ~9%) and optical gap. The change of the magnetic and electronic structures is explained by Mott's transition with rupturing of strong *d–d*-electron correlations. © *2002 MAIK "Nauka/Interperiodica"*.

PACS numbers: 75.80.+q; 75.50.Ee; 76.80.+y; 75.30.Kz

1. INTRODUCTION

Iron borate $FeBO_3$ is among those rare materials that are transparent in the visible region and possess spontaneous magnetization at room temperature. For this reason, light can be modulated in it by magnetooptical effects. $FeBO_3$ has the rhombohedral calcite structure belonging to the space group $R\bar{3}c$ (D_{3d}^6) [1, 2]. It is an antiferromagnet with weak ferromagnetism and Néel point $T_N = 348$ K [2]. Its unit cell contains two formula units. The iron ions Fe^{3+} have an octahedral environment formed by oxygen ions. The interion distances are (Fe–O) = 2.028 Å and (Fe–Fe) = 3.601 Å, and the (O–Fe–O) bond angles are equal to 91.82° and 88.18° [3]. Therefore, the iron environment by six oxygen ions is almost cubic. At normal pressure, the magnetic moments of the two iron sublattices lie in the basal plane (111) and are almost antiparallel. Under normal conditions, $FeBO_3$ is an insulator with an optical gap of ~2.9 eV [4].

The transition from the magnetic to nonmagnetic state was recently observed in iron borate at a pressure of 46 ± 2 GPa by nuclear forward scattering (NFS) of synchrotron radiation [5], and the structural phase transition was observed in [6] by the X-ray method at 52 ± 2 GPa. Inasmuch as the NFS spectra were recorded for a $^{57}FeBO_3$ single crystal, whereas the X-ray spectra were obtained for a polycrystal, it remains unclear whether the difference in the pressures of magnetic and structural transitions has a physical origin or is a "specimen effect."

In this work, Mössbauer absorption spectra of a single crystal of iron borate $^{57}FeBO_3$ and its polycrystalline samples were studied to elucidate the nature of these transitions and their relation to the electronic structure of Fe ions. Samples were exposed to high pressures up to 60 GPa in a diamond anvil cell.

2. EXPERIMENTAL

Transparent high-quality light-green-colored $FeBO_3$ crystals enriched to 96% with ^{57}Fe isotope were grown by the flux method. Crystals were platelets whose planes coincided with their basal plane (111). In high-pressure experiments, a $^{57}FeBO_3$ single crystal with a size of about $80 \times 40 \times 10$ μm was placed in a high-pressure diamond anvil cell. The basal plane (111) of the single crystal was oriented perpendicular to the direction of a gamma-ray quantum beam. Polycrystalline samples were obtained by grinding the single crystal in an agate crucible. The working area of the diamond anvils was about 300 μm in diameter, and the hole diameter in a gasket where the samples were placed was about 100 μm. The chamber working volume was filled with a poly(ethyl siloxane) (PES-5) liquid to produce quasihydrostatic pressure. The pressure was measured using the ruby fluorescence line. For this purpose, apart from the $FeBO_3$ sample, several 10-μm ruby pieces were placed in the chamber at various distances from the center to estimate the pressure gradient.

The ^{57}Fe Mössbauer spectra were recorded at room temperature on a standard spectrometer operating in a constant acceleration mode and interfaced to a personal

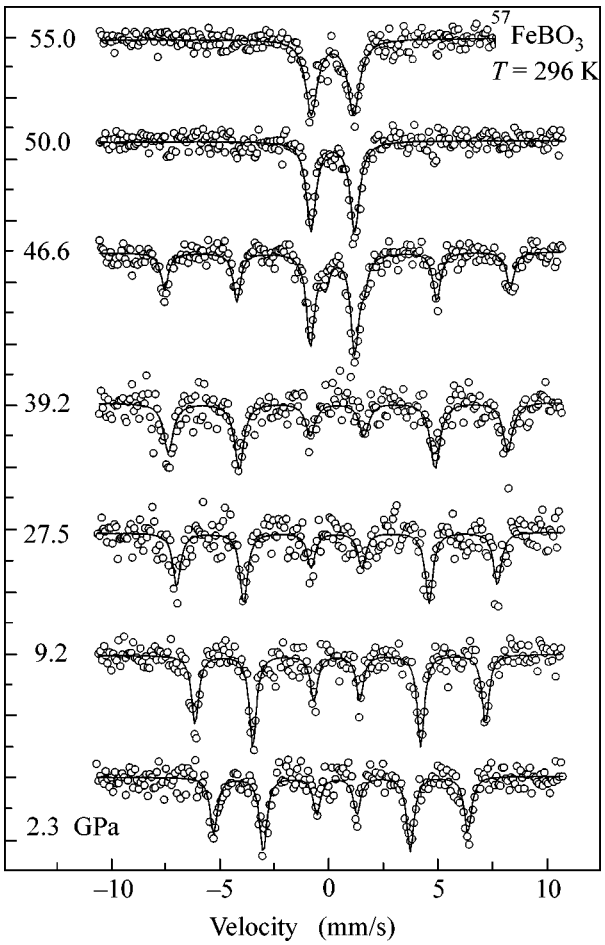

Fig. 1. Typical room-temperature Mössbauer spectra of a $^{57}FeBO_3$ single crystal for some pressures below and above the phase transition. Solid lines correspond to calculations.

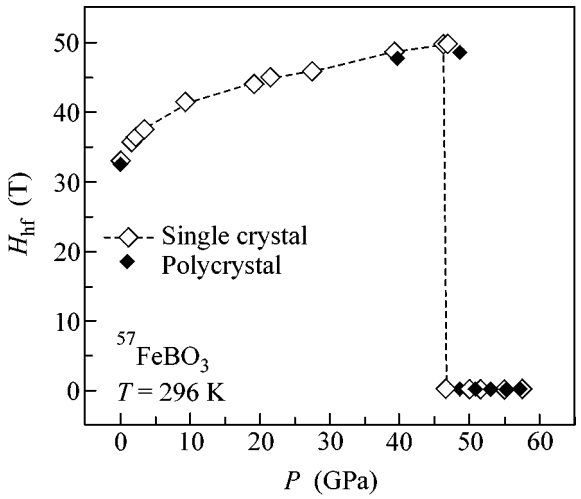

Fig. 2. Pressure dependence of the hyperfine magnetic field at the ^{57}Fe nucleus in iron borate at room temperature. Light symbols correspond to the single-crystal sample and dark symbols are for polycrystal.

computer. The ^{57}Co(Rh) source with an activity of about 100 mCi was at room temperature. To gain reliable statistics, the accumulation time for one spectrum was as long as two weeks, which required enhanced requirements to be placed on the operation stability of apparatus. The spectra were processed using the programs developed in the Shubnikov Institute of Crystallography, Russian Academy of Sciences.

3. RESULTS

The Mössbauer spectra of a $^{57}FeBO_3$ single crystal in the pressure range from normal to 55 GPa are presented in Fig. 1. At $P < 46$ GPa, the Zeeman sextet is typical for a magnetic hyperfine splitting of the ^{57}Fe nuclear levels in an effective magnetic field H_{hf}. This is evidence that all iron ions are in equivalent crystallographic positions. The intensity ratio of the six resonance lines is close to 3 : 4 : 1 : 1 : 4 : 3. This signifies that the magnetic moments of the two iron sublattices in this pressure range lie in the basal plane of the sample perpendicularly to the wave vector of a gamma-ray quantum.

With the buildup of pressure, the splitting of resonance lines increases because of an increase in the magnetic field H_{hf} at the iron nuclei. In the range $0 < P < 44$ GPa, the field H_{hf} increases nonlinearly from 34.1 to 48.1 T (Fig. 2). This is likely due to an increase in the exchange interaction as a result of the decrease in the interion Fe–O–Fe distances and, accordingly, rise in the Néel point. At $P = 46 \pm 2$ GPa, the field H_{hf} abruptly drops to zero, indicating the magnetic-moment collapse and the transition of a $FeBO_3$ antiferromagnet to the nonmagnetic state. One can see from Fig. 1 that the magnetic and nonmagnetic phases coexist in the spectrum at $P = 46.3$ GPa, likely owing to the pressure gradient. In a high-pressure (HP) nonmagnetic phase, the Mössbauer spectra retain an asymmetrical doublet with the quadrupole splitting $QS \approx 2$ mm/s and the isomer shift $IS \approx 0.06$ mm/s (with respect to the metallic iron). As the pressure is reduced, the magnetic hyperfine splitting is restored without a noticeable hysteresis after the transition through the critical point.

The pressure dependences of the *QS* and *IS* parameters are presented in Figs. 3 and 4. In the low-pressure (LP) phase, i.e., below the magnetic transition pressure, the parameters H_{hf}, *QS*, and *IS* are typical of the Fe^{3+} ions in the high-spin (HS) $3d^5$ state ($S = 5/2$; $^6A_{1g}$). However, at $P > 46$ GPa, the magnetic field H_{hf} drops to zero (Fig. 2), and the *QS* and *IS* values also change jumpwise (Figs. 3, 4), evidencing a change in the electronic structure of iron ions upon this phase transition. According to the calibration of hfs parameters *IS* and *QS* [7, 8], their values in the HP phase correspond to the low-spin (LS) state of Fe^{3+} ions ($S = 1/2$; $^2T_{2g}$). This suggests that the magnetic collapse is caused by the

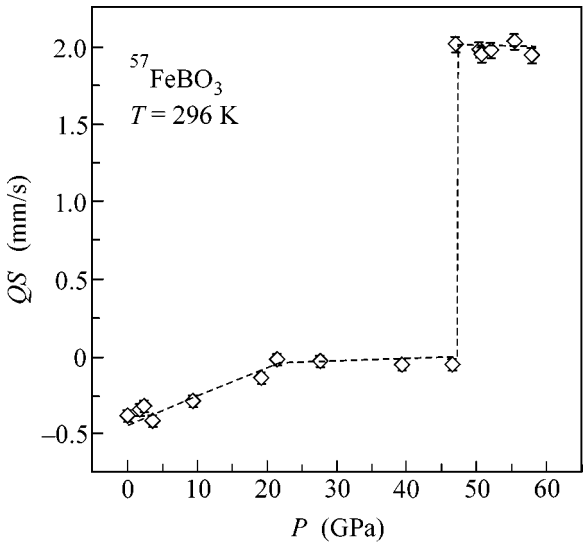

Fig. 3. Pressure dependence of the quadrupole splitting *QS* in the spectra of $^{57}FeBO_3$. Dashed line is a guide to the eye.

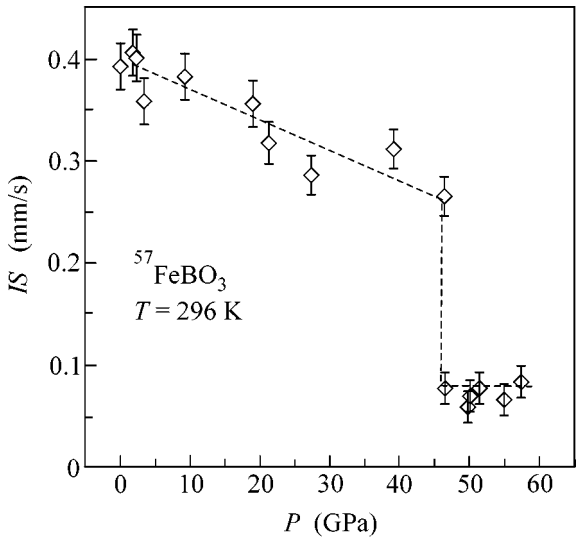

Fig. 4. Pressure dependence of the isomer shift *IS* relative to metallic iron in the Mössbauer spectra of $^{57}FeBO_3$.

rupture of strong *d*–*d*-electron correlations (Mott's transition) and not by the temperature effect of the Néel-point type. The jumplike change in the parameters H_{hf}, *QS*, and *IS* indicates that this phase transition is of the first order.

The polycrystal measurements showed that the field H_{hf} in the polycrystalline LP phase behaves in the same manner as in the single crystal. The magnetic collapse is observed at $P = 48 \pm 2$ GPa, which coincides, to within experimental error, with the single-crystal critical pressure. However, after the transition to the nonmagnetic HP phase, the polycrystalline Mössbauer spectrum transforms into two quadrupole doublets (Fig. 5) with an intensity ratio of ~2 : 1. The parameters *QS* and *IS* of the more intense doublet coincide with their values in the single-crystal HP phase. This indicates that the major portion of the iron ions undergo transition to the low-spin state after the magnetic collapse. The parameters $QS \sim 1.5$ mm/s and $IS \sim 0.4$ mm/s of the less intense doublet are typical of the Fe^{3+} HS state. This suggests that a quantity of iron ions in the polycrystal remain in the HS (although nonmagnetic at room temperature) state at pressures higher than the magnetic transition pressure. This may be caused by the nanodimensional effects in small-sized polycrystal particles and, thus, requires additional studies. Note that no additional anomalies were observed in the Mössbauer spectra of both single-crystal and polycrystalline samples at pressures 51–54 GPa, where the structural phase transition was observed in [6].

DISCUSSION

4.1. Pressure Dependence of the Néel Temperature

The fact that the magnetic field H_{hf} in the LP phase increases with pressure (Fig. 2) is, naturally, due to strengthening of the exchange interaction, and hence it should correlate with the increase in the Néel temperature T_N. Generally, the pressure dependence of H_{hf} at $T = 296$ K is caused both by the pressure dependence of T_N and a possible change in the field H_{hf} with pressure at $T = 0$ K. Our low-temperature NFS measurements showed [9] that the field $H_{hf}(0)$ in the LP phase depends weakly on the pressure and is close to 55.5 T. Using the room-temperature pressure dependence $H_{hf} = f(P)$ and the normal-pressure temperature data $H_{hf} = f(T)$ from [10], one can derive the pressure dependence for the Néel temperature $T_N = f(P)$. To this end, we applied the extrapolation procedure that was suggested earlier in [11, 12] and recommended itself well in the analysis of experimental data. Let us write the pressure and temperature dependence of H_{hf} in the empirical form

$$H_{hf}(P, T) = H_{hf}(P, 0) \times \exp\left(-\alpha\frac{T}{T_N(P)}\right)\left[1 - \frac{T}{T_N(P)}\right]^{\beta}. \quad (1)$$

The parameters α and β were calculated by fitting function (1) to the normal-pressure experimental $H_{hf}(T)$ dependence to obtain $\alpha = -0.371$ and $\beta = 0.4308$. The results of this calculation are shown in the inset in Fig. 6. Next, assuming that α and β are constant and $H_{hf}(P, 0) = 55.5$ T = const, the equation for the variable T_N

$$F(T_N) = \Phi(T_N)$$

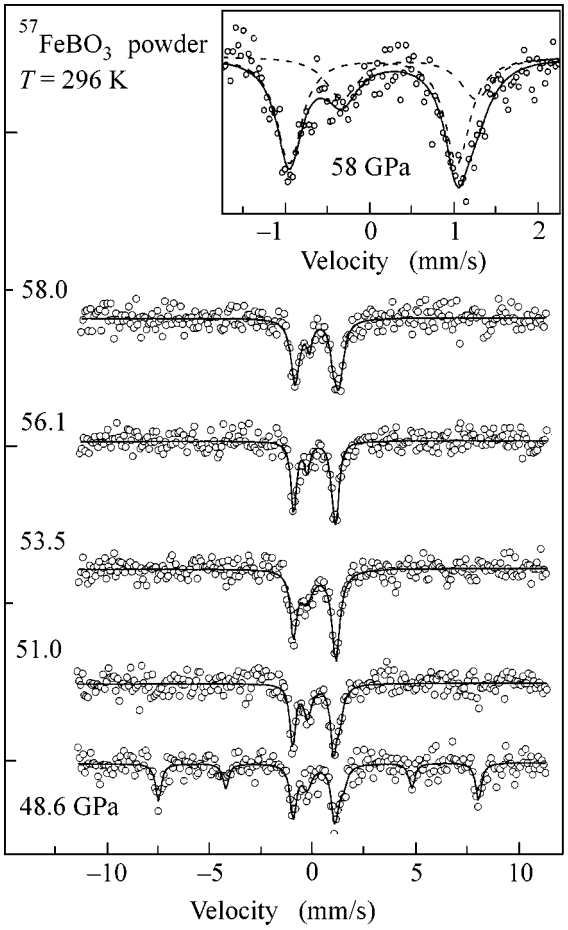

Fig. 5. Room-temperature Mössbauer spectra of a $^{57}FeBO_3$ polycrystal for some pressures below and above the phase transition. Solid lines correspond to calculations. The velocity-expanded spectrum at P = 58.0 GPa is shown at the top.

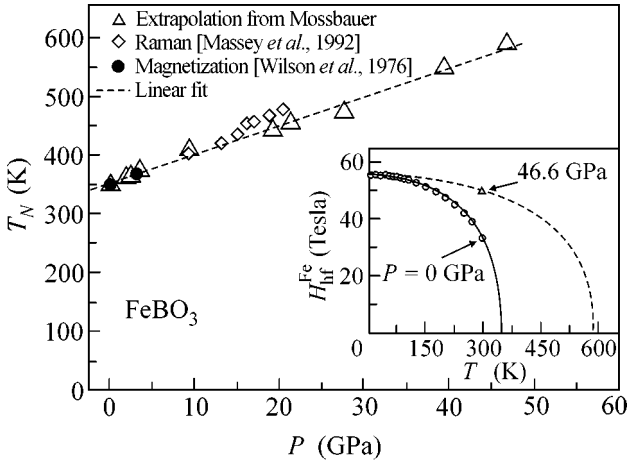

Fig. 6. Pressure dependence of the Néel temperature T_N of $FeBO_3$, as calculated from our experimental data (triangles) using empirical model (see text). The magnetization data taken from [13] (circles) and the two-magnon Raman data from [14] (rhombi) are shown for comparison. The dashed line is a linear fit to the calculated points. Inset: (solid line) a fit of the empirical model to the experimental $H_{hf}(T)$ curve at P = 0 (points are from [10]) and (dashed line) the calculation for P = 46.6 GPa (triangle is our data).

was graphically solved for each value of experimental pressure and, respectively, for $H_{hf}(P, T = 295\ \text{K})$, where

$$F(T_N) = H_{hf}(P, T)\exp\left(\alpha\frac{T}{T_N}\right),$$
$$\Phi(T_N) = H_{hf}(P, 0)\left[1 - \frac{T}{T_N}\right]^{\beta}. \quad (2)$$

The resulting T_N values are presented in Fig. 6 together with the data of magnetization measurements [13] and two-magnon Raman spectra [14]. It is clearly seen that our data agree well with these experiments. To a good accuracy, the obtained pressure dependence of T_N is linear with parameters $T_N(0) = 351.2 \pm 3.5$ K and $dT_N/dP = +4.91 \pm 0.15$ K/GPa. The logarithmic derivative of the Néel temperature was found to be $\partial\ln(T_N)/\partial P = 0.0141\ \text{GPa}^{-1}$.

P.W. Anderson [15] showed that T_N in antiferromagnetic oxides with superexchange is proportional to the exchange integral J. Using the $V(P)$ dependence obtained in our work [6] and the $T_N(P)$ dependence, one can verify for $FeBO_3$ the empirical Bloch relation $J \propto V^{\varepsilon}$ with $\varepsilon = -10/3$, which was suggested in [16] for transition metal oxides. With this aim, we constructed the curve for the logarithm of T_N (reduced to its zero-pressure value) as a function of the logarithm of the reduced volume V. Linear fit of this dependence with $J \propto T_N \propto V^{\varepsilon}$ gave $\varepsilon = (\partial\ln J/\partial\ln V) = (\partial\ln(T_N)/\partial\ln V) = -3.70 \pm 0.14$. This value is slightly larger than the Bloch value (–10/3), but, nevertheless, it agrees well with the Bloch model.

4.2. Quadrupole Splitting QS = f(P)

In the general case, the electric-field gradient Δ in the vicinity of the ^{57}Fe nucleus is the sum of two main contributions: the lattice contribution Δ_{lat} from the crystal field produced by the surrounding ions and the electronic contribution Δ_{el} from the nonspherical charge distribution of its own electron shell. The electron shell of Fe^{3+} ions in the high-spin $3d^5$ state (S = 5/2) is spherically symmetric (their ground state is the orbital singlet $^6A_{1g}$), so that the measured QS is caused only by the lattice contribution Δ_{lat}. One can see in Fig. 3 that QS in the LP phase is small and weakly increases with pressure. This is consistent with the nearly cubic surrounding of iron ions by oxygen. Recently, we have established [6] that the transition to the HP phase in iron borate is accompanied by a jump (decrease) in unit-cell volume by almost 9%, although the type of crystal structure is retained and the space group remains

unchanged ($R\bar{3}c$). Because of this, one should not expect any sizable increase in the Δ_{lat} contribution. Consequently, the experimentally observed sharp increase in *QS* in the HP phase is due to the electronic contribution that appears due to the transition of Fe^{3+} to the low-spin state.

4.3. Isomer Shift IS = f(P)

It is seen in Fig. 4 that the isomer shift in the LP phase is typical of the Fe^{3+} HS state in oxides. Upon the pressure buildup, *IS* decreases gradually, indicating that the *s*-electron charge density at the nucleus increases due to the decrease in atomic volume. After the transition to the HP phase, the value of *IS* drops sharply, indicating the metallization process. This is consistent with the appearance of the LS state, because the atomic volume of iron ions in the LS state is smaller than in the HS state. This also correlates with filling of the conduction band as a result of electron delocalization and with the effective decrease in the cation radii.

Therefore, the behavior of the three parameters H_{hf}, *QS*, and *IS* gives evidence for the phase-transition-induced spin crossover HS $\longrightarrow$ LS.

The 3*d*-metal oxides are mostly Mott's wide-gap insulators with strong electron correlations providing a high-spin state for the 3*d* ions. The correlation energy of localized *d* electrons is characterized by the Hubbard parameter *U* (Coulomb repulsion) [17, 18], and the degree of localization is determined by the ratio *U*/*W*, where *W* is the bandgap. Under high pressure, the strong-correlation regime ($U/W \gg 1$) can be violated, because *W* increases with pressure, while *U* decreases because of an increase in screening, so that a Mott's insulator becomes a metal in which the localized magnetic moment collapses [19]. Monte-Carlo calculations [20] predict metallic behavior at $U/W < \sqrt{N}$, where *N* is the orbital degeneracy ($N = 5$ for iron ions), and the critical value $U/W = 2.24$ for the metallization and magnetic collapse [19].

The magnetic HS $\longrightarrow$ LS transition with a change of the spin state may occur either due to the widening of the *d* band or to a change in the crystal field [21]. If the splitting of the t_{2g} and e_g states in the crystal field is larger than the exchange splitting, the magnetic collapse is due to a change in the populations of these states. To describe the pressure behavior of magnetic oxides, Cohen *et al.* [19] developed the theory of generalized gradient approximation on the basis of the Stoner model [22] of stability criterion for a magnetic state. They showed that the magnetic collapse occurs with an increase in pressure (i.e., a decrease in the distances between nearest neighbors) because of the *d*-band widening, whereas small variations of crystal field play the secondary part and only influence the character of transition. The band widens due to an increase of the hybridization as a result of a decrease in the interion distances with the buildup of pressure and a change in the character of chemical bonding from ionic to metallic.

Our experimental data qualitatively confirm these considerations. This allows the conclusion to be drawn that the $FeBO_3$ crystal undergoes Mott's transition at a pressure of 46 ± 2 GPa with the rupture of *d*–*d*-electron correlations and the magnetic-moment collapse.

An analogous effect was recently observed in rare-earth orthoferrites $LaFeO_3$ and $PrFeO_3$ [23, 24] and hematite Fe_2O_3 [25], where the rupture of electron correlations at high pressure manifested itself in the magnetic collapse and the insulator–metal transition, which, however, was extended over a wide pressure range.

The ground state of the low-spin $3d^5$-electron configuration in Fe^{3+} can be represented as $(t_{2g}\uparrow)^3(t_{2g}\downarrow)^2$ with a magnetic moment approximately five times smaller than in the HS state. This allows a low-temperature paramagnetism, which we plan to observe by continuing NFS experiments at low temperatures.

Theoretical density-functional calculations for iron borate were recently carried out by Parlinskiĭ [26] to predict the magnetic and structural phase transitions and the metallization with gap collapse in the electronic spectrum at pressures 20–60 GPa with large hysteresis. According to [26], the magnetic moment of iron ions in the HP phase is small (approximately four times smaller than in the LP phase). Our experimental results confirm, for the most part, the conclusions of that work.

CONCLUSION

At room temperature, the magnetic moment of iron borate collapses with the spin crossover HS $\longrightarrow$ LS at a pressure of 46–48 GPa. This correlates with the abrupt decrease in the unit-cell volume and a sharp decrease in the optical gap. The change in the magnetic and electronic structures is explained by Mott's transition and the rupture of strong *d*–*d*-electron correlations and results in a drastic change of the transport properties. The pressure dependence of the Néel point is obtained and the Bloch parameter ε is estimated for the low-pressure phase ($P < 46$ GPa).

We are grateful to Dr. R. Rüffer, O. Leupold, A. Chumakov, and N.S. Ovanesyan for helpful discussion of results. This work was supported by the Russian Foundation for Basic Research (project nos. 02-02-17364a, 00-02-17710a, 01-02-17543a) and NATO (grant no. PST.CLG.976560).

REFERENCES

1. I. Bernal, C. W. Struck, and J. G. White, Acta Crystallogr. **16**, 849 (1963).
2. R. Wolff, A. J. Kurtzig, and R. C. LeCraw, J. Appl. Phys. **41**, 1218 (1970).

3. R. Diehl, Solid State Commun. **17**, 743 (1975).
4. I. S. Edelman, A. V. Malakhovskii, T. I. Vasileva, and V. N. Seleznev, Fiz. Tverd. Tela **14**, 2810 (1972) [Sov. Phys. Solid State **14**, 2442 (1973)].
5. I. A. Troyan, A. G. Gavrilyuk, V. A. Sarkisyan, *et al.*, Pis'ma Zh. Éksp. Teor. Fiz. **74**, 26 (2001) [JETP Lett. **74**, 24 (2001)].
6. A. G. Gavriliuk, I. A. Trojan, R. Boehler, *et al.*, Pis'ma Zh. Éksp. Teor. Fiz. **75**, 25 (2002) [JETP Lett. **75**, 23 (2002)].
7. F. Menil, J. Phys. Chem. Solids **46**, 763 (1985).
8. M. E. Lines and M. Eibschutz, Physica C (Amsterdam) **166**, 235 (1990).
9. V. A. Sarkisyan, I. S. Lyubutin, A. G. Gavriliuk, and R. Rüffer, in *Abstracts of Fifth Seeheim Workshop on Mossbauer Spectroscopy* (Seeheim, Germany, 2002), p. C-05.
10. M. Eibschutz and M. E. Lines, Phys. Rev. B **7**, 4907 (1973).
11. A. G. Gavriliuk, G. N. Stepanov, V. A. Sidorov, and S. M. Irkaev, J. Appl. Phys. **79**, 2609 (1996).
12. A. G. Gavriliuk, G. N. Stepanov, I. S. Lyubutin, *et al.*, Zh. Éksp. Teor. Fiz. **117**, 375 (2000) [JETP **90**, 330 (2000)].
13. D. M. Wilson and S. Broersma, Phys. Rev. B **14**, 1977 (1976).
14. M. J. Massey, R. Merlin, and S. M. Girvin, Phys. Rev. Lett. **69**, 2299 (1992).
15. P. W. Anderson, Phys. Rev. **115**, 2 (1959); Solid State Phys. **14**, 99 (1963).
16. D. Bloch, J. Phys. Chem. Solids **27**, 881 (1966).
17. J. Habbard, Proc. R. Soc. London, Ser. A **277**, 237 (1964).
18. J. G. Zaanen, G. A. Sawatzky, and J. W. Allen, Phys. Rev. Lett. **55**, 418 (1985).
19. R. E. Cohen, I. I. Mazin, and D. G. Isaak, Science **275**, 654 (1997).
20. O. Gunnarsson, E. Koch, and R. M. Martin, Phys. Rev. B **54**, R11026 (1996).
21. S. Ohnishi, Phys. Earth Planet. Inter. **17**, 130 (1978).
22. E. C. Stoner, Proc. R. Soc. London, Ser. A **169**, 339 (1939); G. L. Krasko, Phys. Rev. B **36**, 8565 (1987).
23. G. R. Hearne, M. P. Pasternak, R. D. Taylor, and P. Lacorre, Phys. Rev. B **51**, 11495 (1995).
24. W. M. Xu, O. Naaman, G. Kh. Rozenberg, *et al.*, Phys. Rev. B **64**, 094411 (2001).
25. M. P. Pasternak, G. Kh. Rozenberg, G. Yu. Machavariani, *et al.*, Phys. Rev. Lett. **82**, 4663 (1999).
26. K. Parlinski, Eur. Phys. J. B **27**, 283 (2002).

Translated by V. Sakun

JETP Letters, Vol. 76, No. 11, 2002, pp. 670–674. Translated from Pis'ma v Zhurnal Éksperimental'noĭ i Teoreticheskoĭ Fiziki, Vol. 76, No. 11, 2002, pp. 794–798.

Observation of Subgap Resistive Oscillations in Doubly Connected *SNS* Systems with the Suppressed Proximity Effect

Yu. N. Chiang* and O. G. Shevchenko

Verkin Institute of Low Temperatures, Kharkov Physics and Technology Institute, National Academy of Sciences of Ukraine, Kharkov, 61103 Ukraine

** e-mail: chiang@ilt.kharkov.ua*

Received June 21, 2002; in final form, October 31, 2002

Phase-sensitive magnetoresistive oscillations were observed at temperatures $T < 4$ K in hybrid quasi ballistic doubly connected *SNS* structures with single-crystal normal spacers of macroscopic sizes in all dimensions (L = 100–500 μm) and elastic electron mean free path on the same scale $l_{el} \sim 100$ μm. The oscillations observed for the distances corresponding to the indicated L values between the *NS* interfaces are evidence that the phase-interruption length in pure metal is macroscopic at $T < 4$ K. The oscillation parameters related to the geometry of structures and spacer sizes indicate the quantum nature of the oscillations. These are shown to reflect the behavior of conductance in the *NS* interfaces with the dissipative coherent transport of "subgap" quasiparticles with energies $\varepsilon \ll \Delta$, T (Δ is the gap energy). © *2002 MAIK "Nauka/Interperiodica".*

PACS numbers: 74.80.Fp; 73.40.-c; 74.50.+r

It is well known that phase-sensitive current (and, therefore, conductance) in *SNS* systems with dirty normal spacers of a sizable thickness may not exhibit an exponential dependence $j \sim F(\phi)\exp(-L/\xi_T)$ on the spacer thickness L, although it may be rather strong and retain the dependence on the coherent phase difference ϕ between superconductors under conditions $L > \xi_T$. Such behavior of current is due to the long-range phase coherence for the zero-order effects in the parameter $\lambda_B/l_{el} \ll 1$ (ξ_T is the normal-metal coherence length, $F(\phi)$ is a periodic function, and λ_B and l_{el} are, respectively, the de Broglie wavelength and the electron elastic mean free path). This feature, in fact, was pointed out in early theoretical works [1, 2], where not exponential (but, particularly, logarithmic [1]) behavior with respect to the parameter L/ξ_T was predicted for the phase-coherent current in the *SNS* systems with metallic spacers in which l_{el} are much smaller than the superconducting correlation parameter $\xi_0 \sim 1$ μm. The latter determines, by the order of magnitude, the spatial scale of the proximity effect for coherent pairs with $\varepsilon \sim T$ in a pure normal metal contacting a type-I superconductor [3]. This l_{el}/ξ_0 ratio is typical of normal spacers in the majority of nanotechnologically prepared *SNS* systems which exhibit a nonexponential behavior of the amplitudes of phase-sensitive oscillations in the regime $(L/\xi_T) > 1$ and, thus, suggest possible long-range phase coherence under Andreev reflection conditions [4–6]. However, the values of L and the phase-interruption length in the samples with such "diffusional" characteristics, i.e., the samples for which the phase-coherent behavior of conductance in the *SNS* geometry was studied, are ordinarily limited to 1 μm, while the condition $d/\xi_T > 1$ is not fulfilled in such samples for one of the dimensions parallel to the interface ($d \approx 0.02$–0.05 μm). In this connection, it was profitable to investigate this effect on a larger spatial scale of parameters that are responsible for it. The achievements in the theory of long-range phase coherence [7–9] have also stimulated the performing of a new experiment.

In this work, the quantum-interference behavior of the conductivity of doubly connected *SNS* structures was observed and examined under conditions radically different from those studied previously ($L \sim \xi_T^{bal}$; $l_{el} < \xi_T = \sqrt{(1/3)l_{el}\xi_T^{bal}} \ll \xi_T^{bal}$), namely, for L, $l_{el} \gg \xi_T = \xi_T^{bal}$ and $L/\xi_T \approx 10^2$, i.e., for sizes L of normal spacers far exceeding all previously studied characteristic microscopic lengths in metal and fully excluding the proximity effect for the major portion of carriers with energy $\varepsilon \sim T$.

Hybrid samples $\Im 1$ (In–Cu–Sn), $\Im 2$ (Sn–Cu–Sn), and $\Im 3$ (Pb–Cu–Pb) were prepared using a doubly connected *SNS* Andreev interferometer with a calibrated opening. Figure 1 shows schematically (not to scale) the construction of one of the samples typical of the other samples, together with a wire turn as a source of an external magnetic field $\mathbf{H}_e$ for controlling the macroscopic phase difference in the interferometer formed by a piece of copper single crystal and a superconductor

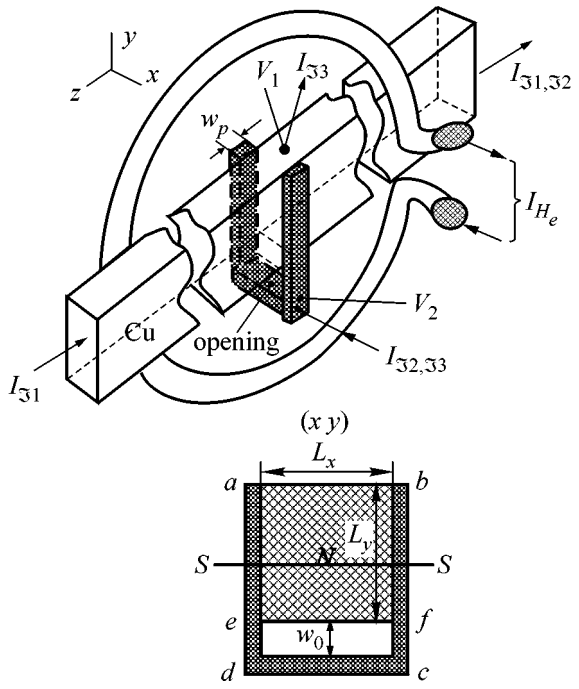

Fig. 1. Typical construction (not to scale) of the studied quasiballistic doubly connected interferometers. V_1 and V_2 are the potential probes; I_i are the current-entry points ($i = \Im 1$, $\Im 2$, $\Im 3$); I_{H_e} is the circular-turn current producing magnetic field $\mathbf{H}_e$. Inset: interferometer cross sections in the *xy* plane.

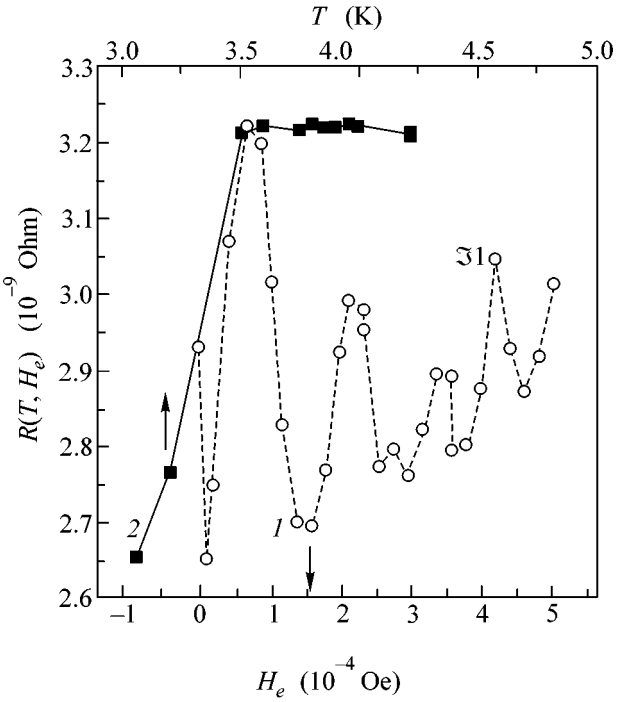

Fig. 2. Curve *1*: oscillations of the generalized resistance $R = U/I$ of interferometer $\Im 1$ (In–Cu–Sn) as functions of magnetic field at $T = 3.25$ K. The oscillation period is $\Delta_H = (h/2e)/S_{\max}$, where $S_{\max}$ is the area of the *abcd* contour in the *xy* cross section of the interferometer (see inset in Fig. 1). Curve 2: temperature dependence $R(T)$ at $H_e = 0$.

connected to it. Interferometers varied in size, type of superconductor, and area of the *NS* interfaces.

The samples were fabricated as follows. Either the strips of superconducting metals of width w_p (samples $\Im 1$ and $\Im 3$) or a copper wire with diameter w_p coated with a thin superconducting layer (sample $\Im 2$) were fused to two opposite faces of width L_y of a bar with rectangular cross section made from copper single crystal, with a clearance between the superconductors and a bar face of width L_x (Fig. 1). The clearance sizes were $L_x \times w_p \times w_0$, where w_0 is the calibrated insulation thickness in the clearance. A part of copper bar with size $L_x \times L_y \times w_p$ functioned as a normal interferometer segment with the *NS* interfaces arranged at opposite bar faces and separated by the distance L_x. The cross-sectional sizes of normal segments $L_x \times L_y$ were 0.35×0.35 mm for $\Im 1$, 0.25×0.5 mm for $\Im 2$, and 0.125×0.475 mm for $\Im 3$.

The samples were placed at the center of a circular turn with a radius of 1 cm and oriented by the long bar axis *z* along the turn axis. The nonorthogonality of the turn axis and the interferometer *xy* planes was 5°–10°. The field H_e was varied within several oersteds with a relative step of 10^{-5} Oe and an error of field measurement no higher than 10%. To compensate external fields, including the Earth's field, a container with the sample and the turn was placed into a closed superconducting screen (not shown in Fig. 1).

The ratio of resistances at room and helium temperatures for metals used in the fabrication of hybrid structures was $RRR \geq 10^4$ with $l_{\text{el}} \approx 100$ μm at helium temperatures. The measurement temperatures for sample $\Im 1$ were in the range of temperatures corresponding to the indium intermediate state and below, and, for samples $\Im 2$ and $\Im 3$, below the analogous range for tin and lead. Temperature was measured with an accuracy of about 10^{-4}, and working current I (~1 A) was measured with an accuracy of 10^{-5}.

The potential difference U was measured to within $(0.5–1) \times 10^{-12}$ V. Measurements were performed using four-, three-, and two-probe schemes for the interferometers $\Im 1$, $\Im 2$, and $\Im 3$, respectively (Fig. 1). One of the potential probes, V_1, was welded to the normal part of the *SNS* system, and another probe V_2 was soldered to the region of superconducting In, Sn, or Pb. The barrier resistance in the V_1 probe contact with copper was approximately an order of magnitude larger than the resistances of normal segments $R_N \approx 10^{-9}$ Ω.

Figures 2, 3, and 4, relating to systems $\Im 1$, $\Im 2$, and $\Im 3$, respectively, show the typical results of measuring

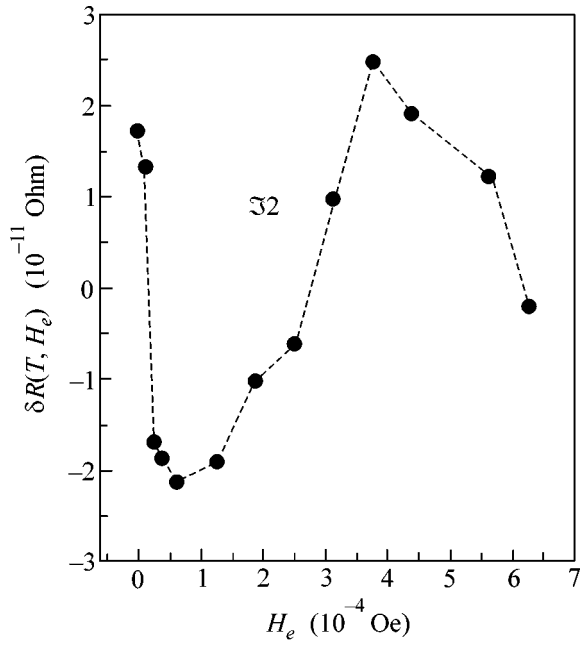

Fig. 3. Oscillations of Andreev resistance $\delta R_A = U/I - R_{H_e = 0}$ in interferometer ℑ2 (Sn–Cu–Sn) as functions of magnetic field at $T = 3.49$ K. The oscillation period is $\Delta_H = (h/2e)/S_{\min}$, where $S_{\min}$ is the area of the *cdef* contour in the *xy* cross section of the interferometer (see inset in Fig. 1); $R_{H_e = 0} = 8.8104 \times 10^{-8}\ \Omega$.

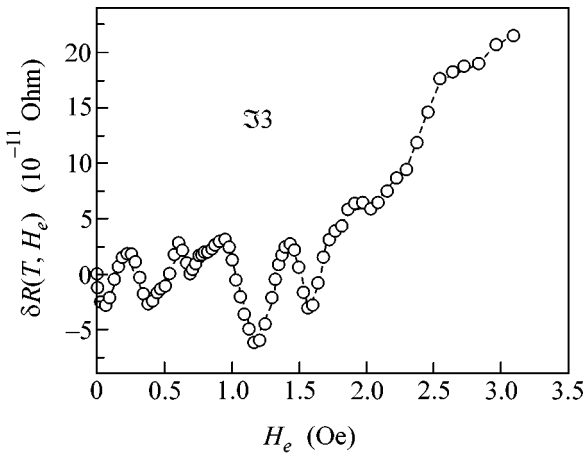

Fig. 4. Oscillations of Andreev resistance $\delta R_A = U/I - R_{H_e = 0}$ in interferometer ℑ3 (Sn–Cu–Sn) as functions of magnetic field at $T = 4.125$ K. The oscillation period is $\Delta_H = (h/2e)/S^*_{\min}$, where $S^*_{\min}$ is the area of *xy* projection of the stretched opening of interferometer onto the direction of magnetic field upon the deviation from the *z* axis; $R_{H_e = 0} = 2.6245 \times 10^{-8}\ \Omega$.

the potential difference U with the V_1–V_2 pair of probes. The potential difference was measured as a function of magnetic field $\mathbf{H}_e$ and normalized to a constant measuring current I. The quantity $R = U/I$ has the meaning of generalized resistance of the systems. One can see in the figures that R has an oscillatory character in all cases.

The inset in Fig. 1 shows the interferometer cross section by a plane normal to $\mathbf{H}_e$. The *cdef* contour enclosing the interferometer opening and including the trace of the lower face of the normal region corresponds to the *xy* projection of the minimal area $S_{\min}$, while the *abcd* contour including the trace of the upper face corresponds to the *xy* projection of the maximal area $S_{\max}$ of all *xy* projections of the possible closed *SNS* contours of the system. It turned out that these projections of extreme areas S_{extr} onto the plane normal to the vector of external magnetic field were related to the periods Δ_H of observed oscillations by the expression

$$S_{\text{extr}}\Delta_H = \Phi_0, \qquad (1)$$

where Φ_0 is the magnetic flux quantum $h/2e$.

The experimental values of Δ_H and the values of Φ_0/S_{extr} calculated using the values of S_{extr} corresponding to the geometric parameters of the samples are given in the table. Since even a small misalignment between the magnetic field and the *z* axis substantially changes the magnetic flux for the opening stretched along *z* ($w_p/w_o \gg 1$), because of the screening of opening by superconductor, the value $S^*_{\min} = S_{\min}[1 - (w_p/w_o)\sin\alpha]^2\cos\alpha$ estimated for a misalignment $\alpha = 0.15$ was taken as the smallest area of *xy* projection for interferometer ℑ3. The table also gives the temperatures of measurements.

The following features differentiate our interferometers from the previously studied systems. The opening cross section is smaller than the cross section of normal region; the macroscopic sizes of normal region are, nevertheless, comparable with the elastic mean free path; and the transmissivity of the *NS* interfaces is close to unity. Due to the first factor, the values of $S_{\min}$ and $S_{\max}$ differed from each other by more than an order of magnitude for each of the interferometers (some of them are given in the table), allowing the corresponding oscillation periods to be resolved. The two other factors greatly simplify the analysis of phase-sensitive coherent conduction in our interferometers as quasiballistic *SNS* structures.

The sensitivity of dissipative conduction to the macroscopic phase difference in a closed *SNS* contour is direct evidence of the coherent transport in the system and the role of both *NS* interfaces in it. In turn, the coherent transport at $L \gg \xi_T$ can be caused by only those normal-metal excitations whose energies $\varepsilon \ll T < \Delta$ fill the Andreev spectrum that arises due to the restrictions on the quasiparticle motion because of the Andreev

Table

Sample	w_p/w_o	T (K)	Δ_H (Oe)	Φ_0/S_{extr} (Oe)	S_{extr} (cm^2)
ℑ1	≈0.5	3.25	1.5×10^{-4}	1.48×10^{-4}	1.4×10^{-3} (max)
ℑ1	"	3.0	1.17×10^{-3}	1.22×10^{-3}	1.7×10^{-4} (min)
ℑ2	≪1	3.49	5×10^{-4}	5.17×10^{-4}	4×10^{-4} (min)
ℑ3	≈7	4.125	0.3–0.5	0.41	$\approx5\times10^{-7}$ (min)

reflections [7, 9]. It follows from the quasi-classical dimensional quantization [10, 11] that the spacing between the levels of the Andreev spectrum should be $\varepsilon_A \approx \hbar v_F/L_x \approx 20$ mK for the distance between interfaces $L_x \simeq 0.5$ mm. This corresponds to the upper limit for energies of *e–h* excitations on the dissipative (passing through the elastic scattering centers) coherent trajectories in the normal region. To zero order in the parameter λ_B/l, only these trajectories can make a nonaveraged phase-interference contribution to conductance, often called the Andreev conductance G_A [12]. Accordingly, it was hoped that the modulation depth for the normal conductance G_N (or resistance R_N) in our interferometers in the temperature range measured would be

$$-\frac{G_A}{G_N} \equiv \frac{\delta R_A}{R_N} \approx \frac{\varepsilon_A}{T} \simeq 10^{-2} \qquad (2)$$

and an order of magnitude higher than the measurement accuracy at $R_N \simeq 10^{-9}$ Ω, and this is confirmed by the data in the table. It is known that, in the approximation of noninteracting trajectories, the macroscopic phase ϕ_i for a superconductor-closed *i*th trajectory of coherent excitations with phases ϕ_{ei} and ϕ_{hi} depends in an external vector-potential field A on the magnetic flux as

$$\phi_i = \phi_{ei} + \phi_{hi} = \phi_{0i} + 2\pi\frac{\Phi_i}{\Phi_0}, \qquad (3)$$

where ϕ_{0i} is the microscopic phase related to the length of a trajectory between the interfaces by the Andreev reflection phase shifts; $\Phi_i = \mathbf{H}_e \cdot \mathbf{S}_i$ is the magnetic flux through the projection S_i onto the plane perpendicular to $\mathbf{H}_e$; $\mathbf{H}_e = \nabla \times \mathbf{A}$ is the magnetic-field strength vector; $\mathbf{S}_i = \mathbf{n}_{S_i} \cdot S_i$; $\mathbf{n}_{S_i}$ is the normal unit vector; S_i is the area under the trajectory; and Φ_0 is the flux quantum $h/2e$.

The evaluation of the overall interference correction $2\text{Re}(f_e f_h^*)$ in the expression for the total transmission probability $|f_e + f_h|^2$ ($f_{e,h}$ are the scattering amplitudes) along all coherent trajectories can be reduced to the evaluation of the Fresnel-type integral with respect to the parameter $\mathbf{S}_i$ [13, 14]. This results in the separation of the **S**-nonaveraged phase contributions at the integration limits (see, e.g., [15]). As a result, the oscillating portion of the interference addition to the total resistance of the normal region in the *SNS* interferometer, in particular, for $\mathbf{H}_e \parallel \mathbf{z}$, takes the form

$$\sigma R_A \sim \frac{\varepsilon_A}{T}\sin 2\pi\left(\phi_0 + \frac{H_e S_{\text{extr}}}{\Phi_0}\right), \qquad (4)$$

where S_{extr} is the minimal or maximal area of the projection of doubly connected *SNS* contours of the system onto the plane perpendicular to **H**, and $\phi_0 \sim (1/\pi)(L/l_{\text{el}}) \sim 1$ [16]. Our experimental data are in good agreement with this phase dependence of the generalized interferometer resistance and the magnitude of the effect. Since all doubly connected *SNS* contours include *e–h* coherent trajectories in the normal region with a length of no less than $\sim L \approx 10^2\xi_T$, one can assert that the observed oscillations are due to the long-range quantum coherence of quasiparticle excitations with energy $\varepsilon \ll T$ under conditions of suppressed proximity effect for the major portion of electrons with energies $\varepsilon \sim T$ [9].

The main results of this work are as follows. Magnetoresistive oscillations with a constant period in a magnetic field have been observed in doubly connected *SNS* interferometers under conditions of strong inequality $L \gg \xi_T$ ($L/\xi_T \approx 10^2$). These conditions were obtained due to the use of single crystals of a pure metal with the macroscopic elastic bulk mean free path as normal interferometer segments of size comparable to this path ($L_x \approx l_{\text{el}} \approx 10^2$ μm). The oscillations are periodic in the flux quantum $h/2e$ inside closed *SNS* contours with extreme flux values. The contours contain macroscopically long sections of coherent *e–h* trajectories in a quasiballistic normal segment and pass through the large-area *NS* contacts with transmissivity close to 1. Such a character of oscillations and the conditions for their observation are caused by a solid-state analogue of the Aharonov–Bohm effect in Andreev reflections of low-energy quasiparticles with the suppressed proximity effect for the major portion of electrons with energy $\varepsilon \sim T$.

REFERENCES

1. L. G. Aslamazov, A. I. Larkin, and Yu. N. Ovchinnikov, Zh. Éksp. Teor. Fiz. **55**, 323 (1968) [Sov. Phys. JETP **28**, 171 (1969)].
2. A. I. Svidzinskiĭ, *Spatially-Inhomogeneous Problems of the Theory of Superconductivity* (Nauka, Moscow, 1982).

3. P. G. de Gennes, *Superconductivity of Metals and Alloys* (Benjamin, New York, 1966; Mir, Moscow, 1968).
4. P. G. N. de Vegvar, T. A. Fulton, W. H. Mallison, and R. E. Miller, Phys. Rev. Lett. **73**, 1416 (1994).
5. H. Courtois, Ph. Gandit, D. Mailly, and B. Pannetier, Phys. Rev. Lett. **76**, 130 (1996).
6. A. Kadigrobov, L. Y. Gorelik, R. I. Shekhter, *et al.*, Phys. Rev. B **60**, 14589 (1999).
7. F. Zhou, B. Spivak, and A. Zyuzin, Phys. Rev. B **52**, 4467 (1995).
8. Yu. V. Nazarov and T. H. Stoof, Phys. Rev. Lett. **76**, 823 (1996).
9. F. Zhou and B. Spivak, Pis'ma Zh. Éksp. Teor. Fiz. **65**, 347 (1997) [JETP Lett. **65**, 369 (1997)].
10. A. F. Andreev, Zh. Éksp. Teor. Fiz. **46**, 1823 (1964) [Sov. Phys. JETP **19**, 1228 (1964)]; Zh. Éksp. Teor. Fiz. **49**, 655 (1965) [Sov. Phys. JETP **22**, 455 (1966)].
11. I. O. Kulik, Zh. Éksp. Teor. Fiz. **57**, 1745 (1969) [Sov. Phys. JETP **30**, 944 (1970)].
12. C. J. Lambert and R. Raimondi, J. Phys.: Condens. Matter **10**, 901 (1998).
13. Yu. N. Tszyan, Pis'ma Zh. Éksp. Teor. Fiz. **71** (8), 481 (2000) [JETP Lett. **71**, 334 (2000)].
14. Yu. N. Tszyan and O. G. Shevchenko, Fiz. Nizk. Temp. **27**, 1357 (2001) [Low Temp. Phys. **27**, 1000 (2001)].
15. J. M. Ziman, *Principles of the Theory of Solids*, 2nd ed. (Cambridge Univ. Press, London, 1972; Mir, Moscow, 1966).
16. B. J. van Wees, P. de Vries, P. Magnic, and T. M. Klapwijk, Phys. Rev. Lett. **69**, 510 (1992).

Translated by V. Sakun

JETP Letters, Vol. 76, No. 11, 2002, pp. 675–680. From Pis'ma v Zhurnal Éksperimental'noĭ i Teoreticheskoĭ Fiziki, Vol. 76, No. 11, 2002, pp. 799–804.

How Behavior of Systems with Sparse Spectrum Can Be Predicted on a Quantum Computer¶

Y. Ozhigov

Institute of Physics and Technology, Russian Academy of Sciences, Moscow, 117218 Russia

e-mail: ozhigov@ftian.oivta.ru

Received April 1, 2002; in final form, October 30, 2002

Call a spectrum of Hamiltonian H sparse if each eigenvalue can be quickly restored within ε from its rough approximation within ε_1 by means of some classical algorithm. It is shown how the behavior of a system with a sparse spectrum up to time $T = (1 - \rho)/14\varepsilon$ can be predicted on a quantum computer with the time complexity $t = 4/(1 - \rho)\varepsilon_1$ plus the time of classical algorithm, where ρ is the fidelity. The quantum knowledge of Hamiltonian eigenvalues is considered as the new Hamiltonian W_H whose action on each eigenvector of H gives the corresponding eigenvalue. Speedup of evolution for systems with a sparse spectrum is possible, because, for such systems, the Hamiltonian W_H can be quickly simulated on the quantum computer. For an arbitrary system (even in the classical case), its behavior cannot be predicted on a quantum computer even for one step ahead. By this method, we can also restore the history with the same efficiency. *© 2002 MAIK "Nauka/Interperiodica".*

PACS numbers: 03.67.Lx

1. INTRODUCTION AND BACKGROUND

A typical quantum system cannot be analyzed at hand or by a classical computer, because the dimension of its Hamiltonian is huge. Nevertheless, one can expect that this analysis would be easier in the framework of quantum computing. The idea of this approach is to force one quantum system to simulate the behavior of the other more simple primary system with some time saving. In the particular case where the primary system is the classical computer with oracle, this is the problem of quantum speedup for classical computations: given a classical algorithm with oracle, is there a quantum algorithm computing the same function faster using the same oracle quantum-mechanically? Examples: Shor factoring algorithm (see [1]), Grover search algorithm (see [2]).

The general form of the problem of prediction is as follows. Given a law of evolution for some system (classical or quantum), is there a device (wizard) of polynomial size that can predict the behavior of this system? To predict the behavior means that the wizard returns states of the initial system earlier than these states appear in the natural evolution. We note that, in the general case of quantum evolution, the wizard can use quantum-mechanically not only the Hamiltonian (as in the case of quantum computations with oracle) but some hidden information about the primary system. What kind of such information may be useful for the prediction? This is the information about the eigenvalues of the primary Hamiltonian. We analyze the possibility of quantum predictions in terms of the spectrum of the primary system.

The first general quantum method of finding eigenvalues was presented by Abrams and Lloyd in [3]. Their method uses quantum Fourier transform (QFT) and requires on the order of N implementations of the initial Hamiltonian, where N is the dimension of the main space. That method generalizes the Shor factoring algorithm. Thus, their algorithm requires an exponentially long time, and it cannot be used for quantum speedup. However, for the systems whose spectrum is sparse, the idea of this approach with QFT can be used for predictions. We proceed with the exact definitions.

2. DEFINITIONS

Let H be a Hamiltonian that induces the unitary transformations U in the N-dimensional space Y of states of n qubits by the usual quantum rule, $U(\tau) = \exp(-iH\tau/h)$, $N = 2^n$. In order to apply notions from the algorithm theory, such as complexity, etc., we assume that the time of Hamiltonian action is always $\tau = 1$. We can choose another value for τ, but this choice would only involve a change in time scale without any subsequences for the algorithm complexity. The system whose evolution is determined by the unitary transformation U is called the primary system.

We assume that the complexity of computation is the number of U applications. The time of all other transformations that we use here is assumed to be negligible compared with the time of computation. Quantum Fourier transform requires a time on the order of n^2

¶This article was submitted by the author in English.

(see [1]). Here, we will use this transform for $\log_2(M)$ qubits in the following form:

$$\mathrm{QFT}_M\colon |s\rangle \longrightarrow \frac{1}{\sqrt{M}}\sum_{l=0}^{M-1}\exp(-2\pi i s l/M)|l\rangle.$$

Let eigenvalues of H have the form $-2\pi\omega_k h$, $k = 0, 1, \ldots, N-1$, where the frequencies ω_k are real numbers from the segment [0, 1). Then the eigenvalues of U will be $\exp(2\pi i\omega_k)$. This is not a loss in generality, because we can always choose another unit τ for the Hamiltonian action time. Let us give the precise definitions of the "knowledge of eigenvalues" of H. It means that there exists another Hamiltonian W_H called a wizard for H that acts in the N^2-dimensional Hilbert space and returns an approximation of frequencies ω_k to within $1/N$, given the eigenvector Φ_k of H. How can frequencies be represented in a quantum memory? Every frequency ω_k has the binary notation $0.\epsilon_1\epsilon_2$. Let $p \le n$ be an integer, $M = 2^p$. We denote the string of ones and zeroes $\epsilon_1\epsilon_2 \ldots e_p$ by $\bar{\epsilon}_k^p$. ϵ_k^p may be considered as an integer if we cancel all first zeroes. And vice versa, every integer $l < M$ can be written in the form $\bar{\epsilon}_k^p$ if we add the corresponding string of zeroes in front. Then the number $\tilde{\omega}_k^M = 0.\bar{\epsilon}_k^p$ approximates w_k to within $1/M$. We define this number $0.\bar{\epsilon}_k^p \in [0, 1)$ by $(0.l)_p$. The simulation in this notation has the form

$$W_U|\Phi_k, b\rangle \longrightarrow |\Phi_k, b \oplus \bar{\epsilon}_k^p\rangle,$$

where $\oplus$ is the biwise addition modulo 2.

At last, we introduce auxiliary Walsh–Hadamard (WH) transformations and U_{seq}^p. Let the memory be divided into the main part x of n qubits and the ancilla a of $p \le n$ qubits: $|x, a\rangle$, $M = 2^p$. We set

(1) $\mathrm{WH}|x, a\rangle = \frac{1}{\sqrt{M}}\sum_{s=0}^{M-1}(-1)^{as}|x, s\rangle$. It is the WH transformation applied to the ancilla, where $\cdot$ denotes the dot product modulo 2.

(2) $U_{\mathrm{seq}}^p|x, a\rangle = |U^a x, a\rangle$. This is the result of a sequential applications of U to the main register.

The WH transform can be fulfilled in a standard model of quantum computer. To fulfill U_{seq}^p, it would suffice to use the following oracle U_{cond} (the conditional application of U) depending on U: $U_{\mathrm{cond}}|x, \alpha\rangle \longrightarrow |x', \alpha\rangle$, where $x' = x$ if $\alpha = 0$ and $x' = Ux$ if $\alpha = 1$; α is one qubit register. The application of U_{cond} cannot be reduced to the simple application of U as an oracle, because a conditional application of U is quantum-mechanically controlled by the second register. One proposal about its practical implementation can be found in Section 4.1.

3. SIMULATING TRANSFORMATION

3.1. How to Predict Evolution

Given a simulating (wizard) transformation, how can we predict the evolution of the primary system? Assume temporarily that the binary notation can represent our frequencies exactly. Let $|\xi\rangle$ denote the initial state of the main register. Let

$$\xi = \sum_{k=0}^{N-1} x_k|\Phi_k \qquad (1)$$

be an expansion of our state in the basis of eigenvectors of U. Add an n-qubit ancillary register initialized by zeroes and obtain the state $|\xi, 0^n\rangle$.

We then apply the transformation W_U to the main register ($p = n$). It gives the state

$$\xi' = \sum_{k=0}^{N-1} x_k|\Phi_k, \bar{\epsilon}_k^p\rangle.$$

Given a number t, we can turn each state in the first register by an angle determined by the second register and the value t, $2\pi\omega_k t$. This gives the state

$$\xi'' = \sum_{k=0}^{N-1} x_k\exp(2\pi i\omega_k t)|\Phi_k, \bar{\epsilon}_k^p\rangle.$$

We then apply the transformation W_U again to obtain

$$\xi''' = \sum_{k=0}^{N-1} x_k\exp(2\pi i\omega_k t)|\Phi_k, 0^n\rangle.$$

Now the cancellation of ancilla gives exactly the state $U^t|\xi\rangle$, which is the state at time t of the initial system. Therefore, given the transformation W_U, we can predict the behavior of the initial system, provided the action of this transformation takes a time smaller than $t/2$.

3.2. Approximate Simulation

In this subsection, we describe the procedure of simulating the predicting operator on zero ancilla. The particular case $p = n$ of this procedure was proposed for the other purpose in the paper [3].

We start with the state of the form (1), with the ancilla initialized by zeroes. The action of the operator W_H on the initial state with zero ancilla is defined as follows:

$$\mathrm{QFT}_M U_{\mathrm{seq}}^p \mathrm{WH}|\xi, 0^p\rangle. \qquad (2)$$

Why must this procedure work? Let us assume temporarily that the frequencies have an exact representa-

tion by their binary notation. Then the application of the first operator in definition (2) gives

$$\chi_0 = \frac{1}{\sqrt{M}}\sum_{k=0}^{N-1}\sum_{s=0}^{M-1} x_k|\Phi_k, s\rangle.$$

The second operator gives:

$$\chi_1 = U_{\text{sec}}^p\chi_0 = \frac{1}{\sqrt{M}}\sum_{k=0}^{N-1}\sum_{s=0}^{M-1} x_k\exp(2\pi i\omega_k s)|\Phi_k, s\rangle.$$

The third operator results in the target state

$$\sum_{k=0}^{N-1} x_k|\Phi_k, \bar{\epsilon}_k^p\rangle.$$

In the general case, the same idea works but with slight corrections resulting from the inaccuracy of frequencies. We will see below how to manage this error.

3.3. Accuracy of Finding the Frequencies

The feasibility of the simulation procedure results from the precise estimation of the inaccuracy in determining frequencies. The proof of this fact can replace Shor's substantiation of the factoring algorithm. The idea is similar to the uncertainty principle. Let ε and δ be the respective errors in a frequency binary approximation and in the probability of finding the right frequency by the observation of the corresponding ancilla. Then their product $\varepsilon\delta$ cannot be smaller than $1/M$. After some consideration, we agree that this formulation would be very natural. To formulate it carefully, we need a definition of a wide class of transformations with this property. Let $\{\tilde{\omega}_{k,i}\}$ be some set of integers. We denote $L_\varepsilon\{\tilde{\omega}_{k,i}\} = \{i: |(0.\tilde{\omega}_{k,i})_p - \omega_k| \le \varepsilon \text{ or } |(0.\tilde{\omega}_{k,i})_p - \omega_k - 1| \le \varepsilon\}$. Let ξ be a state of form (1).

DEFINITION

A transformation W of the form

$$W: |\xi, 0^p\rangle \longrightarrow \sum_{k=0}^{N-1}\sum_{i=0}^{M-1}\lambda_{i,k}|\Phi_k, \tilde{\omega}_{k,i}\rangle$$

is called a transformation of $W_{\delta,\varepsilon}$ type if $\sum_{k=0}^{N-1}\sum_{i\in L_\varepsilon(\tilde{\omega}_{k,i})}|\lambda_{i,k}|^2 \ge 1-\delta$ for any ξ.

Lemma 1. *The operator W_H belongs to the set $W_{1/K, K/M}$ for any $K \in \{1, 2, \ldots, M\}$.*

Consider a result of action of the operator W_H:

$$\chi_{p,2} = \frac{1}{M}\sum_{k=0}^{N-1}\sum_{l=0}^{M-1} x_k H_{l,k}|\Phi_k, l\rangle,$$

$$H_{l,k} = \sum_{s=0}^{M-1}\exp(2\pi i s(\omega_k - (0.l)_p)).$$

Put $\Delta = \omega_k - (0.l)_p$. By summing this progression, we then obtain

$$H_{l,k} = \frac{1-\exp(2\pi i M\Delta)}{1-\exp(2\pi i\Delta)}. \quad (3)$$

Let $\Delta = K/M + \delta$, $K = K(l)$, where $0 \le \delta < 1/M$; K is integer. Then each $H_{l,k}$ depends on K: $H_{l,k} = H_{l,k}(K)$. We fix some value for K: K_0. This means that the accuracy of eigenvalue approximations will be K_0/M. We estimate the sum of squared amplitudes for the states $|\Phi_k, l\rangle$ for which K: $K_0 \le K \le M - K_0$. The module of the denominator in Eq. (4) is separated from zero by $\min\{\pi K/M, \pi(M-K)/M\}$. We then have

$$\sum_{k=0}^{N-1}\sum_{K=K_0}^{M-K_0}|x_k|^2\frac{1}{M^2}|H_{l,k}(K)|^2$$

$$\le 4\sum_{k=0}^{N-1}\sum_{K=K_0}^{M-K_0}|x_k|^2/\pi^2K^2 \le \frac{4}{\pi^2}\sum_{K=K_0}^{M-K_0}\frac{1}{K^2} \le \frac{1}{K_0}.$$

Lemma 1 is proved.

What would happen if we applied another operator $\text{QFT}_M^{-1}(U_{\text{seq}}^p)^{-1}$ WH instead of (2) for revealing frequencies? Then the difference would be only in the simple factors of the basic states. This method is useful for a cleaning ancilla.

Lemma 2. *Let χ be a state and the application of Eq. (2) give $\chi_2 = \sum_k\sum_{l=0}^{M-1} y_{k,l}|\Phi_k, l\rangle$ and $\chi_2' = QF\text{T}_M^{-1}(U_{\text{seq}}^p)^{-1}$ WH $|\chi, 0^p\rangle = \sum_k\sum_{l=0}^{M-1} y_{k,l}|\Phi_k, l\rangle$. Put $\delta_{k,l} = \tilde{\omega}_k^N - (0.l)_p$, $\Delta = \omega_k - (0.l)_p$, $\chi_2'' = \sum_k\sum_{l=0}^{M-1} y'_{k,l}\exp(2\pi i(M-1)\delta_{k,l})|\Phi_k, l\rangle$. Let $M/N < \epsilon$. Then $\|\chi_2'' - \chi_2\| < 7\epsilon$.*

We have $y_{k,l} = x_k H_{k,l}$ (look at (3)), where $H_{k,l} = H_{k,l}(\Delta)$. Then $y'_{k,l} = x_k H_{k,l}(-\Delta)$. Now $H_{k,l}(\Delta) = H_{k,l}(-\Delta)\exp(2\pi i(M-1)\Delta)$, $|\delta_{k,l} - \Delta| \le 1/N$, $2\pi(M-1)|\delta_{k,l} - \Delta| \le 7M/N$ and Lemma 2 follows.

3.4. Complexity of the Method for Finding Frequencies

It is readily seen that the above procedure for $p = n$ requires N applications of the initial transformation U; hence, it cannot be used for the purpose of predicting its evolution. It turns out that, in the general case, it is impossible to simulate an action of the operator W_H with a precision up to $O(1/N)$ using less than $\Omega(N)$ conditional applications of the initial transformation U_{cond}. This follows from the lower bounds for quantum complexity of the parity function as $N/2$ (see [4, 5]). We

assume that an action of the operator W_H can be simulated using less than $\Omega(N)$ applications of U_{cond}. Then, in view of the previous subsection, we would be able to compute the function parity on a quantum computer in a time less than $N/2$ (by adding an appropriate constant to the number n in order to enhance an accuracy), which leads to the contradiction.

We note that the behavior of the bulk of classical systems in the general case in a short time frame is unpredictable on a quantum computer even one step ahead (see [6]), where a short time means approximately $O(N^{1/7})$, where N is the number of all states.

But for one class of systems, quantum prediction is possible. This is the class of systems with a sparse spectrum.

4. PREDICTION OF THE EVOLUTION OF SYSTEMS WITH A SPARSE SPECTRUM

What would happen if we used a smaller number of qubits $p < n$ instead of n in the ancilla? Simulation of the operator W_H wizard would be shorter, but it would be simulated with the corresponding loss in precision, and we obtain no prediction.

Nevertheless, if the spectrum is sparse, then prediction is possible. Indeed, suppose that we are given a classical algorithm h enhancing the accuracy of the eigenvalues approximation. Let $p < n$, $M = 2^p$, and let h: $\{0, 1\}^p \longrightarrow \{0, 1\}^n$ be an integer function mapping a rough frequency approximation up to $1/M$ to a more precise approximation up to $1/N$. The idea of the prediction is as follows. We repeat the procedure from above with only p ancillary qubits instead of n and then enhance accuracy by applying the function h.

We assume for simplicity that the frequency binary representation is exact. Our algorithm then has the following form.

First we apply the WH transform to the ancilla and obtain the state

$$\chi_0 = \frac{1}{\sqrt{M}}\sum_{k=0}^{N-1}\sum_{s=0}^{M-1} x_k|\Phi_k, s\rangle.$$

Then we apply the operator U_{seq}^p. This operation requires p conditional applications of U and results in the state

$$\chi_1 = \frac{1}{\sqrt{M}}\sum_{k=0}^{N-1}\sum_{s=0}^{M-1} \exp(2\pi i\omega_k s)x_k|\Phi_k, s\rangle.$$

Now, the application of the Fourier transform to the second register gives the state

$$\chi_2 = \sum_{k=0}^{N-1} x_k|\phi_k, \tilde{\omega}_k\rangle.$$

This is the point where we use the sparse spectrum. We add an ancillary register with n qubits initialized by zeroes: $\sum_{k=0}^{N-1} x_k|\Phi_k, \tilde{\omega}_k, 0^n\rangle$. We apply the unitary version of the algorithm h enhancing accuracy to two ancillary registers: $|a, b\rangle \longrightarrow |a, b \oplus h(a)\rangle$. This gives the state $\sum_{k=0}^{N-1} x_k|\Phi_k, \tilde{\omega}_k, h(\tilde{\omega}_k)\rangle$. We then turn every state of the form $|\Phi_k, \tilde{\omega}_k, l\rangle$ through the angle $2\pi \cdot 0.l \cdot t$ and obtain the state

$$\sum_{k=0}^{N-1} x_k \exp(2\pi i \cdot 0.l \cdot t)|\Phi_k, \tilde{\omega}_k, l\rangle.$$

Here, t is a given time instant. We apply the unitary version of h, which cleans up the n last ancillary qubits and then discard them:

$$\sum_{k=0}^{N-1} x_k \exp(2\pi\omega_k t)|\Phi_k, \tilde{\omega}_k\rangle,$$

and again QFT_M to the p ancillary qubits:

$$\frac{1}{\sqrt{M}}\sum_{k=0}^{N-1}\sum_{s=0}^{M-1} x_k \exp(2\pi i\omega_k t)\exp(-2\pi i\tilde{\omega}_k s)|\Phi_k, s\rangle,$$

then again U_{seq}^p and the WH transform to the ancilla. The result has the following form:

$$\sum_{k=0}^{N-1} x_k \exp(2\pi i\omega_k t)|\Phi_k, 0^p\rangle.$$

The target state is now in the main register.

Why does this scheme not work for the case where the binary notation from ancilla is the approximation of the true eigenvalues ω_k? The reason is the same as above. To make the necessary corrections, we need only to apply the multipliers that arose in Lemma 2. The resulting algorithm looks more complicated but, in fact, differs only in the point 4, where we correct undesirable phase shifts. Its scheme is as follows.

We are given the numbers n and p. We choose some q: $p \le q < n$ and put $L = 2^q$. Our initial state has the form $\xi = \sum_{k=0}^{N-1} x_k|\Phi_k, 0^q\rangle$:

1. We apply operator (2) to the initial state.

2. We add one more register with n qubits initialized by zeroes: $\sum_k \sum_{l=0}^{L-1} y_{k,l}|\Phi_k, l, 0^p\rangle$ and apply the unitary version of the algorithm h enhancing accuracy to two ancillary registers:

$$\chi_3 = \sum_k \sum_{l=0}^{L-1} y_{k,l}|\Phi_k, l, h(l)\rangle.$$

3. We turn every state of the form $|\Phi_k, l, h(l)\rangle$ through the angle $2\pi \cdot 0.h(l) \cdot t$ and obtain the state

$$\chi_4 = \sum_k \sum_{l=0}^{L-1} y_{k,l} \exp(2\pi i \cdot 0.h(l) \cdot t) |\Phi_k, l, h(l)\rangle.$$

Here, t is the given time instant.

4. We put $\delta^*_{k,l} = (0.h(l))_n - (0.l)_q$. We turn every state of the form $|\Phi_k, l, h(l)\rangle$ through the angle $-2\pi(L-1)\delta^*_{k,l}$. The result is denoted by χ_5.

5. We apply the unitary version of h, which cleans up the n last ancillary qubits and then discard them:

$$\chi_6 = \sum_k \sum_{l=0}^{L-1} y_{k,l} \exp(2\pi i \cdot 0.h(l) \cdot t) \times \exp(-2\pi i(L-1)\delta^*_{k,l}) |\Phi_k, l\rangle.$$

6. We apply to χ_6 the transformation WH U^q_{sec} QFT_L, then observe and discard the ancilla.

The time of this algorithm is $2L + 2t_{\text{QFT}_L} + 2t_h + w$, where t_{QFT_L} is the time of the Fourier transform, t_h is the time of enhancing accuracy, and w is the time of rotations.

Let $\delta > 0$ be some number, $q = p + c$, $L = 2^q$, t: $0 < t \le CN$, where $c = \log_2(4/\delta)$, $p \ge c$, $C = \delta/14$. Then a straightforward calculation based on Lemmas 1 and 2 gives an estimate for the difference between the result of this algorithm and the ideal state as δ.

This result can be formulated in the following convenient form:

Given a Hamiltonian of a system with the sparse spectrum and an algorithm enhancing the accuracy of eigenvalues from ε_1 to ε and a fidelity ρ, a state of the system at the time $(1-\rho)/14\varepsilon$ can be obtained in the time $4/(1-\rho)\varepsilon_1$ with this fidelity.

4.1. Generalizations, Examples and Practical Implementation

We note that the spectra of real systems like molecules typically contain bands, where the spectrum is a continuum separated by gaps and the energy levels are absent altogether. Let w be the maximal width of bands and g be the minimal width of gaps.

Considering the evolution in the time frame less than $1/w$ (here we assume the system of units where Plank's constant is unity), we obtain the following generalization of the result from the previous section.

If $t = o(1/w)$, we can compute the state $U(t)$ of the primary system in the time $t_{pre} = O(tw/g)$.

The more general result can be obtained if we consider a spectrum that is not sparse but has sparse areas.

The operator H_W can be used not only for the prediction of the future but for the restoration of history as well. *The states of the primary system at the time instant $T = (1-\rho)/14\varepsilon$ in future and at the time $-T$ in the past can be obtained in the time $4/(1-\rho)\varepsilon_1$ with the fidelity ρ, provided each eigenvalue can be quickly calculated with precision up to ε, given its approximation with the accuracy ε_1.*

Formula (2) can be considered as a natural generalization for the quantum part of the Shor factoring algorithm [1]. Our approach applies to the factoring problem if U has the form $U|x\rangle \longrightarrow |ax(\text{mod } q)\rangle$, where ax is a multiplication of integers and $(a, q) = 1$ with eigenvectors of U of the form

$$\frac{1}{\sqrt{r}} \sum_{j=0}^{r-1} \exp(-2\pi ikj/r) |a^j (\text{mod } q)\rangle$$

with the eigenvalues $\exp(2\pi ij/r)$, where r is the period of a (the minimal integer such that $a^r \equiv 1 \pmod q$).

The main difficulty for the practical implementation of this method is contained in the conditional iterations of U. This scheme can be reformulated by means of analogous quantum computing if we consider QFT on an ancillary register as a passage to the canonically conjugate magnitude. For instance, if we use a value of coordinates in operations with a register, then the corresponding momentum will be canonically conjugate. The passage from the coordinate representation of a wave function to the momentum representation in the one-dimensional case can be defined as

$$\phi(p) = \int_{-\infty}^{+\infty} \exp(-ipx/h)\psi(x)dx,$$

where the probability of obtaining the momentum in a segment $(p, p + dp)$ is $|\phi(p)|^2 dp/2\pi h$. Assume that we have one particle that can be located at M points of the form $x = 0, 1/M, 2/M, \ldots, (M-1)/M$. Then the coordinate quantum space for one particle will be M-dimensional. Consider the corresponding integral sum for $\phi(p)$ in the system of units where Plank's constant h equals one. This integral sum will be just the sum in the definition of QFT where x plays the role of s/M and $p/2\pi$ plays the role of l.

Then the main algorithm acquires the following general form:

(a) primary evolution quantum-mechanically controlled by a magnitude contained in the properly prepared ancillary register;

(b) simple actions depending on the canonically conjugate magnitude;

(c) the repetition of (a).

Such a procedure can predict the behavior of a primary system with a sparse spectrum and restore the state of an arbitrary system in the past.

I am grateful to L. Grover for his kind invitation to Bell Labs, discussions, and attention to my work. I also thank P. Hoyer and D. DiVincenzo for fast replies and useful comments.

This work was performed while the author was at Bell Labs, Lucent Technologies. It was supported by the U.S. Army Research Office (contract no. DAAG55-98-C-0040).

REFERENCES

1. P. W. Shor, SIAM J. Comput. **26** (5), 1484 (1997); quant-ph/9508027.
2. L. K. Grover, in *Proceedings of STOC* (Philadelphia, PA, 1996), p. 212; quant-ph/9605043.
3. D. S. Abrams and S. Lloyd, quant-ph/9807070.
4. E. Farhi, J. Goldstone, S. Gutmann, and M. Sipser, Phys. Rev. Lett. **81**, 5442 (1998); quant-ph/9802045.
5. R. Beals, H. Buhrman, R. Cleve, *et al.*, quant-ph/9802049.
6. Y. I. Ozhigov, Chaos, Solitons and Fractals **10** (10), 1707 (1999); quant-ph/9803064.

JETP Letters, Vol. 76, No. 11, 2002, pp. 681–692. Translated from Pis'ma v Zhurnal Éksperimental'noĭ i Teoreticheskoĭ Fiziki, Vol. 76, No. 11, 2002, pp. 805–817.

Interplay between the Structure and Properties of New Metastable Carbon Phases Obtained under High Pressures from Fullerite C_{60} and Carbyne

V. V. Brazhkin*, A. G. Lyapin*, S. V. Popova*, S. C. Bayliss, T. D. Varfolomeeva*, R. N. Voloshin*, A. G. Gavrilyuk*, M. V. Kondrin*, V. V. Mukhamad'yarov*, I. A. Troyan*, S. V. Demishev***, A. A. Pronin***, and N. E. Sluchanko*****

**Institute of High-Pressure Physics, Russian Academy of Sciences, Troitsk, Moscow region, 142190 Russia*
e-mail: brazhkin@hppi.troitsk.ru
***Department of Chemistry, School of Applied Sciences, De Montfort University, The Gateway, LE1 9BH, Leicester, England*
****Institute of General Physics, Russian Academy of Sciences, Moscow, 117942 Russia*
Received October 23, 2002

A brief review of structural, electrotransport, optical, elastic, and mechanical properties of carbon phases synthesized under pressure by heating fullerite C_{60} and carbynoid materials is given. A large variety of carbon modifications with a variable bonding type, a variable mean coordination number, a variable molecular or atomic structural type, a variable characteristic dimensionality (from zero- to three-dimensional structures), a variable degree of covalence, etc., were prepared. Emphasis in the review is given to the elucidation of the interplay between the structural and topological characteristics of carbon phases and their key electronic and mechanical properties. A version of the kinetic phase diagram of fullerite C_{60} transformations on heating under pressure is also suggested. This version is modified with respect to the interpretations known in the literature. © *2002 MAIK "Nauka/Interperiodica".*

PACS numbers: 64.70.Kb; 61.50.Ks; 62.50.+p; 61.48.+c; 81.30.-t

1. INTRODUCTION

New carbon materials attract particular attention because of their unique combination of physical properties and the possibilities of numerous practical applications. Interatomic bonds in carbon substances are extremely short and strong, which, along with the small atomic weight of the carbon atom, leads to uniquely high mechanical characteristics of carbon materials with their rather low density (diamond, lonsdeylite, carbon-based fiber materials). Carbon materials exhibit a wide range of electrophysical and optical properties from the typical wide-bandgap dielectric diamond to the semimetallic graphite.

Only two solid phases are present in the equilibrium carbon phase diagram in the experimentally accessible range of pressures, which have the stability region corresponding to graphite and diamond [1, 2]. Graphite has a quasi-two-dimensional layered structure with atoms in trivalent sp^2 states. Carbon atoms in the diamond lattice have four nearest neighbors each being in the sp^3-hybridized state. In addition to the rhombohedral graphite modification and the hexagonal analogue of diamond, lonsdeylite [1, 2], a virtually continuous series of amorphous carbon phases differing in the fraction of atoms occurring in the tri- and tetravalent states should be primarily mentioned [3–5].

In the general case, carbon atoms in solid phases can exhibit a valence from 2 to 4, being in sp^1, sp^2, or sp^3 states, respectively. The reason for the occurrence of various types of chemical bonds between carbon atoms and the existence of a large number of carbon modifications is associated with the fact that the bond energies per atom are close to each other for various carbon states. In its turn, this is due to the small size of the inner electron shell of the carbon atom and the high energy of π bonds [6].

New metastable carbon materials have been discovered in the last few years, such as fullerites [7], nanotubes [8], and carbynes [9, 10]. Fullerites represent crystals built of closed spherical fullerene molecules bonded by weak van der Waals forces [11]. The states of carbon atoms in the molecule are close to the sp^2 hybridization of valence electrons. C_{60} fullerite is of greatest interest, because the C_{60} molecule is the most stable among fullerenes. Carbynes combine a whole group of amorphous and crystalline phases composed of fragments of quasi-one-dimensional carbon chains. Inside the chains, carbon atoms are in predominantly divalent sp^1 states. Because of their sufficiently high chemical activity, carbynes generally contain an appreciable amount of impurities, and researchers often deal with carbynoid materials. In fact, carbynoid materials represent solid carbon phases with atoms occurring in

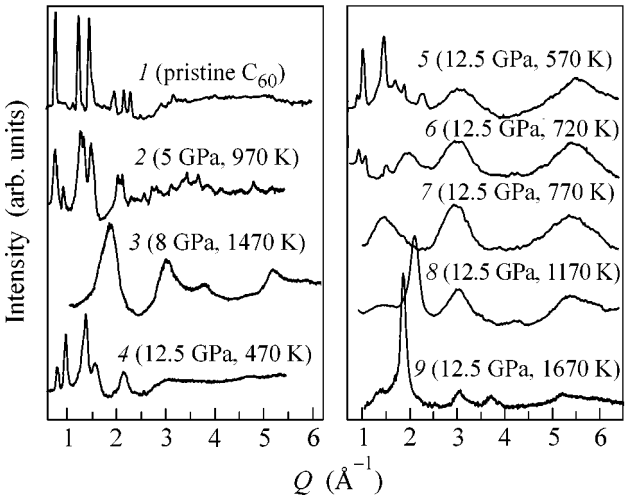

Fig. 1. Typical X-ray diffraction patterns (after background subtraction) for carbon phases synthesized from C_{60} fullerite. The synthesis conditions are indicated in parentheses. The corresponding structures were identified as follows: (*1*) starting C_{60}, (*2*) 2D polymerized rhombohedral phase, (*3*) disordered nanocrystalline graphite-like (sp^2) phase, (*4*)–(*6*) 3D polymerized phases differing in the degree of polymerization (lattice parameter) and in the degree of disordering, (*7*) and (8) disordered (amorphous) sp^2–sp^3 phases differing in nanomorphology and in sp^2/sp^3 ratio, and (*9*) diamond–graphite nanocomposite.

both sp^1 and sp^2 states with a significant amount (up to several percent) of impurities of other elements [9, 10, 12].

Fullerites and carbynes are high-energy metastable phases; that is, their free energy under normal conditions significantly exceeds the free energies of graphite and diamond. It is likely that new metastable carbon phases with intermediate Gibbs energies will arise under pressure on the fullerite and carbyne transformation pathway to stable carbon modifications, which, indeed, is observed experimentally.

In this work, we present a review of our original results in the context of a wider set of data published in the scientific literature on the structural, electronic, and mechanical properties of new metastable carbon phases obtained from fullerites and carbynes under high pressures (P) and temperatures (T).

2. EXPERIMENTAL PROCEDURE

In what follows, we will deal with carbon materials obtained by thermobaric treatment of a fullerite or carbyne powder followed by quenching to normal conditions. "Toroid" chambers of various size were used for creating high pressure with a maximum pressure up to 14 GPa.

The synthesis of fullerite-based samples was carried out from a powder containing no less than 99.9% of C_{60} with crystal grains of size ~100 μm. The starting amorphous carbyne used in the experiments was synthesized by low-temperature dehydrohalogenation of poly(vinylidene chloride) [9, 10]. This material can be characterized as cumulene-type chains (=C=C=C=) interrupted with kinks of atoms in sp^2 states [9, 10, 13]. The chemical state of carbon atoms in carbyne samples and their elemental composition were determined by X-ray photoelectron spectroscopy. K, Cl, and O impurities were detected, and the element concentrations were calculated from integrated C1*s*, F1*s*, O1*s*, Cl2*p*, and K2*s* spectra [12]. The K and Cl contents did not exceed 2%, and the fraction of oxygen varied in the range from 8 to 22%, depending on the storage time. The carbynoid powder with the lowest O content was used for experiments.

The structure of the samples was studied by X-ray diffraction (CuK_α and CrK_α). The density of the samples was measured by a pycnometer. A specially designed capacitance dilatometer was used for measuring the thermal expansion of weakly polymerized C_{60} samples. The temperature dependence of the static conductivity for carbyne samples was studied in the range $1.8 < T < 300$ K. Ultrasonic measurements of elastic properties were carried out by measuring the traveling time of longitudinal and transverse ultrasonic waves through a sample at a frequency of 10 MHz. The mechanical properties were measured by the Vickers diamond pyramid indentation method under loads up to 5.5 N on a PMT-3 hardness tester modified for large loads. The Vickers hardness H_V and the critical stress intensity (crack resistance) factor were calculated according to the procedure proposed in [14].

3. STRUCTURE AND VALENCE STATES OF C_{60}-BASED PHASES

A wide variety of ordered or disordered carbon phases can be synthesized by the action of high pressures and temperatures on C_{60} fullerite (see, for example, reviews [15–18]). Among them are dimeric and weakly polymerized phases [19, 20], one-dimensionally (1D) and two-dimensionally (2D) polymerized C_{60} phases [21–26], disordered graphite-like (sp^2) structured phases [23, 27, 28], three-dimensionally (3D) polymerized phases with a variable degree of polymerization [29–34], diamond-like (that is, predominantly sp^3) amorphous phases [33–36], and nanocrystalline composites [33, 34, 37]. Typical X-ray diffraction patterns for the above phases are shown in Fig. 1. Whereas polymerized phases may be considered as molecular modifications of C_{60}, many of which can be depolymerized to the starting fullerite (see, for example, [21, 38] for 2D and [31] for 3D polymers), disordered and nanocrystalline sp^2–sp^3 phases are atomically structured, that is, correspond to irreversible destruction of the C_{60} structure. Therefore, it is natural to consider these two groups of carbon materials separately.

3.1. Dimeric and Polymerized Phases

A high degree of fullerite dimerization, that is, the formation of covalently bonded $(C_{60})_2$ pairs, is observed even at relatively low temperatures under pressure (for example, at ~400 K and 1.5 GPa) [19] or under compression at room temperature [20]. The dimerization process is well detected both by spectroscopic methods and from the magnitude of the volume jump (Fig. 2) [20] corresponding to the phase transition of the orientationally ordered simple cubic lattice to an orientationally disordered fcc lattice in the range 230–260 K [39]. The covalent bonding of molecules leads to a loss of rotational degrees of freedom by the C_{60} molecule. Dimerization proceeds continuously both upon the variation of external parameters (Fig. 2) and in time [40]. The structure of partially dimerized phases corresponds to an effective fcc lattice with a somewhat reduced lattice parameter [19, 20].

Upon heating C_{60} in the pressure range below 8 GPa, 1D and 2D polymerized C_{60} phases are formed. These phases consist, respectively, of covalently bonded chains or planes of C_{60} molecules [21–26, 28]. Three polymer phases were detected and identified: 1D orthorhombic (*O*), 2D tetragonal (*T*), and 2D rhombohedral (*R*) (curve *2* in Fig. 1). Structural models of these phases were proposed in [21, 22]; however, it has been shown more recently that the best packing of molecules corresponds to somewhat different structures and symmetry groups of these phases (see references in [26]). Two *O* phases were distinguished in [24]—a low-pressure phase and a high-pressure phase. Detailed information on the structure of the *O*, *T*, and *R* phases can be found in the original works cited above. It is important to emphasize that not only the morphology but also the phase composition may depend on the *P*–*T* trajectory [25]. In many cases, both 1D and 2D polymerizations proceed as a continuous process, that is, through partially polymerized phases [23, 28]. The most detailed *P*, *T* diagram of transformations to 1D and 2D polymerized C_{60} phases is given in [26].

A [2 + 2] cycloaddition reaction was suggested as the mechanism of C_{60} polymerization [41], where a polymerized pair of molecules is connected by two covalent bonds, and the four involved atoms undergo transition from the sp^2 state to sp^3. ^{13}C NMR experiments [42–44] gave a direct confirmation of this mechanism in the *O*, *T*, and *R* phases. Note that the sp^3/sp^2 ratio for the ideal defect-free *O*, *T*, and *R* phases comprises 1/14, 2/13, and 1/4, respectively.

At pressures above 8 GPa, the pattern of polymerization changes substantially (curves *4*–*6*, Fig. 1). In this case, 3D polymerization proceeds [29–34], for which covalent bonds between molecules are formed in all possible directions and the fcc lattice parameters of C_{60} fullerite decrease along all three crystallographic directions. Note that the structure of 3D polymerized phases is differently identified in the literature (see [32]); however, recent studies of the structure of 3D polymers and the kinetics of its variation with time directly under pressure carried out with the use of synchrotron radiation [45] fully confirm the interpretation of experimental data and the concept of 3D polymerization presented in this review [31, 33, 34, 46].

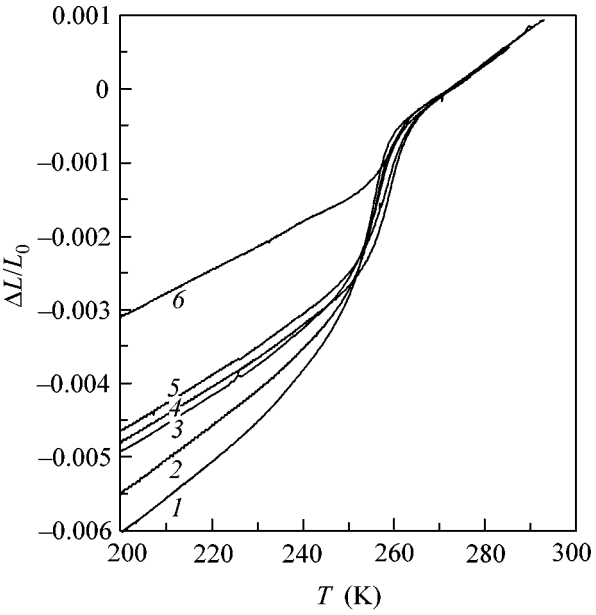

Fig. 2. Variation of the relative volume as a function of temperature in the region of an orientational phase transition for C_{60} samples after a thermobaric treatment: (*1*) P_{syn} = 2.5 GPa and T_{syn} = 290 K, (*2*) 2.5 GPa and 330 K, (*3*) 2.5 GPa and 360 K, (*4*) 5 GPa and 330 K, (*5*) 8 GPa and 290 K, (*6*) 8 GPa and 310 K. The curve for a sample synthesized at 2.5 GPa and 290 K virtually coincides with the curve for the starting C_{60}.

X-ray diffraction patterns for 3D polymers are well described within the framework of an fcc structure. The lattice parameter *a* can vary in this case virtually continuously from 14.17 Å (starting C_{60}) to ≈11.6 Å for samples quenched to normal conditions [31, 33, 34] or from ≈13 to ≈11.6 Å under a pressure of 12–14 GPa [45]. A good agreement between the crystallographic and experimental density values was noted in [31, 33]. Distortions of the fcc structure [47] and the appearance of ellipsoidal Debye–Scherrer diffraction patterns from 3D polymers of C_{60} molecules [48] are possible under nonhydrostatic synthesis conditions.

A detailed analysis of X-ray data [33] distinguished two stages of 3D polymerization: (1) gradual formation of covalent bonds between pairs of neighboring molecules, likely through the mechanism of [2 + 2] cycloaddition, and (2) the formation of additional covalent bonds after complete polymerization and a gradual transformation of the 3D polymer of C_{60} molecules to a disordered amorphous phase with a large fraction (~80%) of sp^3 atoms. Note that the amplitude of X-ray reflections at the first stage is well described in the

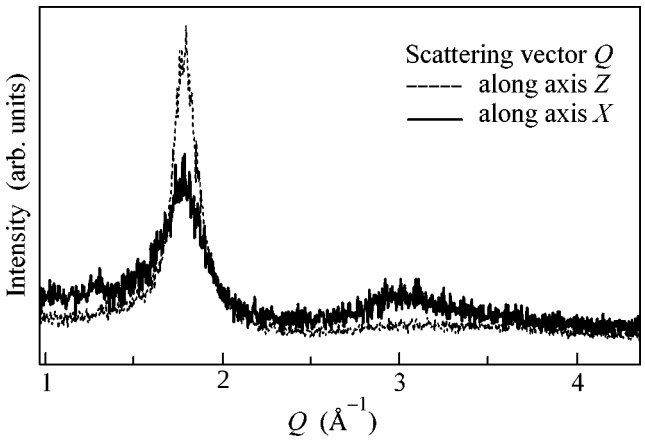

Fig. 3. Structural anisotropy of a disordered graphite-like phase synthesized under nonhydrostatic conditions (*z* is the load axis) illustrated by X-ray diffraction obtained by reflections from different faces of a sample.

approximation of an fcc crystal and a spherical molecular scattering factor of the C_{60} molecule [33]. At the same time, electron microscopy provides direct evidence for significant distortions of sphericity at the second stage [49].

A quantitative model was proposed in [31, 33] for the description of the first polymerization stage, in which a 3D polymer is considered as a mixture of polymerized (covalently bonded) and nonpolymerized (van der Waals) pairs of molecules within the framework of an effective fcc crystal. This model describes the specific features of X-ray diffraction patterns [31, 33] and the Raman spectra of 3D polymers [33, 46] well. One of the greatest successes of this model consists in the prediction of the rigidity threshold for the mechanical properties of 3D polymers [31, 33]. Note also that the proposed model explains in a natural way the possibility of Debye–Scherrer ellipses for 3D polymers of C_{60} [48] and offers advantages over the original interpretation given in [48]. Such a diffraction pattern can be a consequence of the orientational dependence of both the degree of polymerization and the effective lattice parameter for Bragg reflections in different directions.

Theoretical models have been proposed recently for ordered 3D polymerized phases [50–52]. The experimental synthesis of such phases can be expected only in the future, for example, with the use of further polymerization of structurally ordered 1D or 2D C_{60} polymers, whereas the synthesized 3D polymers likely have a high degree of orientational (for molecules) and topological (for bonds between molecules) disorder [18, 33, 46, 53].

3.2 Amorphous and Nanocrystalline C_{60}-based Phases

The further heating of C_{60} fullerite under different pressures leads to the irreversible destruction of its molecular structure and to the formation of various disordered phases based on atomic carbon [23, 27–37, 45–47, 49]. One can distinguish between the interval of low pressures up to 10–11 GPa, where graphite-like disordered phases with densities in the range 1.9–2.3 g/cm^3 are formed [23, 27, 28, 30, 46, 47, 49], and the high-pressure range above 12 GPa, which corresponds to the formation of denser amorphous and composite phases with a large fraction of atoms in the sp^3 states (including amorphous and nanocrystalline diamond) [29, 30, 32–37, 46].

A typical X-ray diffraction pattern for graphite-like disordered phases presented in Fig. 1 (curve *3*) corresponds to the known patterns for amorphous sp^3 carbon phases. Atomic-resolution electron microscopy [54] demonstrates that these phases are formed from nanocrystallites with graphite-like packing of atoms and a typical size of ~30 Å. In addition, correlation exists in the mutual orientation of nanocrystallites [54, 55]. The scale of these correlations is large and exceeds micron distances [55]. It is natural to relate the occurrence of such large-scale correlations to the starting structure of the decomposed fullerite. At the same time, the diffusional nature of the formation of disordered sp^2 phases of C_{60} is beyond question. This is also corroborated by the weak baric dependence of the disordering temperature of 2D C_{60} polymers [23, 28, 49]. Another interesting property of the disordered sp^2 phases is the orientational anisotropy of the structure (Fig. 3) obtained in the synthesis under nonhydrostatic conditions. The occurrence of a texture in the system of nanoclusters is a consequence of the nonuniform distribution of orientations of graphite nanocrystals with respect to different axes [56].

A basically different pattern of transformations is observed at higher pressures >12 GPa (Fig. 1, curves *7*–*9*). A typical series of high-temperature transformations for pressures in the range 12.5–14 GPa can be described by the following sequence: (1) strongly polymerized 3D C_{60} polymers with a high degree of disorder (Fig. 1, curve *6*), (2) diamond-like amorphous phases with a high fraction of sp^3 states (curve *7*), (3) amorphous heterogeneous sp^2–sp^3 phases (curve *8*), and (4) nanocrystalline graphite–diamond composites (curve *9*). It is evident that the fraction of sp^2 states must become negligible with increasing pressure, which is observed in shock experiments at pressures above 20 GPa [35, 36], where amorphous diamond-like (sp^3) carbon is formed. Under static compressions at room temperature, the molecular structure is stable approximately up to 20 GPa, after which the irreversible transformation to an amorphous optically transparent sp^3 phase with a possible admixture of crystalline diamond is observed [57, 58]. From the experimental results mentioned above, it evidently follows that the amorphization temperature of the molecular structure essentially depends on the pressure, which is confirmed

by direct measurements of electrical conductivity at various *P–T* conditions [59].

Note that the change of the scenario of the destruction of the molecular C_{60} structure into graphite-like sp^2 phases to the regime of the formation of sp^2–sp^3 amorphous structures occurs at higher pressures (11–13 GPa) than the crossover between 2D and 3D polymerization (8–9 GPa) [46].

3.3. Phase Diagram of Structural Transformations of C_{60}

A kinetic phase diagram of structural transformations of C_{60} fullerite is presented in Fig. 4. This diagram summarizes the discussion presented in the previous sections and is constructed with regard to both original results and published data. The phase-transition curves in the monomeric C_{60} phase and the regions of the formation of 1D and 2D polyfullerenes are reproduced from [17] and [26], respectively. The stability boundary of these phases (up to 8 GPa) is taken from [26] with allowance for the phase diagrams from [17, 23, 49] and the data from [24, 28]. In fact, a concentration isoline is first constructed in this diagram with regard to the results obtained in [19, 20]. The region >10 GPa is presented according to the results of our works [31, 33, 46] and data from [45].

We emphasize that this diagram has not conventional character and, basically, cannot be unambiguous. The structure of the formed phases may depend, not only on the kinetic conditions of the experiment (see, for example, [19, 24]), the path in the *P–T* plane, and the hydrostatic conditions, but also on the starting orientational state of C_{60} molecules [60]. We distinguished between three classes of lines (Fig. 4): phase boundaries for the monomeric C_{60} phase, which were determined thermodynamically for the molecular substance; lines of sharp structural transformations, such as the stability boundary of polymolecular phases; regions of gradual transformations, such as dimerization and 1D, 2D, or 3D polymerization, where the line has fully conventional character and can be constructed in a physically definite way only from the percolation point of view.

The diagram of transformations constructed here for the region of high pressures >10 GPa is notably different from that proposed previously in [32] or, in a modified form, in [61], which was repeatedly reproduced in a number of works, for example, in [16, 17]. First, the destruction boundary of polymolecular states in [32, 61] depends sharply and nonmonotonically on pressure, which contradicts the thermally activated diffusional nature of these structural processes. Moreover, the identification of the bcc phase in the region of 3D polymers in [32] is based on an analysis of powder diffractograms containing only a few broadened reflections and is incorrect in our opinion. The point of view presented in this work is confirmed, as was already

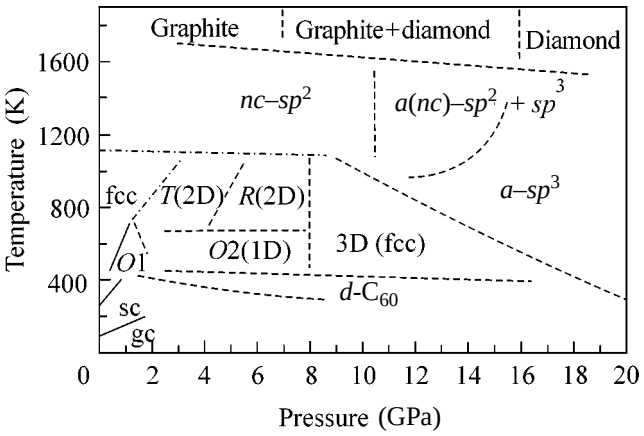

Fig. 4. Nonequilibrium (kinetic) phase diagram of C_{60} transformations under high pressures and temperatures, which partially reproduces diagrams from [17] and [26]. The diagram is extended on the basis of the experimental data discussed in this work (see Section 3). Solid lines correspond to the thermodynamic phase boundaries for monomeric phases; dot-and-dash lines correspond to the irreversible but sharp structural transformations; dashed lines correspond to the rather smooth transformations and separate regions of different classes of structures synthesized from C_{60}. The corresponding phases or classes of structures are designated as follows: fcc, sc, and gc correspond to monomeric phases, including the fcc and the primitive cubic phases with rotation of molecules and with the frozen glassy state of molecular orientations; *O*1, *O*2, *R*, and *T* are low-pressure and high-pressure 1D orthorhombic phases, and 2D rhombohedral and tetrahedral phases; *d*-C_{60} are phases with a predominant concentration of $(C_{60})_2$ dimers; *nc*–sp^2 are disordered (nanocrystalline) graphite-like phases; 3D (fcc) are 3D polymerized C_{60} phases; *a*–sp^3 and *a*(*nc*)–sp^2 + sp^3 are amorphous phases with possible nanocrystalline inclusions in the second case.

mentioned above, by recent synchrotron studies [45], in which only diffraction patterns from polymerized fcc phases with the lattice parameter varying continuously with time were, in particular, observed directly under pressure.

4. CARBYNE GRAPHITIZATION

X-ray diffraction patterns after thermobaric carbyne treatment are presented in Fig. 5. The action on the starting carbyne by pressures ≈8 GPa (curve *1*) does not lead to a significant change in the diffraction pattern, which corresponds to a strongly disordered substance. On heating to ≈800 K (curve *2*), structural changes are insignificant, and only a small peak appears in the region of 3 $Å^{-1}$. However, a significant structural rearrangement is observed in the range 900–1000 K, and the new structure corresponds to a disordered graphite-like (sp^2) phase (curve *3*). The Raman spectra of the treated carbyne samples fully confirm this pattern [46]. In particular, the occurrence of a line at 2150 cm^{-1} in the spectra of the starting carbyne [46] corroborates the

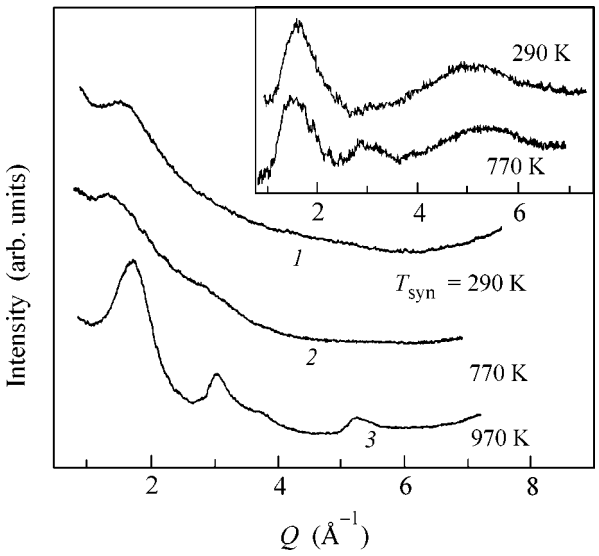

Fig. 5. X-ray diffraction patterns for carbyne samples after a thermobaric treatment under a pressure of 7.7 GPa. For convenience, the spectra are vertically shifted. The inset shows the same curves after background subtraction.

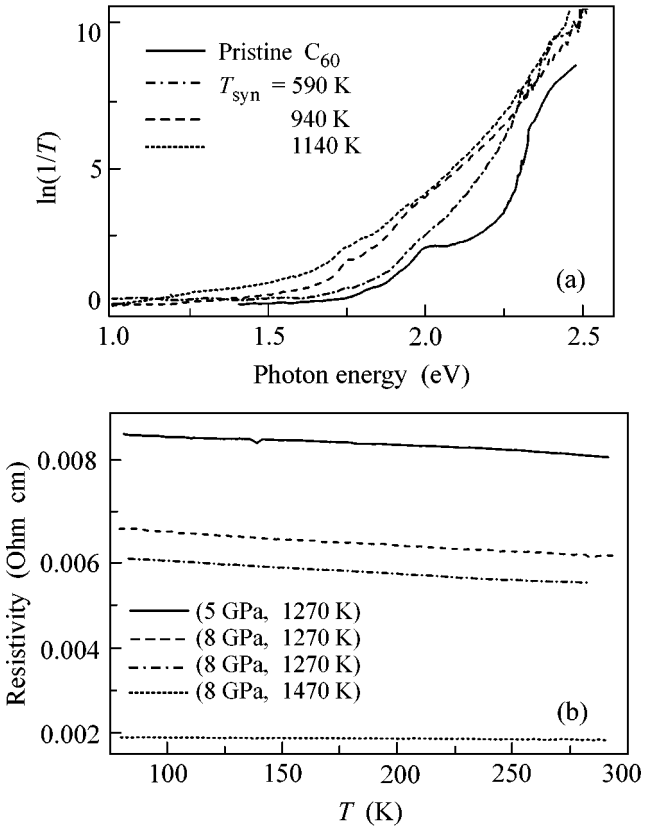

Fig. 6. Electronic properties of phases synthesized from C_{60} at $P < 8$ GPa. (a) Inverse transmission spectra for 1D polymerized (T_{syn} = 590 K) and 2D polymerized (940 K and 1140 K) C_{60} fullerite phases synthesized under a pressure of 8 GPa in comparison with the spectrum of the starting C_{60}. (b) Conductivity of disordered graphite-like phases obtained after destruction of the molecular structure (the synthesis conditions are indicated in parentheses).

fact that a considerable number of atoms are in the sp^1 states. However, a thermobaric treatment leads to the disappearance of this line even at modest temperatures ≈600 K. In this case, the absolute values of the absorption coefficient in the wavelength range 100–4000 cm^{-1} appreciably increase as a result of heating and graphitization.

5. ELECTRONIC PROPERTIES

A detailed review of electronic and optical properties of monomeric and polymerized fullerenes is given in [62]. Here, we will present a brief analysis of electrotransport and optical properties of a wider range of carbon phases obtained from C_{60} fullerite and carbyne (see also [46]), which demonstrates that the semiconducting or semimetallic nature of these phases is determined not only by their valence state, that is, the ratio between the numbers of atoms in the sp^1, sp^2, and sp^3 states but also by the structural topology, molecular or atomic character, and the degree of heterogeneity.

5.1. C_{60}-based Carbon Phases

The starting C_{60} fullerite is a semiconductor whose band-gap width, according to various sources, lies in the range 1.5–2.3 eV [62]. The conductivity of crystalline C_{60} is, as a rule, described by an activation law and, presumably, has a hopping mechanism at low temperatures [62]. Under reversible shock compression of C_{60} up to pressures above 10 GPa, the fullerite resistivity drops by 7–8 orders of magnitude down to values of ~0.2 Ω cm at starting room temperature or ~15 Ω cm for a sample cooled down to 77 K in the starting state, which corresponds to a semiconducting-type dependence of conductivity in the compressed state [63].

1D and 2D polymerization leads to a shift of the optical absorption edge to lower energies (Fig. 6a), which, in many instances, is similar to the edge shift in the case of simple compression of C_{60} [64]. However, rather extended absorption tails appear in polymerized phases. The electrical conductivity of polycrystalline 1D and 2D polymers notably increases compared to pristine C_{60}, although still remains rather low ($<10^{-8}$ (Ω cm)$^{-1}$) [65–67]. The activation energy for the temperature dependence of the conductivity also decreases as a result of polymerization [65–67]. A more detailed study of highly oriented 2D polymers [66–68] points to a significant anisotropy of electrical properties, and a quasimetallic dependence of conductivity is observed at high temperatures along the polymerized planes.

The destruction of 1D and 2D polymers at high temperatures leads to a sharp drop in resistivity (Fig. 6b) (see, also, [27, 28, 46]), which, evidently, is associated with the formation of atomic graphite-like phases.

Transparent amorphous phases [35, 36, 57, 58] formed under high pressures >20 GPa are wide-band-gap semiconductors whose bandgap width is somewhat

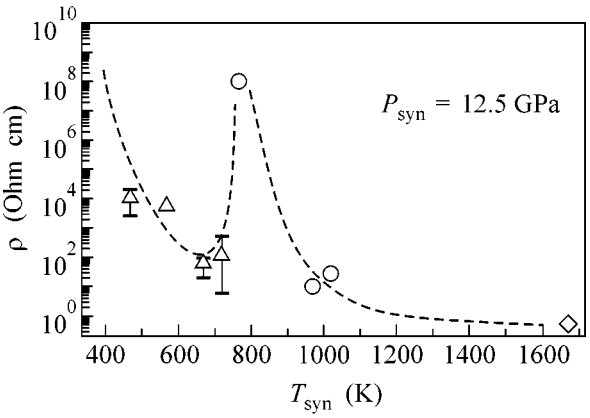

Fig. 7. Resistivity measured under normal conditions for samples of 3D C_{60} polymers (triangles), amorphous sp^2–sp^3 phases (circles), and a nanocrystalline graphite–diamond composite (rhombus) synthesized at 12.5 GPa. Dashed lines are drawn by the eye guide.

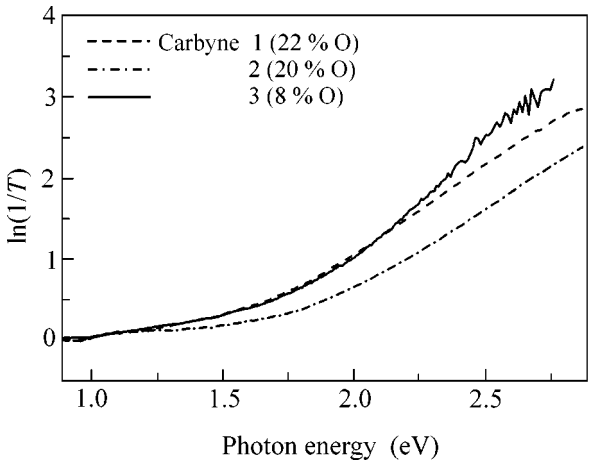

Fig. 8. Inverse transmission spectra for carbynes differing in the oxygen impurity concentration (indicated in parentheses).

narrower than in crystalline diamond [70]. A more complicated pattern is observed at intermediate pressures in the region of 3D polymerization (Fig. 7). 3D polymers (with a high degree of polymerization) have a low resistivity with a small negative temperature coefficient [46] and, likely, are narrow-bandgap semiconductors. The formation of amorphous diamond-like phases (Fig. 1, curve *7*) is accompanied by a sharp increase in resistivity (Fig. 9) and in semiconductor bandgap [70]. However, the formation of low-ohmic graphite-like clusters (Fig. 1, curve *8*) and conduction percolation over these clusters lead again to a drop in resistivity. It is evident that, with increasing pressure, the fraction of sp^2 clusters must drop and the resistivity of phases must increase, approaching the characteristics of amorphous diamond. It was reported that Mott's law and the temperature dependence of conductivity of the form $\Delta\sigma \sim T^n$ (where n = 3/2, 2, or 4 and $\Delta\sigma$ is the variation of conductivity with temperature) are fulfilled for high-pressure phases [71]. However, a detailed classification and a comprehensive analysis of the conduction mechanisms for such phases are still lacking.

5.2. Optical Properties and Hopping Conduction of Carbynoid Materials

Absorption spectra of carbyne samples with the degree of oxidation varying from 8 to 22% are presented in Fig. 8. The spectra point to the semiconducting nature of the starting carbyne. Formally, spectra of this type can be assigned to a substance with an indirect bandgap (with a width of 1–1.5 eV), and the tail extended down to 0.8–1.0 eV correlates well with the amorphous nature of the substance under consideration.

Whereas the starting carbyne has a high resistivity (>10^8 Ω cm), the insulator–metal transition due to carbyne graphitization can be observed as a result of the thermobaric treatment in the conducting properties of the synthesized samples (Fig. 9). An analysis of temperature dependences of conductivity in this region is of special interest. The low-temperature portions of these curves can be described by Mott's law [46, 72, 73]

$$\rho = \rho_0 \exp[(T_0/T)^{\alpha}]. \quad (1)$$

Temperature dependences $\rho(T)$ for samples differing in T_{syn} are shown in Fig. 10 [72, 73]. Well-defined linear portions are observed for $T < T^* \sim 40$ K in the coordinates $\log(\rho) = f(T^{-\alpha})$, which can be traced down to $T \sim 1.8$ K. The index α increases with decreasing synthesis temperature (Fig. 10) [72, 73]. For T_{syn} = 1160 K, this parameter equals 1/4, which corresponds to Mott's law in the 3D case, and a decrease in T_{syn}

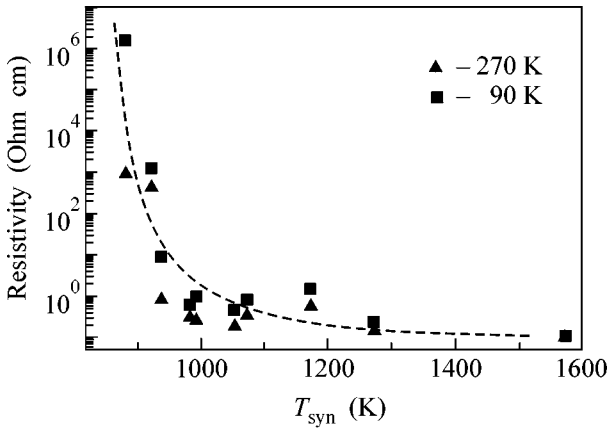

Fig. 9. Resistivity measured at two temperatures 90 and 270 K for carbyne samples after a thermobaric treatment at 7.7 GPa. Dashed lines are drawn by the eye guide.

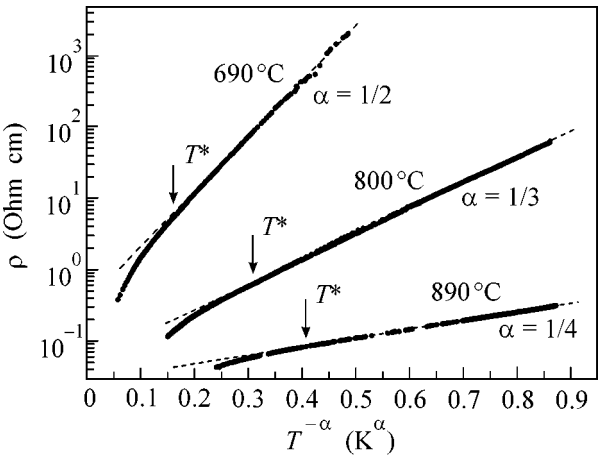

Fig. 10. Conductivities of carbyne samples obtained at different synthesis temperatures as functions of temperature.

down to 1070 K leads to an increase in α up to a value of 1/3, which is characteristic of 2D hopping conduction (Eq. (2)). In the vicinity of T_{syn} ~ 970 K, the hopping conduction exponent changes again to a value of 1/2 (Fig. 10, T_{syn} = 960 K).

A comprehensive study of static and dynamic conductivities, thermal emf, magnetoresistance, and Hall effect [72–74] demonstrated experimentally that a change in the synthesis temperature under pressure actually induces a crossover from 1D to 3D hopping conduction and that the hopping conduction of the phases obtained corresponds to 2D hopping conduction in the intermediate region of synthesis temperatures $970 < T_{syn} < 1170$ K. This interpretation agrees qualitatively with the data of structural and Raman measurements on the $sp \longrightarrow sp^2$ transition and carbyne graphitization, because the degree of cross-linking of carbon chains increases with T_{syn}, and the dimensionality of the system must increase. As a result, carbynes synthesized under pressure prove to be a unique model object that allows the variation of the effective dimensionality of hopping conductivity.

6. ELASTIC AND MECHANICAL PROPERTIES

Considering the mechanical and elastic properties of phases synthesized from C_{60} upon heating, one can conventionally distinguish between phases of relatively low ($P < 8$ GPa) and relatively high ($P > 8$ GPa) pressures. In fact, this subdivision corresponds to carbon phases with densities of ~1.8–2.4 g/cm^3 and ~2.5–3.5 g/cm^3, respectively. The second group of phases is of applied interest, because most of these phases are superhard materials.

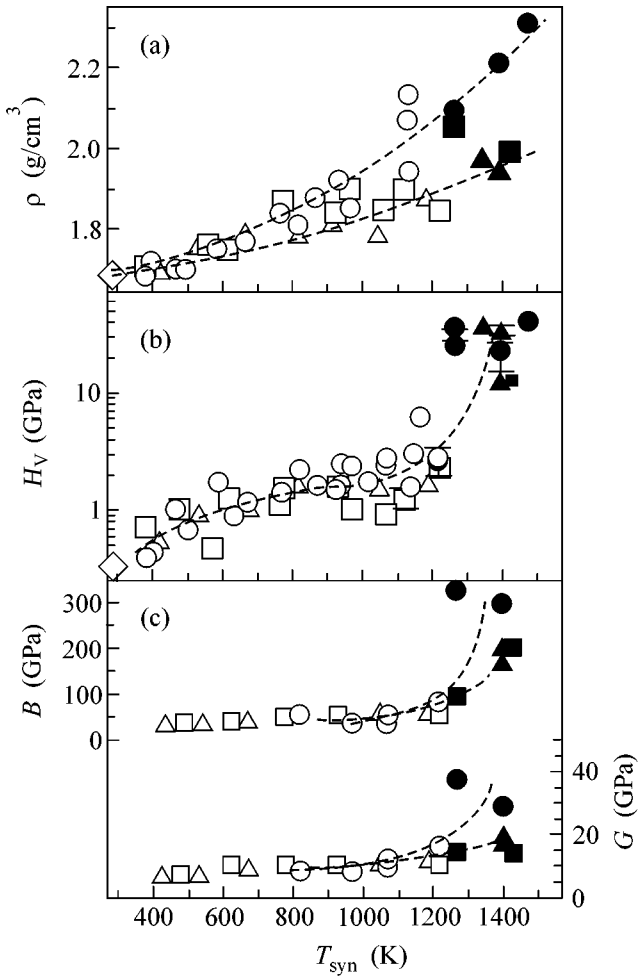

Fig. 11. Dependences of (a) density, (b) Vickers hardness, and (c) ultrasonic elastic moduli for samples synthesized from C_{60} under pressures of 3.5 GPa (triangles), 5 GPa (squares), and 8 GPa (circles). Light symbols correspond to 1D and 2D C_{60} polymerized phases, and black symbols correspond to disordered graphite-like phases. Dashed lines are drawn by the eye guide.

6.1. Low-Pressure C_{60}-based Phases

The density and the main mechanical properties of the phases synthesized in the pressure range 3.5–8 GPa are presented in Fig. 11. The elastic moduli were calculated in the approximation of a homogeneous medium [28]. As a result of the 1D–2D polymerization, the hardness of C_{60} increases approximately by 3 times, and the elastic moduli increase by 20–50%. The data presented are in a qualitative agreement with other measurements of polymerized phases [75–77]. The destruction of the molecular structure upon heating in the range of pressures under consideration leads to a drastic increase in hardness by more than an order of magnitude (Fig. 11), as was observed in [27]. In this case, the rearrangement of the molecular structure into an atomic nanocrystalline graphite-like phase (see Section 3) is far from being accompanied by a notable

increase in density (Fig. 11a). Note that the elastic moduli also increase significantly with the destruction of the molecular structure (Fig. 11). Such high values of the Vickers hardness at low densities for the disordered sp^2 phases should be related [18, 28] to their nanocrystalline structure and to the high degree of elastic recovery of the system of graphite-like clusters, which was also observed in deposited carbon films [78] or after C_{60} compression to pressures of ~20 GPa [79].

The appearance of an orientational anisotropy of the structure, that is, a texture (see, for example, Fig. 3 in Section 3.2), upon synthesis under nonhydrostatic conditions is an important feature of phases obtained from C_{60} under pressure. A substance with anisotropy along one preferred direction (the *z* axis in this case) will have a tensor of elastic constants that is equivalent to the tensor for a crystal with hexagonal symmetry, which is characterized by five independent constants, c_{11}, c_{12}, c_{33}, c_{13}, and c_{44}. The procedure of measuring and calculating elastic constants from ultrasonic data is described in detail in [56], where examples of such measurements and calculations are given for disordered graphite-like phases. The presence of an additional pressure component along *z* leads to a higher degree of polymerization along this axis (and, correspondingly, to a 20% higher longitudinal velocity along *z*) in the case of 2D polymers. However, the destruction of the molecular structure leads to the situation where the formed graphite-like clusters are predominantly perpendicular to the *z* axis with their graphene planes [56] (see Fig. 4), and the longitudinal velocities along *z* become 20–40% lower than the values measured in the direction perpendicular to *z*. We emphasize that such a detailed study of the possible anisotropy of elastic properties excludes errors in determining the real bulk modulus *B* of the substance, whereas the use of a uniaxial approximation may lead to physically incorrect values of *B* and Poisson coefficient [77, 80, 81].

6.2. High-Pressure C_{60}-based Phases

The hardness of carbon phases synthesized at high pressures >8 GPa increases with synthesis temperature [34, 37]. In accordance with our measurements, the majority of 3D C_{60} polymers, as well as the amorphous and nanocrystalline phases synthesized in the pressure range 9–13.5 GPa, can be assigned to superhard materials (H_V > 20 GPa). The crack resistance of superhard materials is their important mechanical characteristic, which can be determined from the length of cracks formed around the impression upon Vickers indentation [14]. The crack resistance factors are rather high (6–15 MN/m$^{3/2}$) for the majority of the phases under consideration. Note for comparison that the crack resistance factor of diamond is 7–10 MN/m$^{3/2}$. The range of synthesis temperatures from 600 to 700 K is of the most interest. The phases synthesized under these conditions [34] represent superhard 3D polymers that are actually ductile materials (cracks did not form upon their indentation).

The amorphous sp^2–sp^3 phases or nanocrystalline graphite–diamond composites synthesized from C_{60} are of special interest [34, 37]. The hardness of these materials approaches or, in particular cases, even exceeds the hardness of conventional diamond crystals; their crack resistance is approximately 1.5 times higher and their density (3.1–3.3 g/cm^3) is lower than the corresponding values for diamond [37]. Several reasons for such highest characteristics can be pointed out: (1) the optimal size of nanocrystallites (~5–10 nm) [82] corresponding to the maximum hardness values; (2) the uniform character of the formation of composites from rather soft molecular phases without nanopores, impurities, and distinct nanocrystallite boundaries; (3) the formation of a rigid "skeleton" of diamond-like clusters; and (4) the binding effect of graphite-like clusters, whose elastic recovery perpendicular to the graphene planes is anomalously high, whereas the strength of the planes against longitudinal stresses is very high.

6.3. Correlation between Mechanical Properties and Density

The study of correlations between the physical properties of various substances, in particular, between density and mechanical characteristics, is of great interest from both fundamental and applied points of view. The dependence of the Vickers hardness H_V on the density ρ is presented in Fig. 12 for a broad spectrum of carbon phases obtained from C_{60}, in comparison with the data for amorphous carbon sp^2–sp^3 films [5]. Despite the broad scatter of the obtained hardness values, the correlation between the density and hardness values is clearly seen. This correlation apparently has a universal character for various carbon phases. The general trend is an increase in hardness with increasing density, and the results for phases obtained from C_{60} are in a good agreement with the data on $H_V(\rho)$ for amorphous carbon films.

An exception is provided by the phases with densities typical of graphite (~1.8–2.2 g/cm^3), for which the hardness values can differ by more than an order of magnitude despite the occurrence of the $H_V(\rho)$ correlation (see [31] and Fig. 12). Graphite, the starting C_{60} fullerite, and also the polymerized 1D and 2D C_{60} phases are soft materials [31], whereas the disordered sp^2 phases with close densities may have hardness up to 40 GPa. It is evident that the phases whose covalent structure is characterized by macroscopic 2D ordering (or bonding) are soft.

Even better correlation is observed between the bulk elastic modulus *B* and the density of carbon phases whose covalent structure is characterized by 3D ordering. In Fig. 13, experimental data for the disordered sp^2–sp^3 phases synthesized from C_{60} [28, 56, 83] and

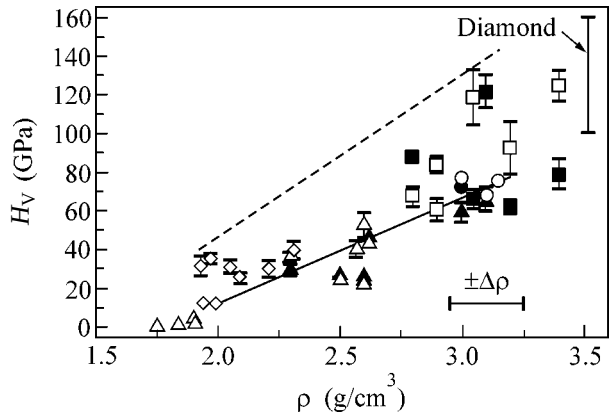

Fig. 12. Hardness vs. density for carbon phases obtained from C_{60}: triangles correspond to 3D polymers, rhombi correspond to graphite-like amorphous phases, circles correspond to diamond-like amorphous phases, and squares correspond to sp^2–sp^3 nanocomposites. Light symbols correspond to an indenter load of ≈2 N, symbols with a dot at the center correspond to ≈3.5 N, and black symbols correspond to ≈5 N. The data for diamond are taken for loads of 2–5 N (see references in [37]). Solid line corresponds to the dependence for amorphous films [5]. Dashed line is apparently the boundary of maximum possible hardness values for carbon phases obtained from C_{60}.

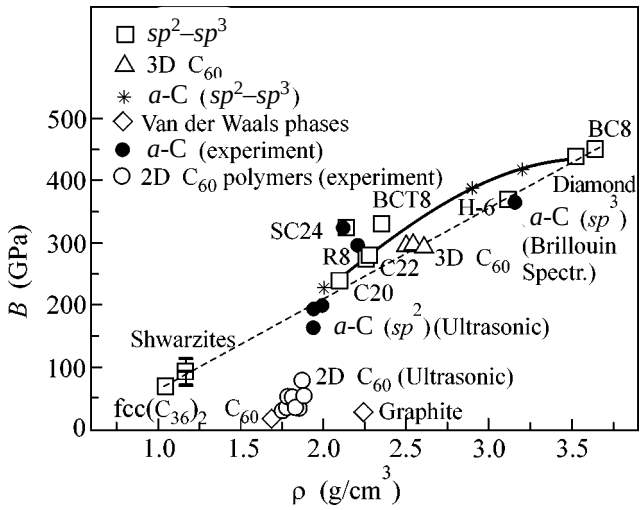

Fig. 13. Bulk compression modulus vs. density for allotropic carbon modifications and disordered phases (*a*-C) obtained from C_{60} [28, 56, 83] (experimental procedures are indicated in figure) and theoretical data for various hypothetical phases (by results of [84–90]).

for the real allotropic carbon modifications are compared with numerous calculations for hypothetical phases, including amorphous structures [84], 3D C_{60} polymers [51], sp^2 crystalline phases [85–89], and the high-pressure BC8 phase [90]. A good agreement between experimental and theoretical data is noteworthy. At the same time, the phases with 1D or 2D bonding of the covalent structure (graphite and 1D or 2D C_{60} polymers), as well as the starting fullerite (zero-dimensionally covalently bonded molecular van der Waals crystal) are considerably more compressible than the phases with three-dimensionally organized covalent structure.

7. CONCLUSION

The following main trends can be recognized in the structural transformations of C_{60} under high pressure: (1) C_{60} fullerite under high pressures and temperatures transforms to a more stable graphite or diamond through the intermediate polymolecular and disordered phases, (2) an increase in the temperature acting on C_{60} leads eventually to the irreversible destruction of the molecular structure, and (3) an increase in pressure on heating C_{60} leads to an increase in the density of the synthesized phases and in the mean coordination number of carbon atoms (in the interval from 3 to 4). In the case of carbyne, a similar transformation of the metastable phase to a more stable phase with a graphite-like structure proceeds. The common property of these processes consists in a sizeable change not only in the character of geometrical arrangement of atoms but also in the type of interatomic bonds.

An analysis of optical and electrotransport properties shows that the low-density carbon phases with a high structure-formation contribution of van der Waals forces, including the starting C_{60} and its 1D and 2D polymers, as well as quasi-one-dimensional atomic carbyne, are semiconductors with a bandgap of ~1 eV. An increase in the degree of polymerization (or moving C_{60} molecules closer together upon compression) results in a decrease in the semiconductor bandgap and an increase in its conductivity. The heating-induced nanocrystalline or amorphous graphite-like phases or the heterogeneous phases with a large fraction of the latter exhibit quasi-metallic conducting properties, whereas the diamond-like (sp^3) modifications obtained under higher pressures are already wide-bandgap semiconductors approaching diamond properties.

It is also shown that direct correlation between the hardness or bulk modulus and the density is observed for carbon phases. However, phases with low-dimensional (from zero-dimensional to 2D) macroscopic ordering of their covalent structure have lower mechanical and elastic characteristics.

We are grateful to E.V. Tat'yanin, A.V. Sapelkin, and V.A. Davydov for fruitful discussions and to A.G. Glazov for help in performing experiments.

This review is based on studies supported by the Russian Foundation for Basic Research, project nos. 99-02-17408, 00-02-16403, 01-02-17543, and 01-02-16557. This work was also supported by INTAS (project no. 00-807); the program "Fullerenes and Atomic Clusters" of the Ministry of Industry, Science, and Technology of the Russian Federation; NATO

research program; the program on the support of young scientists of the Ministry of Education of the Russian Federation (project no. PD02-1.2-336); and the program "Quantum Nanostructures" of the Russian Academy of Sciences.

REFERENCES

1. E. Yu. Tonkov, *Phase Transformations of Compounds at High Pressure: Handbook* (Metallurgiya, Moscow, 1988), Vol. 1, p. 142.
2. D. A. Young, *Phase Diagrams of Elements* (Univ. of California, Berkley, 1991).
3. J. Robertson, Adv. Phys. **35**, 317 (1986).
4. D. R. McKenzie, D. Muller, and B. A. Pailthorpe, Phys. Rev. Lett. **67**, 773 (1991).
5. M. Weiler, S. Sattel, T. Giessen, *et al.*, Phys. Rev. B **53**, 1594 (1996).
6. W. A. Harrison, *Electronic Structure and the Properties of Solids* (Freeman, San Francisco, 1980; Mir, Moscow, 1983).
7. W. Krätschmer, L. D. Lamb, K. Fostiropolous, and D. Huffman, Nature **347**, 354 (1990).
8. S. Iijima, Nature **354**, 56 (1991).
9. Yu. P. Kudryavtsev, S. E. Evsyukov, M. V. Guseva, *et al.*, Izv. Ross. Akad. Nauk, Ser. Khim. **42**, 450 (1993).
10. Yu. P. Kudryavtsev, R. B. Heimann, and S. E. Evsyukov, J. Mater. Sci. **31**, 557 (1996).
11. H. W. Kroto, J. R. Heath, S. C. O'Brien, *et al.*, Nature **318**, 162 (1985).
12. A. P. Dement'ev, private communication.
13. B. M. Bulychev and I. A. Udod, Ross. Khim. Zh. **39**, 9 (1995).
14. A. R. Evans and T. R. Wilshaw, Acta Metall. **24**, 939 (1976).
15. V. V. Brazhkin and A. G. Lyapin, Usp. Fiz. Nauk **166**, 893 (1996) [Phys. Usp. **39**, 837 (1996)].
16. B. Sundqvist, Adv. Phys. **48**, 1 (1999).
17. B. Sundqvist, Phys. Status Solidi B **223**, 469 (2001).
18. A. G. Lyapin, in *Perspectives of Fullerene Nanotechnology*, Ed. by E. Osawa (Kluwer, Dordrecht, 2002), p. 199.
19. V. A. Davydov, L. S. Kashevarova, A. V. Rakhmanina, *et al.*, J. Phys. Chem. B **103**, 1800 (1999).
20. M. N. Kondrin, A. G. Lyapin, V. V. Brazhkin, and S. V. Popova, Fiz. Tverd. Tela (St. Petersburg) **44**, 431 (2002) [Phys. Solid State **44**, 447 (2002)].
21. Y. Iwasa, T. Arima, R. M. Fleming, *et al.*, Science **264**, 1570 (1994).
22. M. Núñez-Regueiro, L. Marques, J.-L. Hodeau, *et al.*, Phys. Rev. Lett. **74**, 278 (1995).
23. L. Marques, J.-L. Hodeau, M. Núñez-Regueiro, and M. Perroux, Phys. Rev. B **54**, R12633 (1996).
24. V. A. Davydov, L. S. Kashevarova, A. V. Rakhmanina, *et al.*, Pis'ma Zh. Éksp. Teor. Fiz. **66**, 110 (1997) [JETP Lett. **66**, 120 (1997)].
25. V. A. Davydov, L. S. Kashevarova, A. V. Rakhmanina, *et al.*, Phys. Rev. B **58**, 14786 (1998).
26. V. A. Davydov, L. S. Kashevarova, A. V. Rakhmanina, *et al.*, Phys. Rev. **61**, 11936 (2000).
27. M. E. Kozlov, M. Hirabayashi, K. Nozaki, *et al.*, Appl. Phys. Lett. **66**, 1199 (1995).
28. A. G. Lyapin, V. V. Brazhkin, E. L. Gromnitskaya, *et al.*, Appl. Phys. Lett. **76**, 712 (2000).
29. V. V. Brazhkin, A. G. Lyapin, Yu. V. Antonov, *et al.*, Pis'ma Zh. Éksp. Teor. Fiz. **62**, 328 (1995) [JETP Lett. **62**, 350 (1995)].
30. V. D. Blank, S. G. Buga, N. R. Serebryanaya, *et al.*, Phys. Lett. A **205**, 208 (1995).
31. V. V. Brazhkin, A. G. Lyapin, and S. V. Popova, Pis'ma Zh. Éksp. Teor. Fiz. **64**, 755 (1996) [JETP Lett. **64**, 802 (1996)].
32. V. D. Blank, S. G. Buga, N. R. Serebryanaya, *et al.*, Phys. Lett. A **220**, 149 (1996).
33. V. V. Brazhkin, A. G. Lyapin, S. V. Popova, *et al.*, Phys. Rev. B **56**, 11465 (1997).
34. V. V. Brazhkin, A. G. Lyapin, S. V. Popova, *et al.*, J. Appl. Phys. **84**, 219 (1998).
35. H. Hirai, K. Kondo, N. Yoshizava, and M. Shiraishi, Appl. Phys. Lett. **64**, 1797 (1994).
36. H. Hirai, Y. Tabira, K. Kondo, *et al.*, Phys. Rev. B **52**, 6162 (1995).
37. V. V. Brazhkin, A. G. Lyapin, R. N. Voloshin, *et al.*, Pis'ma Zh. Éksp. Teor. Fiz. **69**, 822 (1999) [JETP Lett. **69**, 869 (1999)].
38. A. Dworkin, H. Szwarc, V. A. Davydov, *et al.*, Carbon **35**, 745 (1997).
39. P. A. Heiney, J. E. Fisher, A. R. McChie, *et al.*, Phys. Rev. Lett. **66**, 2911 (1991).
40. V. A. Davydov, L. S. Kashevarova, A. V. Rakhmanina, *et al.*, Chem. Phys. Lett. **333**, 224 (2001).
41. A. M. Rao, P. Zhou, K.-A. Wang, *et al.*, Science **259**, 955 (1993).
42. C. Goze, F. Rachdi, L. Hajji, *et al.*, Phys. Rev. B **54**, R3676 (1996).
43. F. Rachdi, C. Goze, L. Hajji, *et al.*, J. Phys. Chem. Solids **58**, 1645 (1997).
44. A. Rezzouk, F. Rachdi, Y. Errammach, *et al.*, Solid State Commun. **115**, 661 (2000).
45. T. Horikawa, K. Suito, M. Kobayashi, and A. Onodera, Phys. Lett. A **287**, 143 (2001).
46. A. G. Lyapin, V. V. Brazhkin, S. G. Lyapin, *et al.*, Phys. Status Solidi B **211**, 401 (1999).
47. V. D. Blank, B. A. Kulnitskiy, and Ye. V. Tatyanin, Phys. Lett. A **204**, 151 (1995).
48. L. Marques, M. Mezouar, J. L. Hodeau, *et al.*, Science **283**, 1720 (1999).
49. V. A. Davydov, L. S. Kashevarova, A. V. Rakhmanina, *et al.*, Pis'ma Zh. Éksp. Teor. Fiz. **63**, 778 (1996) [JETP Lett. **63**, 818 (1996)].
50. S. Okada, S. Saito, and A. Oshiyama, Phys. Rev. Lett. **83**, 1986 (1999).
51. E. Burgos, E. Halac, R. Weht, *et al.*, Phys. Rev. Lett. **85**, 2328 (2000).
52. N. R. Serebryanaya and L. A. Chernozatonskii, Solid State Commun. **114**, 537 (2000).
53. V. V. Brazhkin and A. G. Lyapin, Phys. Rev. Lett. **85**, 5671 (2000).
54. E. V. Tat'yanin, private communication.

55. V. D. Blank, Ye. V. Tatyanin, and B. A. Kulnitskiy, Phys. Lett. A **225**, 121 (1997).
56. A. G. Glazov, V. V. Mukhamad'yarov, V. V. Brazhkin, *et al.*, Pis'ma Zh. Éksp. Teor. Fiz. **73**, 621 (2001) [JETP Lett. **73**, 552 (2001)].
57. F. Moshary, N. H. Chen, I. F. Silvera, *et al.*, Phys. Rev. Lett. B **69**, 466 (1992).
58. J. L. Hodeau, J. M. Tonnerre, B. Bouchet-Fabre, *et al.*, Phys. Rev. B **50**, 10311 (1994).
59. M. Núñez-Regueiro, P. Monceau, A. Rassat, *et al.*, Nature **354**, 289 (1991).
60. B. Sundqvist, Phys. Rev. B **57**, 3164 (1998).
61. V. D. Blank, S. G. Buga, G. A. Dubitsky, *et al.*, Carbon **36**, 319 (1998).
62. T. L. Makarova, Fiz. Tekh. Poluprovodn. (St. Petersburg) **35**, 257 (2001) [Semiconductors **35**, 243 (2001)].
63. Yu. A. Osip'yan, V. E. Fortov, K. L. Kagan, *et al.*, Pis'ma Zh. Éksp. Teor. Fiz. **75**, 680 (2002) [JETP Lett. **75**, 563 (2002)].
64. K. P. Meletov, G. Kourouklis, D. Christofilos, and S. Ves, Zh. Éksp. Teor. Fiz. **108**, 1456 (1995) [JETP **81**, 798 (1995)].
65. T. L. Makarova, N. I. Nemchuk, A. Ya. Vul', *et al.*, Pis'ma Zh. Tekh. Fiz. **22** (24), 75 (1996) [Tech. Phys. Lett. **22**, 985 (1996)].
66. T. L. Makarova, T. Wagberg, B. Sundqvist, *et al.*, Mol. Mater. **13**, 151 (2000).
67. P. Scharff, B. Sundqvist, M. E. Gaevski, *et al.*, Carbon **39**, 2203 (2001).
68. T. L. Makarova, B. Sundqvist, P. Scharff, *et al.*, Synth. Met. **121**, 1099 (2001).
69. A. V. Okotrub, V. V. Belavin, L. G. Bulusheva, *et al.*, J. Chem. Phys. **115**, 5637 (2001).
70. H. Hirai, M. Terauchi, M. Tanaka, and K. Kondo, Phys. Rev. B **60**, 6357 (1999).
71. S. G. Buga, V. D. Blank, G. A. Dubitsky, *et al.*, J. Phys. Chem. Solids **61**, 1009 (2000).
72. S. V. Demishev, A. A. Pronin, N. E. Sluchanko, *et al.*, Pis'ma Zh. Éksp. Teor. Fiz. **72**, 547 (2000) [JETP Lett. **72**, 381 (2000)].
73. S. V. Demishev, A. A. Pronin, N. E. Sluchanko, *et al.*, Fiz. Tverd. Tela (St. Petersburg) **44**, 585 (2002) [Phys. Solid State **44**, 607 (2002)].
74. S. V. Demishev, A. A. Pronin, V. V. Glushakov, *et al.*, Zh. Éksp. Teor. Fiz. **122**, 140 (2002) [JETP **95**, 123 (2002)].
75. A. Matsumuro, Y. Takada, Y. Takahashi, *et al.*, Rev. High Pressure Sci. Technol. **7**, 823 (1998).
76. S. Berezina, V. Blank, V. Levin, and V. Prokhorov, Ultrasonics **38**, 327 (2000).
77. V. M. Levin, V. D. Blank, V. M. Prokhorov, *et al.*, J. Phys. Chem. Solids **61**, 1017 (2000).
78. I. Alexandrou, H.-J. Scheibe, C. J. Kiely, *et al.*, Phys. Rev. B **60**, 10903 (1999).
79. A. V. Talyzin, L. S. Dubrovinsky, M. Oden, and U. Janson, Diamond Relat. Mater. **10**, 2044 (2001).
80. V. D. Blank, V. M. Levin, V. M. Prokhorov, *et al.*, Zh. Éksp. Teor. Fiz. **114**, 1365 (1998) [JETP **87**, 741 (1998)].
81. V. M. Prokhorov, V. D. Blank, S. G. Buga, and V. M. Levin, Synth. Met. **103**, 2439 (1999).
82. S. Yip, Nature **391**, 532 (1998).
83. M. H. Manghnani, S. Tkachev, P. V. Zinin, *et al.*, Phys. Rev. B **64**, 121403(R) (2001).
84. P. C. Kelires, Phys. Rev. Lett. **73**, 2460 (1994).
85. A. Y. Liu, M. L. Cohen, K. C. Hass, and M. A. Tamor, Phys. Rev. B **43**, 6742 (1991).
86. G. Jungnickel, P. K. Sitch, Th. Frauenheim, *et al.*, Phys. Rev. B **57**, 661 (1998).
87. M. Côté, J. C. Grossman, M. L. Cohen, and S. G. Louie, Phys. Rev. B **58**, 664 (1998).
88. S. J. Townsend, T. J. Lenosky, D. A. Muller, *et al.*, Phys. Rev. Lett. **69**, 921 (1992).
89. V. Rosato, M. Celino, G. Benedek, and S. Gaito, Phys. Rev. B **60**, 16928 (1999).
90. C. Mailhiot and A. K. McMahan, Phys. Rev. B **44**, 11578 (1991).

Translated by A. Bagatur'yants